MAX-PLANCK INSTITUTE FOR POLYMER RESEARCH

JOHANNES GUTENBERG UNIVERSITY MAINZ

DISSERTATION

Polarization Dynamics in Ferroelectric Thin Films

Written by
Dong Zhao

Supervised by
Prof. Dr. Paul Blom (Max-Planck Institute for Polymer Research)
Prof. Dr. Hans-Joachim Elmers (Institute of Physics, Johannes Guttenberg University Mainz)

Jul. 11, 2017

Declaration of Authorship

I declare that I have written the enclosed PhD thesis by myself, and have not used sources or means without declaration in the text. Any thoughts from others or literal quotations are clearly marked.

Signed: _____

Date: _____

Contents

1. Introduction

1.1. Fundamentals of ferroelectricity ……2

1.2. PVDF-based polymer ferroelectric thin films ……..……..4

1.3. Motivation of the thesis ..…...……..7

1.4. Outline of the thesis .....……...11

2. Theory of polarization switching

2.1. Intrinsic and extrinsic switching ……14

2.2. Landau-Ginzburg-Devonshire theory ..……15

2.3. Monte-Carlo simulation ....……..18

2.4. Effects of disordered pinning sites ...……19

2.5. Summary ...……23

3. Device fabrication and characterization

3.1. Spin-coated P(VDF-TrFE) thin films .....……25

3.2. Electrical measurements .....……25

3.3. Piezoresponse force microscopy (PFM) ……..……30

4. Switching dynamics in disordered ferroelectric thin films

4.1. Kolmogorov-Avrami-Ishibashi (KAI) model ……...……33

4.2. Characteristic parameters extracted from switching transients ……35

4.3. Random-walk model for disordered ferroelectric thin films ……39

4.4. Summary ..……...……43

5. Piezoresponse force microscopy study of ferroelectric domains

5.1. Global excitation and local probing method ..……..……..46

5.2. PFM phase analysis and macroscopic ferroelectric polarization ..……47

5.3. Domain morphology during polarization switching ……..……51

5.4. Summary ....……53

6. Depolarization field and domain-wall depinning mechanism

6.1. Depolarization field ……55

6.2. Suppression of the remanent polarization ...56

6.3. Dynamics of depolarization ...59

6.4. Depolarization diagram ...61

6.5. Origin of activation field ...65

6.6. Temperature dependence ...66

6.7. Summary ...67

7. Polarization fatigue of P(VDF-TrFE) ferroelectric capacitors

7.1. Fatigue of ferroelectric capacitors ...70

7.2. Fatigue of P(VDF-TrFE) capacitors with Au electrodes ...71

7.3. Mechanism ...74

7.4. Fatigue-free P(VDF-TrFE)-based capacitors ...79

7.5. Summary ...80

8. Perspective: in-plane polarization and vortices in ferroelectrics

8.1. Charged domain walls ...83

8.2. In-plane vortices and skyrmionic configurations ...83

Summary 86

Acknowledgement 87

List of publications 89

References 90

Chapter 1 Introduction

A ferroelectric material exhibits a spontaneous polarization at zero electric field. The material holds two or more discrete, stable or metastable, polarization states between which it can switch upon an applied electric field. In this Chapter, the principles of ferroelectricity are reviewed. The microscopic origin of ferroelectricity is discussed from both an ab initio and a phenomenological point of view. The ferroelectricity in polymers is specifically reviewed from monomeric to the macroscopic device level. After introducing the basic background, the motivation and outline of this thesis are presented.

1.1 Fundamentals of ferroelectricity

Ferroelectric materials refer to a group of materials with spontaneous polarization that can be switched by an applied electric field higher than the coercive field [1]. The term *ferroelectricity* is used in analogy to ferromagnetism, which had already been known when ferroelectricity was discovered in 1920 in Rochelle salt by Valasek [2] [3]. Thus, the prefix *ferro*, meaning iron, was used to describe the property despite the fact that most ferroelectric materials do not contain iron.

Ferroelectric materials are featured by the hysteretic relation between the electric displacement, *D*, (or polarization, *P*) and the applied electric field, *E*. By applying an alternating electric field with an amplitude higher than the coercive field, a *D-E* hysteresis loop can be recorded. The *D-E* loops of $Pb(Zr,Ti)O_3$ (PZT) and of the random copolymer of vinylidene fluoride with trifluoroethylene [P(VDF-TrFE)] capacitors are presented in Fig. 1.1.1 respectively as examples.

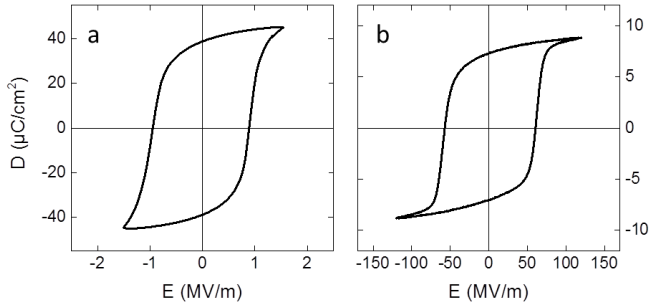

FIG. 1.1.1 *D-E* hysteresis loops of (a) $Pb(Zr,Ti)O_3$ (PZT) ceramic- and (b) the random copolymer of vinylidene fluoride with trifluoroethylene [P(VDF-TrFE)] thin-film capacitors.

Origin of ferroelectricity

Microscopically, ferroelectric materials consist of polar unit cells. The polarity of the unit cells is due to atomic or molecular displacement for ionic or molecular crystals (semi-crystalline) respectively, as schematically illustrated in Fig. 1.1.2.

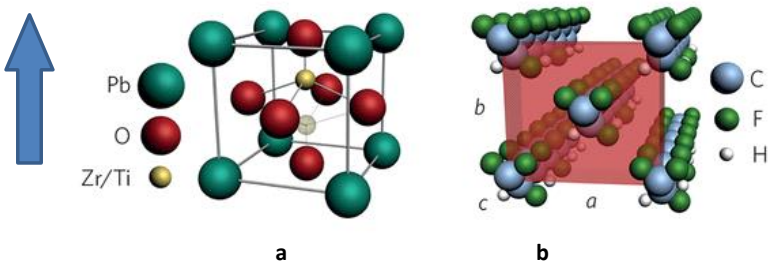

Fig. 1.1.2 Schematics of the unit cell of lead zirconate titanate (PZT) (a) and β-PVDF (b). The blue arrow denotes the polarity of the unit cell. Figure adapted from Ref [4].

In 1992, Cohen has conducted electronic-structure calculations on the ferroelectric perovskites $BaTiO_3$ and $PbTiO_3$ [5]. He investigated the ferroelectric stability based on atomic displacement in the unit cell, the so-called "ferroelectric distortion", in the ground state. The ground-state energy was obtained for various atomic displacements of Ti; a double-well energetics indicates that a spontaneous polar unit cell, corresponding to the ferroelectric phase, is energetically favoured. His calculations suggested that the hybridization between the titanium 3*d* states and the oxygen 2*p* states is essential for ferroelectricity; when this hybridization is inhibited the nonpolar cubic phase becomes the most stable one, yielding no ferroelectricity. Furthermore he showed that the long-range Coulomb energy favours ferroelectricity whereas the short-range covalent interactions favour the nonpolar cubic phase. He concluded for general ferroelectric perovskites, ABO_3, that hybridization between the B cation and the oxygen anion is essential to weaken the short-range repulsions and to allow the ferroelectric transition. This delicate balance of the short-range forces favouring the cubic phase and the long-range forces favouring the ferroelectric phase makes the ferroelectric-paraelectric phase transition sensitive to defects and chemical composition.

At the same period of time, the modern definition of polarization, known as the Berry-phase theory of polarization [6] [7] [8], was established. The polarization results from the distribution of the electron wavefunction in a periodic lattice and is defined as:

$$P = \frac{e}{(2\pi)^3} \mathrm{Im} \sum_n \int d\mathbf{k} < u_{n\mathbf{k}} \mid \nabla_{\mathbf{k}} \mid u_{n\mathbf{k}} > + \frac{e}{\Omega} \sum_s Z_s^{ion} \mathbf{r}_s \qquad (1.1.1)$$

where the first term at the right side is the contribution from electrons and the second term is the contribution arising from the positive point charges eZ_s^{ion} located at atomic positions $\mathbf{r}_s$. $u_{n\mathbf{k}}$ is the Bloch function for the *n*-th level in **k**-space, satisfying $u_{n\mathbf{k}+\mathbf{G}} = \exp(-i\mathbf{G}\cdot\mathbf{r})u_{n\mathbf{k}}$ where **G** is a translational reciprocal lattice vector. The spontaneous polarization, *i.e.* non-zero *P* at zero electric field, is unambiguously determined by the electronic structure and ion displacement in the unit cell when the system is in the ground state.

Order-disorder transition

As discussed above, the phase transition between the polar and nonpolar crystal structures, *e.g.* $PbTiO_3$ from tetragonal to cubic at 766 K [5], is structural type, often termed "displacive" phase transition. The appearance and disappearance of ferroelectricity, however, can also be an order-disorder type phase transition where the polarity of a single unit cell is maintained whereas the vanishing of ferroelectricity results from the disordered alignment of each polar unit cells [9]. The antiferroelectric phase [10] is an example.

Monte Carlo simulations based on a first-principles Hamiltonian have suggested that the cubic-tetragonal transition in $BaTiO_3$, which used to be thought of as displacive, may be better described as of the order-disorder type [11]. Quadrupole perturbed Ti NMR measurements [12] have shown that Ti atoms are disordered between several off-centre sites in the paraelectric phase near the Curie temperature, T_c, and order into well-defined positions below T_c, which confirms the presence of the order-disorder type in the ferroelectric-paraelectric phase transition of $BaTiO_3$.

In the ferroelectric polymers PVDF and P(VDF-TrFE), X-ray diffraction measurements have confirmed that the ferroelectric-paraelectric phase transition at T_c is structural, similar to the displacive transition in ionic ferroelectrics, as nicely reviewed by Tashiro and Kobayashi [13]. During the transition, the unit cell changes from the polar β form, consisting of two all-*trans* chains, into the α form, consisting of two tg^+tg^- chains with antiparallel moments, leading to a zero net polarity. It is recently suggested however, that at the β relaxation temperature, $T_\beta \approx 250$ K for P(VDF-TrFE) (70/30 mol. %), the PVDF unit cell undergoes an order-disorder transition from a disordered 3/1 helical conformation above T_β to an all-*trans* order below T_β [14].

In summary, the emergence of ferroelectricity requires both a polar structure of the unit cells and the ordered alignment of the unit cells. The ferroelectric-paraelectric transition in different materials, or in a same material but at different experimental conditions, can originate from either or hybrid mechanisms.

Classic description of ferroelectrics

Despite the intensive studies on the electronic structures at the microscopic level, the classic Clausius model [15] still provides the most widely used scenario of the macroscopic polarization. The macroscopic polarization, *P*, is regarded as the sum of individual dipoles, p_i, within the volume *V*, which reads:

$$P = \frac{\sum_i p_i}{V} \tag{1.1.2}$$

In the ferroelectric phase, the dipole moments, p_i, are non-zero, and the dipoles are energetically favoured to align parallel at zero electric field, resulting in the spontaneous macroscopic polarization. The ferroelectric material as a thermodynamic system is characterized by the Helmholtz free energy, *F*, or Gibbs free energy, *G*, depending on the state parameters taken. The free energy expanded with the macroscopic polarization, *P*, known as the Landau-Devonshire theory [16] [17], is widely used for studying the ferroelectric-paraelectric phase transition and the polarization dynamics for instance at applied electric field and mechanical stress. Polarization switching described within the Landau phase transition framework shall be elaborated in **Chapter 2**.

1.2 PVDF-based polymer ferroelectric thin films

Since the 1970s, PVDF and P(VDF-TrFE) have been increasingly gaining interests from the ferroelectric community [18] [19]. Compared with their inorganic counterparts, these ferroelectric polymers possess special advantages such as easy processability, flexibility and low cost [20]. PVDF-based ferroelectric materials are compatible with low temperature flexible substrates enabling up-scaling by large-area solution processing. PVDF-based ferroelectric capacitors maintain a remanent polarization and coercive field constant upon bending with a radius of curvature down to 1 cm, which makes them ideal candidates for flexible electronics or system-in-foil applications [21]

[22]. As an example, high performance non-volatile polymer memories on banknotes have recently been realized [23].

The polar units at different length scale in a PVDF thin film are schematically presented in Fig. 1.2.1. Below we shall discuss the structural features and the resulting polarity from the molecular level to the macroscopic scale.

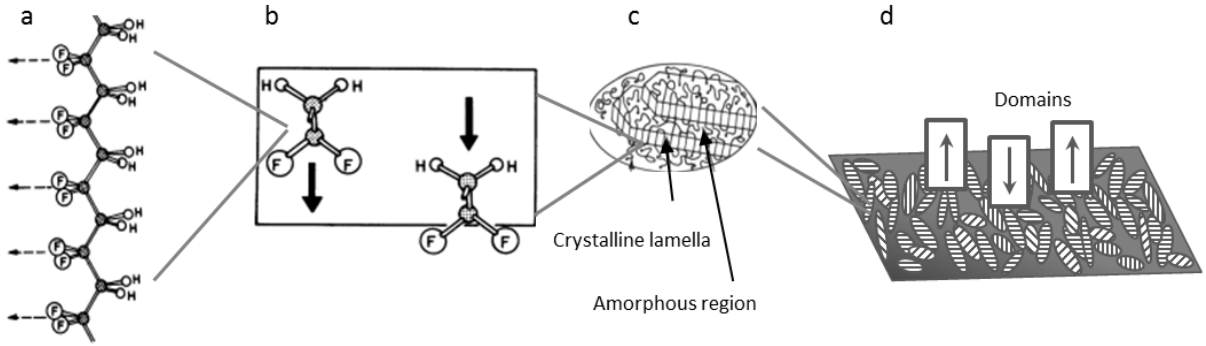

FIG. 1.2.1 Schematics of the relation between polarization and structural features of β-PVDF from the molecular to the macroscopic device level. Figure adapted from Ref. [20]. (a) An all-*trans* chain consisting of -[CH_2-CF_2]- monomers. (b) A primitive unit cell of a β-PVDF crystal. (c) The crystalline lamella and amorphous regions. (d) The grains and domains in a PVDF thin film.

Monomeric

The polymer chains consist of many elementary repeating units, termed as monomers. In PVDF, fluorine atom forms highly polar bonds with carbon, as -CF_2-, yielding a dipole moment of 2 debye [20]. These highly polar monomers are the elementary dipolar units in our investigated system.

Monomeric sequence and chain conformation

At this level we are talking about the intra-chain structure. In an ideal PVDF chain, the monomeric units -CH_2- (head) and -CF_2- (tail) sequence alternates during polymerization forming the periodic head-to-tail configuration. However, this sequence can be broken by "inappropriately" inserted segments forming head-to-head and tail-to-tail defects [24]. These intra-chain defects cause the average dipole moment of the chain per monomeric unit to be reduced [20], and are an origin of nucleation sites in the process of both crystallization and polarization switching, *c.f.* **Chapters 2,4** and **6**.

In the melt or solution, polymer chains coil randomly. In the solid state, chains tend to crystallize into regular conformations. The most favorable torsional bond arrangements have substituents at 180° to each other, termed as *trans*, or at ± 60°, termed as *gauche*$^{\pm}$; but actual torsion angles commonly deviate somewhat from these values. The all-*trans* conformation yields the highest polarity, which is perpendicular to the chain. A schematic of an all-*trans* chain is shown in Fig. 1.2.1 (a).

Chain packing

The ability of molecules to adopt polar conformations is not sufficient to ensure polarity of their resulting crystals, as these molecules may be crystallographically packed in a lattice so as to cancel each other's moment. An example is α-PVDF, whose unit cell contains two tg^+tg^- chains with antiparallel dipole moments leading to zero net polarity. This is the ground state for PVDF homopolymer [25]. The most polar phase of PVDF is the β phase, whose unit cell consisting of two all-*trans* chains are packed parallel, as schematically shown in Fig. 1.2.1 (b). In this type of packing, the fluorine and hydrogen atoms of neighbouring chains are approximately at the same level, which is energetically favoured and plays a major role in stabilizing the crystalline structure of β-PVDF. The presence of TrFE in the copolymer P(VDF-TrFE) increases the crystallinity, and makes the β phase the most favoured phase [20].

Typically, after solution processing, *e.g.* spin-coating, and thermal annealing, a thin film of P(VDF-TrFE) solidified on the substrate phase-separates into grains of polycrystalline and amorphous regions. The crystallinity is about 50 % [26]. Within the crystals, the chains are packed, forming the lamellae of β-phase PVDF, as schematically shown in Fig. 1.2.2 (a). Within the amorphous regions, the chains are randomly coiled, with no contribution to the polarity, as schematically shown in Fig. 1.2.1 (c,d). The topography of an annealed P(VDF-TrFE) thin film measured by scanning electron microscopy (SEM) is shown in Fig. 1.2.2 (b). The rice-like grains form the lamellae of the β-phase PVDF.

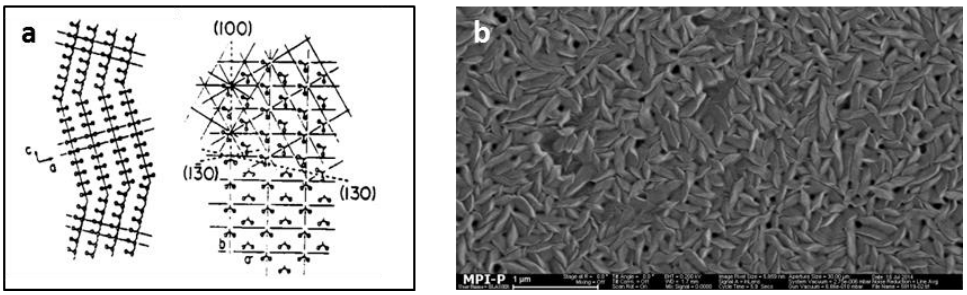

FIG. 1.2.2 (a) Lamellae of β-PVDF after thermal annealing, adapted from Ref. [13]. (b) Scanning electron microscope (SEM) micrograph of a 500 nm-thick P(VDF-TrFE) film spin-coated on a quartz substrate. Prior to SEM measurement, the film has been annealed at 140 °C for 2 hours.

Domains

Now we are at the macroscopic level. In a partially polarized ferroelectric material, one can expect two scenarios: (i) the whole material is identically polarized to a value between the plus and minus saturated polarization values, or (ii) the polarization is spatial inhomogeneous. In P(VDF-TrFE) thin films, the situation (ii) is practically observed. A region sharing a same local polarization is referred to as a domain [9]. Domains are widely present in ferroelectric materials, including Langmuir-Blodgett PVDF ultrathin films, epitaxial oxide thin films, spin-coated P(VDF-TrFE) thin films and bulk ceramics.

The morphology of the out-of-plane domains measured on a P(VDF-TrFE) film on a Au bottom electrode by piezoresponse force microscopy (PFM) is presented in Fig. 1.2.3 (b). The topography of

the same region is presented in Fig. 1.2.3 (a) as comparison.

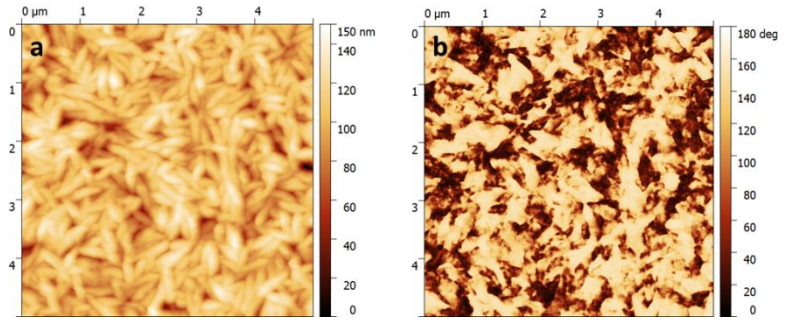

FIG. 1.2.3 Piezoresponse force microscope images. (a) Topography of a 500 nm-thick P(VDF-TrFE) film spin-coated on Au bottom electrode. (b) Out-of-plane piezoresponse phase image scanned in the same region as (a).

It can be seen from Fig. 1.2.3 that the domains are not limited by the grain boundaries in the spin-coated P(VDF-TrFE) thin film. In **Chapter 5**, we shall specifically study the domain morphology with the PFM. When the polarization of different domains is added up over the whole material, the macroscopic polarization is obtained; the experimental verification of this relation is also presented in **Chapter 5**.

1.3 Motivation of the thesis

The remanent polarization at zero electric field and the capability of being switched between multiple stable states make ferroelectric materials good candidates for non-volatile memories. Practically, ferroelectric materials are commercially available and have been applied to ferroelectric random-access memories (FeRAM) for computers and radio frequency identification (RFID) cards [27].

For application in data storage, three factors are crucial: (i) a fast writing/reading speed, (ii) a reliable data retention, and (iii) a slow degradation during a large number of writing/reading cycles. These challenges have attracted a wide research interest from both industry and academia, since they are not only of practical interests but trigger intriguing fundamental questions related to the ferroelectric materials as well.

It is the major scope of this thesis to study the polarization-related device physics motivated by the aforementioned practical requirements. We focus on thin films of the ferroelectric polymer poly-vinylidene-fluoride (PVDF) and its random copolymers with trifluoroethylene [P(VDF-TrFE)]. We shall show that the conclusions derived also apply to inorganic ferroelectric materials such as $Pb(Zr,Ti)O_3$, and $BaTiO_3$.

Polarization switching

The polarization switching refers to the reversal of macroscopic polarization upon applied electric field. The understanding of the mechanism of polarization switching is crucial to improve the write/reading speed in ferroelectric-based memories.

The theory of polarization switching was first developed by Devonshire [17] based on the framework of Landau mean-field phase transition [16], and later was incorporated with the consideration of spatial inhomogeneity by Ginzburg [28], now termed as the Landau-Ginzburg-Devonshire theory [1]. The essential of the LGD theory is that the polarization switching is a predetermined result of lowering the free energy of the system. The LGD theory elegantly characterized the coercivity and the hysteresis of ferroelectric materials during their polarization switching. The LGD deals with ideal perfect ferroelectric single crystals in which the polarization switching is termed as the *intrinsic switching*. Practical materials contain dipolar defects such as local misaligned polar cells, for which an unsolvable contradiction between theoretical and experimental values of the coercive field occurs. For example, the coercive field of P(VDF-TrFE) predicted by the LGD theory is in the order of magnitude of GV/m whereas that obtained experimentally is typically 50 MV/m.

It has been well known nowadays that the polarization switching in practical ferroelectric devices is mediated by nucleation and growth of multidomains, termed as the *extrinsic switching* [29]. During this process, sporadic dipolar defects with polarity parallel to the applied field modify the energetic landscape, lowering the barrier for local dipolar reversal thus acting as nucleation centres for the growing switched regions (ferroelectric domains). In **Chapter 2** we show with Monte-Carlo simulations that the presence of such defects significantly lowers the coercive field; within the framework of the LGD theory, introducing a reasonable percentage of such defects yields the values and their frequency dependence of the coercive field comparable to device-level results measured from ferroelectric capacitors.

For applications, often it is the macroscopic polarization at the device level that matters. To this end, a statistical model for describing the growing ferroelectric domains is sufficient and elegant. The canonical statistical model for the extrinsic switching has been developed by Kolmogorov [30], Avrami [31] and Ishibashi [32] by the 1970s, now well known as the KAI model [29]. The beauty of the KAI model is that starting from simple and clear physical scenario it derives an explicit description of the reversed polarization as a function of elapsed time, and can quantitatively fit switching transients measured on a wide range of ferroelectric materials. Despite the simple physical scenario and the usually successful fit to measured switching transients, the quantitative explanation of the model parameters, *i.e.* the switching time and the Avrami index, is still a non-trivial issue. It is especially elusive that the Avrami indices, which should equal to the dimensionality of the ferroelectric system according to conventional KAI model, are often found non-integers. Furthermore, several non-KAI models have been increasingly proposed, especially for disordered and nanoscale ferroelectric systems [33] [34] [35] [36]. Such a debate has triggered our study on the switching dynamics in disordered polymer ferroelectric thin films. Our discussion on the switching dynamics is elaborated in **Chapter 4**.

Viewed from another aspect, the growth of ferroelectric domains is often taken as the motion of the domain walls which separate different domains [37]. Such a motion of the domain walls among defects is categorized into the creep type [38] which has a generic form in diverse elastic systems. The

depinning force in the creep formula is a key parameter. A possible origin of the depinning force in disordered ferroelectric systems is unexpectedly implied from our measurements. We discuss this part in **Chapter 6**.

Local probing of ferroelectric domain walls

To gain in-depth understanding of the polarization-related device physics of ferroelectric materials, a direct visualization of ferroelectric domains is of great help. The piezoresponse force microscopy (PFM), which is based on monitoring piezoelectric surface deformation induced by the electrically biased probing tip, has proven to be one of the most powerful tools in visualization and manipulation of ferroelectric domains. The PFM technique was first developed in 1992 by Guethner and Dransfeld [39] to detect polarized regions in thin films of the ferroelectric random copolymer poly(vinylidenefluoride-trifluoroethylene) [P(VDF-TrFE)]. Since then the PFM technique has been adapted for experiments such as sub-micron study of static domain morphology [40] [41], polarization switching [42] [43], domain-wall motion [38], non-linear dynamics of domains [44] and domain manipulation [38] [45] in a wide variety of ferroelectric materials.

In the PFM measurements, a ferroelectric sample is poled and measured by a PFM tip which contacts the top surface of the sample and can be electrically biased. In terms of poling, or in other words, exciting, the sample, there are two main methods in PFM [46]: local or global excitation. In the local excitation method, there is no top electrode; the ferroelectric material is poled by the biased PFM tip, which scans the bare top surface of the sample. In the global excitation method, the ferroelectric material is poled in a capacitor using the top electrode, through which the domains are imaged by PFM.

The local excitation method allows *in situ* investigation of fine structures of domains [40] [41] and field-induced domain-wall motion [38] with high resolution. The drawback, however, is that the electric field generated by the PFM tip is inhomogeneous, which hampers quantitative analysis of the field-induced signal [46]. Moreover, the spot under the PFM tip acts as an artificial nucleation site. Due to the high local electric field, the tip actively drives the nucleation and domain growth process [45], which significantly differs from the scenario of stochastic nucleation and multi-domain growth during macroscopic polarization switching in a homogeneous electric field [29].

On the other hand, in the global excitation method, due to the presence of the top electrode, the sample is exposed to a homogeneous electric field. By using this method, the growth of domains could successfully be correlated to polarization switching transients [42] [43], verifying the statistical theory of multi-domain growth proposed by Kolmogorov, Avrami and Ishibashi [30] [31] [32]. Remarkably, the global excitation method allows one to quantitatively bridge the microscopic domains with the electrically measured macroscopic polarization. However, the major drawback of the global excitation method is that the resolution is limited due to the presence of the top electrode [47] [48].

We note that an alternative PFM method is to investigate in-plane capacitors, where both electrodes are in a common plane with the ferroelectric material on the substrate [49] [50]. The ferroelectric material is poled via the in-plane electrodes and probed by the PFM tip above the sample. This method generates a homogeneous electric field inside the ferroelectric material without sacrificing the

intensity and resolution of the piezoresponse signal. However, unlike the top-view images by conventional PFM measurements, with planar capacitors one visualizes the lateral growth of the domains from side view. In that way, the lateral growth of domains is restricted to one dimension, along the parallel electrodes; this geometry may lead to different polarization switching mechanism from that in commonly used ferroelectric devices with a vertical structure.

Our goal is to simultaneously achieve high resolution and a homogeneous poling electric field distribution, and meanwhile keep the vertical structure of the ferroelectric device such that the lateral growth is not restricted. To this end, we have developed a measurement technique, called *global excitation and local probing method*. In **Chapter 5**, this technique will be elaborated.

Polarization fatigue

The fatigue, *i.e.* the reduction of the remanent polarization upon poling cycles, is vital to the application of ferroelectric devices.

The fatigue of inorganic ferroelectric thin films has been intensively investigated, as reviewed by Refs. [51] [52]. It has been reported that the fatigue of PZT capacitors could be due to local phase decomposition [53] [21]: under electrical bipolar stress the ferroelectric PZT perovskite phase is transformed into the paraelectric pyrochlore phase, which has been confirmed by Micro Raman measurements. Upon annealing the fatigued capacitor in oxygen ambient, the original ferroelectric perovskite PZT phase was completely restored. Therefore, it was concluded that fatigue is a generic problem of inorganic ferroelectric materials. The origin was argued to be the formation of oxygen vacancies causing a local, uncompensated high depolarization field.

Contrary to inorganic ferroelectrics, reports on fatigue of organic ferroelectrics are limited. The most studied organic ferroelectric materials are PVDF and its random copolymer with trifluoroethylene, P(VDF-TrFE). Fatigue in organic ferroelectric capacitors is a major problem as the spontaneous polarization is typically halved already after less than 10^6 cycles [52]. Fatigue depends on experimental parameters such as temperature, the type of electrodes and the frequency and amplitude of the applied waveform [54] [55] [56]. It has been reported for P(VDF-TrFE) that fatigue increases with increasing driving voltage and decreasing frequency. Bipolar driving leads to polarization fatigue, while unipolar switching does not. Application of polymer electrodes, such as poly(3,4-ethylenedioxythiophene) stabilized with polystyrene sulfonic acid (PEDOT:PSS), has been shown of improving the programming cycle endurance [23]. Evidences imply that fatigue also depend on the degree of crystallinity [57].

Fatigue in organic ferroelectric materials has been ascribed to charge trapping: injected charges get trapped at crystalline boundaries and defects, thereby pinning the domain walls and reducing the polarization [55]. Increasing the crystallinity concomitantly reduces the number of defects and grain boundaries, resulting in increased reliability. The use of poorly conducting polymer electrodes, or the introduction of an interfacial blocking layer, diminishes charge injection and, hence, fatigue [58]. However, apart from the intrinsic mechanisms, *e.g.* charge trapping, fatigue can have an extrinsic origin, such as delamination of the top electrode. A few reports [22] [59] mention this delamination and suggest a temperature rise due to the heat dissipation upon continuous cycling as the origin [22].

Strangely, the reported endurance of the P(VDF-TrFE) capacitors, which suffer the delamination of the top electrodes, is similar to that of the samples whose fatigue mechanism was argued to be intrinsic in other literatures. This implies that the endurance of commonly used PVDF-based polymer ferroelectric materials should be hampered by extrinsic reasons rather than by the intrinsic endurance of the ferroelectric polymers themselves. To clarify the real bottle-neck of the endurance of PVDF-based ferroelectric capacitors, we have systematically investigated the fatigue of P(VDF-TrFE) thin-film capacitors. The detailed experiments and interpretation are described in **Chapter 7**.

1.4 Outline of the thesis

This thesis is focused on the device physics related to the ferroelectric polarization in P(VDF-TrFE) thin films. Our investigation is based on macroscopic electrical measurements and nanoscale scanning probe measurements. Modeling at mesoscopic level is involved. The main text of the thesis is organized as following.

Polarization switching within the framework of the Landau-Ginzburg-Devonshire theory is discussed in **Chapter 2** where we apply the Metropolis algorithm to simulate the evolution of ferroelectric domains. The polarization and strain as function of the electric field is simultaneously obtained.

The experimental details on device fabrication and measurements are described in **Chapter 3**.

In **Chapter 4**, the switching dynamics in disordered ferroelectric thin films is discussed. Transients of the polarization switching are systematically investigated at various electric fields and temperature. The transients are quantitatively interpreted. Using a random walk model we demonstrate that the observed switching dynamics can be attributed to a domain growth mechanism where domains are circular at low electric field with few nucleation sites, whereas at high field irregular entangled domains are formed.

We elaborate on the piezoresponse force microscopy investigation of ferroelectric domains in **Chapter 5**. By chemical etching of the top electrode of the ferroelectric capacitor, we are able to locally probe the bare surface of the pre-poled ferroelectric material. With this method, we systematically study the ferroelectric domains generated during polarization switching. We show for the first time an explicit correlation between the mean value of the out-of-plane piezoresponse phase and the macroscopic polarization. Reliability of the measurements has been demonstrated by comparing the remanent polarization measured before etching away and after re-evaporating the top electrode. The underlying origin for the retention of domains in bare ferroelectric thin films is discussed. The morphology of domains discussed in **Chapter 4** is directly visualized and presented in **Chapter 5**.

Depolarization in ferroelectric materials, an important data-loss process in memories, has been studied in pioneering works since the 1970s, albeit under quasi-static conditions. To study the dynamics of depolarization one resorts to the empirical Merz law, which gives the polarization switching time as a function of electric field, normalized to the so-called activation field. The Merz law has been used for decades; its origin as domain-wall depinning has recently been corroborated by first-principles-based molecular dynamics simulations. In **Chapter 6**, we experimentally investigate domain-wall depinning

by measuring the dynamics of depolarization in ferroelectric thin films. We find that the boundary between thermodynamically stable and depolarizing regimes can be described by a single constant, $P_{sat}/\varepsilon_0\varepsilon_{ferro}E_c$. Among different multidomain ferroelectric materials the values of coercive field, dielectric constant and polarization vary by orders of magnitude; the value for $P_{sat}/\varepsilon_0\varepsilon_{ferro}E_c$ however is comparable, implying a relation between activation-, depolarization- and intrinsic coercive field. We propose that the causality naturally holds, when domain-wall depinning originates from collective switching of polarized regions near pinning sites.

The polarization of the ferroelectric polymer P(VDF-TrFE) decreases upon prolonged cycling. Understanding of this fatigue behavior is of great technological importance for the implementation of P(VDF-TrFE) in random-access memories. In **Chapter 7** we study the fatigue in thin-film capacitors by systematically varying the frequency and amplitude of the driving waveform. We show that the fatigue is due to delamination of the top electrode. The origin is accumulation of gases, expelled from the capacitor, under the impermeable top electrode. The gases are formed by electron-induced phase decomposition of P(VDF-TrFE), similar as reported for inorganic ferroelectric materials. When the gas barrier is removed and the waveform is adapted, a fatigue-free ferroelectric capacitor based on P(VDF-TrFE) is realized. The capacitor can be cycled for more than 10^8 times without a sign of fatigue, approaching the programming cycle endurance of its inorganic ferroelectric counterparts.

Chapter 8 is a brief review on recent focus on the in-plane polarization. The in-plane component of polarization is attracting more and more interest as these studies reveal novel phenomena such as local insulator-metal transitions and topological phase transitions. Two topics are specifically chosen, which are charged domain walls and in-plane vortices. The understanding of the vortices may enable utilizing the new dimension, *i.e.* the in-plane component, of the polarization for novel non-volatile memory devices where the density of information storage is greatly enhanced.

Chapter 2 Theory of polarization switching

We have conducted Monte-Carlo simulations based on the Landau-Ginzburg-Devonshire theory. It is found that even in defect-free samples, polarization switching is not collective, but mediated with the formation and growth of domains; the extracted coercive field, however, is comparable with the intrinsic coercive field as derived from Landau theory for collective switching. Subsequently, disordered pinning sites are incorporated into the simulation. It is observed that the pinning sites act as nucleation centers during polarization switching. The presence of the disordered pinning sites significantly lowers the coercive field, turning the switching mechanism from intrinsic to extrinsic. By presuming a linear relation between the tentative flipping waiting time in the MC simulation with the realistic time, we have simulated the time-resolved domain configurations and polarization states. The hysteresis loops of the polarization and strain *vs.* electric field are simulated. The characteristics and their frequency dependence are in good agreement with experimental data.

2.1 Intrinsic and extrinsic switching

Polarization switching refers to the reversal of the macroscopic polarization under for instance applied electric field or mechanical stress. The microscopic origin of polarization switching is the reorientation of the dipoles which are either the polar ions in a ferroelectric ionic crystal or the polar monomers in a ferroelectric polymer. A polarization state with lower energy of the system is energetically more favoured. When an electric field against the polarization direction is applied, the dipoles tend to reorient to lower the free energy. Macroscopically this leads to polarization switching from an energetically instable (metastable) state to an energetically stable state.

Devonshire first introduced the Landau mean-field phase transition theory to ferroelectrics, known as the Landau-Devonshire (LD) theory [17] [16]. According to the LD theory, the free energy of the ferroelectric system is a single valued function of the mean polarization over the material. In this scenario, all the dipoles flip upon applied electric field collectively without spatial inhomogeneity. Later, the spatial gradient of the polarization is incorporated into the free energy, known as the Ginzburg term [28] and the developed theory is referred to as the Landau-Ginzburg-Devonshire (LGD) theory. The essential of the LGD theory is that the spatial inhomogeneity of the polarization is taken into account, hence the polarization is a function of position and the free energy is a functional of the spatial variant polarization and its gradient. Specifically, the extra Ginzburg term is the energetic penalty for spatial inhomogeneity.

The LD and the LGD theory elegantly characterize the coercivity and hysteresis of ferroelectric materials during polarization reversal. The polarization switching mechanism described by the LD or the LGD is commonly termed as the *intrinsic* switching. In intrinsic switching, macroscopic polarization reversal is hindered by a large energy barrier which can hardly be overcome by thermal fluctuations. The experimentally obtained coercive field, however, is typically an order of magnitude lower than that predicted by the LD or the LGD theory. For example, the coercive field of P(VDF-TrFE) predicted by the LD and LGD theory is in the order of magnitude of GV/m whereas that obtained experimentally is typically 50 MV/m.

Intrinsic switching is expected only in defect-free homogeneous ferroelectric single crystals. Practical ferroelectric materials contain disordered pinning sites which are sporadic spots with a polarization orientation opposite to the macroscopic polarization. When an electric field against the macroscopic polarization and higher than the coercive field is applied, these pinning sites tend to flip their neighbouring sites via Coulomb interaction and mechanical strain. Hence these pinning sites act as nucleation centers. The presence of the nuclei greatly lowers the energy barrier to the extent that can be overcome by thermal fluctuations; such a thermal activated process is termed as *extrinsic switching*. In extrinsic switching, the coercive field strongly depends on the temperature, and is typically much lower than the intrinsic coercive field.

In this Chapter, we conduct Monte-Carlo (MC) simulations based on the LGD theory. With the LGD coefficients, we determine the free energy as a function of the spatial variant polarization. The evolution of the domains is simulated via minimizing the free energy. Disordered pinning sites are incorporated into the simulation. By assuming a linear relation between the tentative flipping waiting time in the MC simulation with the realistic time, we have simulated the time-resolved domain configurations and polarization states. The hysteresis loops of the polarization- and strain *vs.* the electric field are simulated. The characteristics and their frequency dependence are in good agreement

with experimental data.

2.2 Landau-Ginzburg-Devonshire theory

Based on the mean-field phase transition theory of Landau, Devonshire developed the free-energy description of a ferroelectric system, which is now referred to as the Landau-Devonshire theory. In a homogeneous ferroelectric material, the macroscopic polarization, *P*, is chosen as the order parameter, with which the free energy is expanded as:

$$F(P) = \frac{1}{2}\alpha P^2 + \frac{1}{4}\beta P^4 + \frac{1}{6}\gamma P^6 - EP \tag{2.2.1}$$

where α, β and γ are Landau coefficients, and *E* is the electric field within the ferroelectric material. The last term in the right hand side of Eq. (2.2.1) implies that the electric field tends to align the polarization parallel to the field to lower the free energy. The stability of the ferroelectric system requires the (local) minimization of the free energy, which reads:

$$\begin{aligned} &\frac{\delta F}{\delta P} = 0 \\ &\frac{\delta^2 F}{\delta P^2} > 0 \end{aligned} \tag{2.2.2}$$

The solution to Eq. (2.2.1) and Eq. (2.2.2) yields an explicit relation between the polarization, *P*, and the electric field, *E*. The calculated relation for P(VDF-TrFE), using the reported values for Landau coefficients [60] [61], is presented in Fig. 2.2.1 as the blue curve. The region between **a** and **b** is instable. At the position **a**, further increase of the electric field leads to macroscopic polarization reversal from **a** to **a'** as indicated by the black arrow, and so is the case from **b** to **b'**; the positions **a** and **b** correspond to the coercive field.

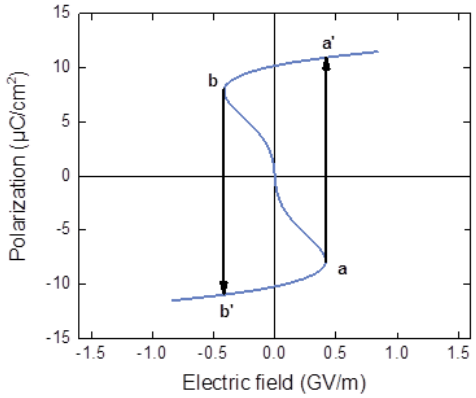

FIG. 2.2.1 The *P-E* relation for P(VDF-TrFE) calculated using Landau-Devonshire theory. The Landau coefficients are taken from Ref. [61].

The coercive field obtained here is about 0.5 GV/m, which is an order of magnitude higher than the experimentally obtained value. We notice however, that different values for the Landau coefficients are also reported [62], which leads to a coercive field of about 1.5 GV/m.

Ginzburg took the spatial inhomogeneity of the order parameter and the energy expense in forming domain walls into account. Later, other contributions such as the coupling between polarization and mechanical stress and the dipole-dipole interaction were incorporated into the free energy. Generally, the full-termed free energy reads [63]:

$$F = \int \left(f_L + f_E + f_G + f_{el} + f_{es} + f_{dip} \right) \cdot d\mathbf{r} \tag{2.2.3}$$

where the terms on the right-hand side refer to Landau-Devonshire energy, electrostatic energy, Ginzburg gradient energy, elastic energy, electrostrictive energy and dipole-dipole energy, respectively.

We consider the out-of-plane domains. The order parameter is the normal component of polarization, P_3. The mean-field Landau-Devonshire energy, f_L, is formulated as an expansion to P_3, to sixth order, which reads:

$$f_L = \frac{\alpha_0 (T - T_0)}{2} P_3^{\,2} - \frac{\beta}{4} P_3^{\,4} + \frac{\gamma}{6} P_3^{\,6} \tag{2.2.4}$$

Here, P_3 denotes the z-component of polarization. α_0, β, γ and T_0 are phenomenological parameters, and their values have been determined by molecular-dynamics simulations [62] or experiments on Langmuir-Blodgett P(VDF-TrFE) ultrathin films [61].

f_E is the electrostatic energy when the ferroelectric material is exposed to an electric field, E, which reads:

$$f_E = -\frac{1}{2} \varepsilon_0 \varepsilon_r E^2 - E \cdot P_3 \tag{2.2.5}$$

where ε_0 is the vacuum permittivity and ε_r is the dielectric constant of the ferroelectric material.

The Ginzburg term, f_G, describes the energy expense caused by domain walls where there are polarization gradients. As we only consider the polarization normal to the film, in the free energy only the terms with ∂P_3 are included. In ferroelectric thin films, it is a reasonable simplification to disregard the gradient perpendicular to the film, *i.e.* $\partial P_3/\partial z$ is regarded as zero. Hence the Ginzburg term can be expressed as:

$$f_G = \frac{K_1}{2} \left(\frac{\partial P_3}{\partial x} \right)^2 + \frac{K_2}{2} \left(\frac{\partial P_3}{\partial y} \right)^2 \tag{2.2.6}$$

where K_1 and K_2 are gradient coefficients related to the energy expense in creating polarization gradients in the transverse direction and along the chain respectively.

As an elastic medium, the ferroelectric material stores the elastic energy, f_{el}, when there is elastic displacement. Here only the elastic displacement normal to the film is considered. In addition, we

ignore the shear stress. With these simplifications, we write the elastic energy as:

$$f_{el} = \frac{1}{2} c_{33} u_3^{\,2} \tag{2.2.7}$$

where c_{33} is the elastic constant and u_3 is the strain normal to the film.

f_{es} is the electrostrictive energy. Similar as dealing with the elastic energy, here we only consider the *z*-component of the response to the *z*-component of input. The electrostrictive term then reads:

$$f_{es} = -Q_{33} u_3 P_3^{\,2} \tag{2.2.8}$$

where Q_{33} is the electrostrictive coupling coefficient.

f_{dip} is the energy corresponding to the dipole-dipole interaction. Due to this term, the ferroelectric system favours head-to-tail dipole alignment. In our current work, in-plane polarization is not taken into account, and the polarization normal to the film is regarded as identical. The energetic difference caused by dipole-dipole interaction then is orders-of-magnitude less than that caused by the previous terms. For computing convention, we let $f_{dip} \equiv 0$.

With the full-termed free energy, the remaining task is to find its minima at a given electric field. The free energy now is no longer a single valued function of the polarization, but a function of the spatial-variant polarization which is separated in to different domains. The evolution of the domains, equivalent to the evolution of the spatial distribution of polarization, **P**(**r**), is typically described by the Landau-Khalatnikov equation [61], also referred to as the time-dependent Ginzburg-Landau (TDGL) equation [62] [64]:

$$\frac{\delta F}{\delta P_i} = -L \frac{\partial P_i}{\partial t} + \eta \tag{2.2.9}$$

where P_i denotes the *i*-th component of the polarization, L is a kinetic coefficient, and η is a is a random thermal noise function [62] [63].

An alternative approach in simulating polarization reversal is Monte-Carlo simulation using the Metropolis algorithm. The physical scenario is straightforward. Since the evolution of polarization and free energy is facilitated by thermal fluctuations of the local order parameter, one can directly model the variation of the local order parameter, δ**P**(**r**), instead of solving Eq. (2.2.9). Whether the variation is energetically favored is judged by its impact on the corresponding change of free energy, according to Boltzmann statistics: variations which lower the free energy have a higher probability to be accepted. With statistically large number of local variations, the domains evolve towards the configuration of minimum free energy. This approach has been successfully applied to study the domain pattern of $BaTiO_3$ films evolving from the paraelectric phase to the ferroelectric phase at zero field [65] and has been applied to study the zero-field domains in restricted systems in equilibrium [66]. A recent work applied this MC method to study the electrocaloric effect in $BaTiO_3$ thin films [67].

We note that all these aforementioned studies are on inorganic ferroelectric materials, and defects are seldom taken into account. Below we elaborate our Monte-Carlo simulation for P(VDF-TrFE)

ferroelectric thin films. We also take disordered pinning sites into account.

2.3 Monte-Carlo simulation

The Monte-Carlo simulation is performed on a 2D $N \times N$ square lattice with periodic boundary conditions. Each lattice site represents a 1 nm × 1 nm region. On the lattice site **r**, the local polarization in *z*-direction is denoted as $P_3(\mathbf{r})$. Note that $P_3(\mathbf{r})$ is the mean polarization within the corresponding 1 nm × 1 nm region, and takes values continuously ranging from $-P_s$ to $+P_s$, where P_s is the spontaneous polarization. The strain at the site **r** is denoted as $u_3(\mathbf{r})$. The simulation proceeds as follows. In each simulation cycle, a fluctuation is generated at a randomly chosen site. The strain/polarization at the site is randomly varied. Consequently, the free energy F is recalculated and compared with the value before the tentative variation to obtain the difference ΔF. The variation is accepted with the probability p:

$$p = \begin{cases} 1, & \text{if } \Delta F < 0, \\ \exp\left(-\Delta F / k_B T\right), & \text{if } \Delta F > 0. \end{cases} \tag{2.3.1}$$

In each simulation cycle, we update the values of P_3 and u_3 at a randomly chosen site by the standard Metropolis procedure for the relaxation of electric dipole and elastic strain in the lattice [66], and the macroscopic polarization and strain are the averaged values of local polarization, P_3, and local strain, u_3, over the whole film, denoted as P and u, respectively. Here, a reasonable assumption is that the response time of elastic strain is far shorter than that for dipole relaxation, such that when a new dipole moment is given, the mechanical equilibrium is instantly established [68] [69]. In our present simulation, we give ten times more chances to the strain relaxation, given one time for the dipole to relax so that the local mechanical equilibrium conditions can be satisfied. The number of simulation cycles scales with the dimension of the lattice system. We normalize it to the number of lattice, $N \times N$, defined as a single Monte-Carlo Step (mcs). 1 mcs means each lattice site have undergone a tentative flipping on average; its reciprocal value has the meaning of the generation rate of thermal perturbations to the dipoles.

Here, we have chosen $N = 100$, corresponding to a region of 100 nm × 100 nm. For each simulation, we let the system first evolve at zero-field for 10^5 mcs to reach equilibrium. Afterwards, a sinusoidal waveform of electric field is applied. Spatial distribution of polarization and strain is recorded in each mcs. The macroscopic polarization and strain is the average over lattice sites. The parameters used for simulation are listed in Table 2.3.1.

TABLE 2.3.1 The parameters used for P(VDF-TrFE).

α_0 **[60]** (Jm/C^2K)	T_0 **[13]** (K)	β **[13]** (Jm^5/C^4)	γ **[13]** (Jm^9/C^6)	K_1 **[62]** (Jm^3/C^2)	K_2 **[62]** (Jm^3/C^2)	c_{33} **[70]** (Pa)	Q_{33} **[4]** (m^4/C^2)	P_s **[71]** (C/cm^2)
7.5×10^7	306.7	1.9×10^{12}	1.9×10^{14}	2.108×10^{-8}	2.108×10^{-8}	2.5×10^9	-1.8	0.12

2.4 Effects of disordered pinning sites

The simulated *P-E* hysteresis loop subject to a sinusoidal electric field with an amplitude of 1.5 GV/m and a period of 1.7×10^7 mcs is presented in Fig. 2.4.1. This ramping frequency is chosen such that the *P-E* loop is simulated in a quasi-static. The simulated loop is presented with red curve in Fig. 2.3.1 (a) in which Fig. 2.2.1 is replotted in blue curve as a comparison. The remanent polarization, P_r, is 10 $\mu C/cm^2$. The coercive field is about 0.5 GV/m. Fig. 2.4.1 (b) is a snapshot of domain morphology at $P \approx 0.7P_r$. Spatial inhomogeneity of polarization can be seen, indicating that the polarization reversal is meditated by nucleation and growth of domains, a result of thermal fluctuations, in agreement with the observation in Ref. [62]. The spatial variation of the local polarization, though, is smooth, without sharp domain walls, in agreement with the TDGL simulations reported in Ref. [62]. For comparison, the *P-E* relation derived from the mean-field Landau-Devonshire theory, in which the physical scenario is the collective switching without nucleation and the formation of domains [72], is plotted with red curve in Fig. 2.4.1 (a). We find that inhomogeneous switching yields a similar coercive field as that for the collective switching. The *P-E* relation is also similar except for the instable region. Therefore, a defect-free ferroelectric thin film is expected to exhibit the properties of intrinsic switching, regardless if polarization switching is nucleation-meditated or collective.

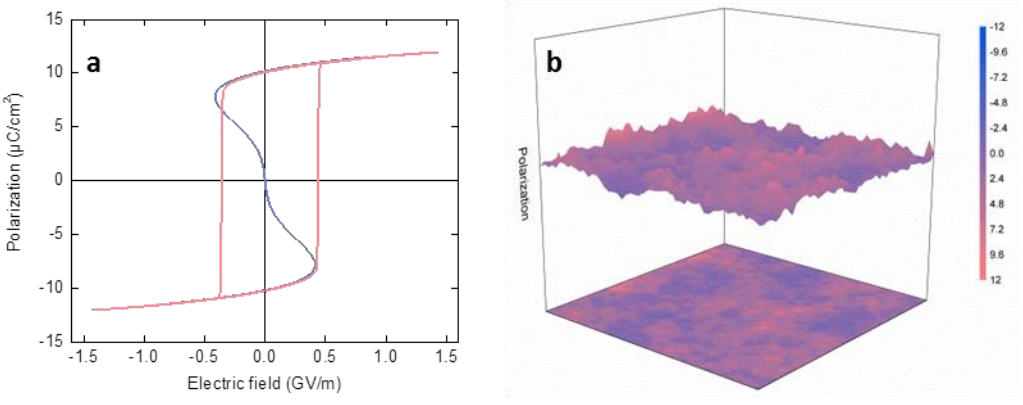

FIG. 2.4.1 *P-E* hysteresis loop and domains formation for P(VDF-TrFE) thin films. (a) The blue curve is analytically calculated using Landau-Devonshire theory where the polarization is the z-component of P_3 averaged over the whole film. The red curve is obtained by the Monte-Carlo simulation with the full-termed free energy, *c.f.* Eq. (2.2.3). (b) The distribution of polarization in a 50 nm × 50 nm region, snapshotted at a macroscopic polarization of about $0.7P_r$.

Commonly used ferroelectric materials are polycrystalline thin films or ceramics that are by nature not defect-free [73] [35] [74]. There is energetic and spatial disorder due to, for instance, misfit dislocations [75] [76], defects in conformation and molecular packing of macromolecular chains [34], and grain boundaries [77] [78]. The presence of these defects lowers the barrier for polarization reversal. The macroscopic polarization switching in ferroelectric materials with defects involves anisotropic growth of individual domains, termed as extrinsic switching [29]. Here we simulate a P(VDF-TrFE) thin film with defects. We specifically investigate the effects of the pinning sites, *i.e.* the sporadic small regions with fixed polarity which cannot be switched by an applied electric field. To maintain a metastable polarization within these regions, a typical dimension as several nanometers is calculated, termed as the size of critical nuclei [79]. Pinning sites with a smaller dimension generate and annihilate in dynamic equilibrium, with net contribution to the macroscopic polarization. Here, a critical nucleus is modeled as one site with fixed polarity corresponding to a 1 nm × 1 nm region. We assume that the percentage of pinning sites with opposite polarity is equal. The presence of the pinning sites lowers the value of the remanent polarization; in an extreme case when all sites are pinned, *i.e.* 50 % are up and 50 % are down, the remanent polarization is zero. We have found that a density of 1.7 % yields a remanent polarization of 8 $\mu C/cm^2$, which is roughly the experimentally measured value.

With 1.7 % disordered pinned sites (half up and half down) introduced, we have studied the *P-E* hysteresis loop at various periods of the sinusoidal electric field counted in Monte-Carlo Steps (mcs). The derived coercive field against the period of the electric field is presented in the inset of Fig. 2.4.2. The coercive field decreases with increasing value of the period counted in mcs. With the frequency-dependence of coercive field known from experiments, we can correlate the Monte-Carlo Step, mcs, with the elapsed time, *t*, assuming:

$$mcs = Rt \tag{2.4.1}$$

where R is a constant, the rate of the tentative flipping in the Monte-Carlo simulation, or the generation rate of the thermal perturbations in the scenario of thermally activated dipolar flipping. When $R = 10^{10}$, we find good agreement between the simulated results and the measured results in the frequency dependence of the coercive field, as presented in Fig. 2.4.2. We notice that the tentative flipping, or generation rate of perturbations, could relate to the phonon modes as discussed in Ref. [80] where a frequency of 10^{12} has been taken.

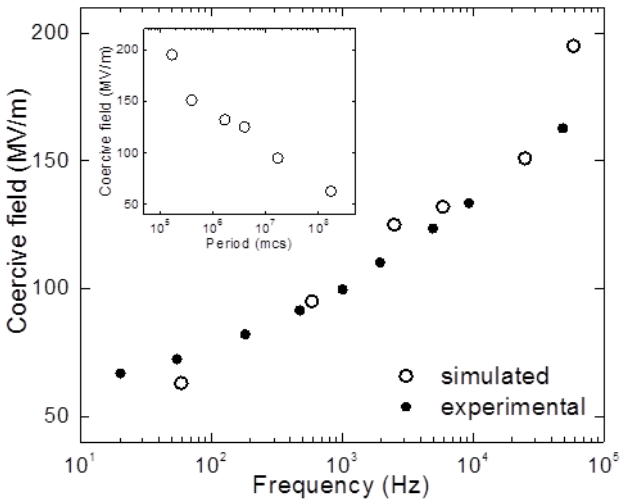

FIG. 2.4.2 Frequency dependence of the coercive field. The solid symbols are experimentally measured. The hollow symbols are obtained from the Monte-Carlo simulation and the frequency is derived as *R*/*mcs*, *c.f.* Eq. (2.4.1). The inset shows the dependence of the simulated coercive field on Monte-Carlo Steps (mcs).

With Eq. (2.4.1) and $R = 10^{10}$, we have then correlated our simulated results counted in mcs with the results measured as a function of frequency. The *P-E* loop and the strain, *S*, vs. the electric field, the *S-E* loop simulated for a 100 nm × 100 nm P(VDF-TrFE) thin film are presented in Fig. 2.4.3 (a) and Fig. 2.4.3 (b) respectively. The ramping electric field has a sinusoidal waveform with amplitude of 300 MV/m and frequency of 0.5 kHz. Our simulation yields a coercive field of about 90 MV/m at 0.5 kHz, in good agreement with experimentally obtained value. The piezoelectric coefficient, d_{33}, extracted from simulated *S-E* loops yields about -5 pC/N. We note that this d_{33} counts only the contribution from the crystalline part. In reality, the coupling between the crystalline part and the amorphous part also contributes to the piezoelectric coefficient, which leads the value of d_{33} extracted from measurements to be about -30 pC/N [4].

The domain morphology and the distribution of the strain are simultaneously obtained. The domains and the local strain at three intermediate states are presented in Figs. 2.4.3 (c,e,g), (d,f,h), respectively. The least deformed regions (strain being zero) contour the domain wall. Note that the local polarization at one site is the value averaged over the 1 nm × 1 nm region.

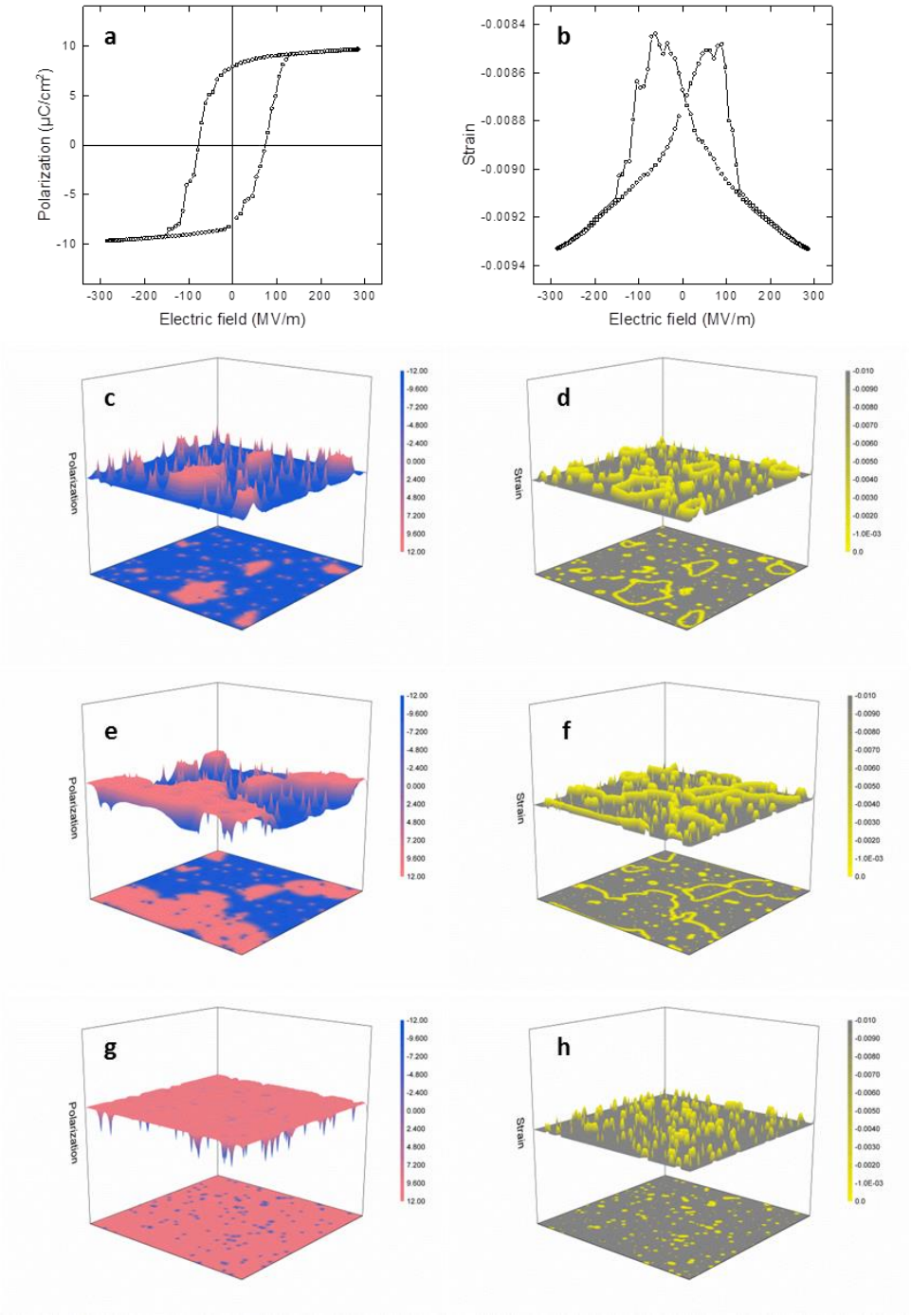

FIG. 2.4.3 Simulated results for a 100 nm × 100 nm P(VDF-TrFE) thin film with 1.7 % pinning sites. The frequency of the ramping electric field is 0.5 kHz. (a) The simulated *P-E* field loop, from which the coercive field reads about 90 MV/m. (b) The simulated *S-E* loop, from which the piezoelectric coefficient, d_{33}, is extracted as -5 pC/N. (c, e, g) The domain patterns at three intermediated polarization states. (d,f,h) The spatial distribution of strain at the intermediate polarization states corresponding to (c,e,g) respectively.

From the simulation it is clear that the pinning sites keep the dipoles in their vicinity parallel to their own polarity. The presence of pinning sites leads to strong spatial inhomogeneity; domains with opposite polarity can be clearly seen. The domains are highly irregular and entangled, which agrees with the morphology of the out-of-plane domains measured with piezoresponse force microscopy.

2.5 Summary

In this Chapter, we have studied the polarization switching in ferroelectric thin films based on the Landau-Ginzburg-Devonshire theory. A full-termed free energy is used, consisting of *e.g.* the Landau-Ginzburg term, the electrostriction energy and elastic energy. We have conducted the Monte-Carlo simulation using Metropolis algorithm where the tentative flipping is correlated with thermal perturbations. Due to thermal perturbations, even in defect-free samples, polarization switching is not collective, but mediated with the formation and growth of domains. Nevertheless, in defect-free ferroelectric thin films, the spatial inhomogeneity of the polarization is relatively small, and the extracted coercive field is comparable with the intrinsic coercive field derived from Landau theory for collective switching. Subsequently, disordered pinning sites are incorporated into the simulation. It is observed that the pinning sites act as nucleation centers during polarization reversal. The presence of the disordered pinning sites significantly lowers the coercive field, turning the switching mechanism from intrinsic to extrinsic. By assuming a linear relation between the tentative flipping waiting time in the MC simulation with the real time, we have simulated the time-resolved domain configurations and polarization states. The hysteresis loops of the polarization- and strain *vs.* the electric field are simulated. The characteristics and their frequency dependence are in good agreement with experimental data.

Chapter 3 Device fabrication and characterization

In this Chapter, we elaborate the details of the experiments conducted in this thesis, such as the device fabrication, electrical characterization and scanning probe microscopy methods. Electrical measurements based on the Sawyer-Tower circuit are the main technique used in this thesis. The measurements yield explicit values of the electric displacement a function of applied electric field, both quasi-statically and dynamically. To investigate depolarization, a linear capacitor with various values of capacitance in series with the ferroelectric capacitor is used to tune the compensation of the depolarization field in the ferroelectric material. The piezoresponse force microscopy is used to visualize the ferroelectric domains. Details about other auxiliary characterization techniques are described as well.

3.1 Spin-coated P(VDF-TrFE) thin films

Capacitors were fabricated on thermally oxidized silicon monitor wafers on which 50 nm thick Au bottom electrodes on a 2 nm Ti adhesion layer were photolithographically defined. Thin P(VDF-TrFE) films were spincoated at 2000 rpm from a 5 wt% solution in methylethylketone. The thickness, as measured with a DEKTAK surface profilometer, amounted to about 500 nm. To enhance the crystallinity and hence the ferroelectric properties, the samples were subsequently annealed in vacuum at 140 °C for 2 hours. A Au top electrode was evaporated through a shadow mask. The device area varied from 0.059 mm^2 to 1.38 mm^2. A photograph of the finished capacitor array and a schematic representation of the comprising capacitors' layout are presented in Fig. 3.1.1.

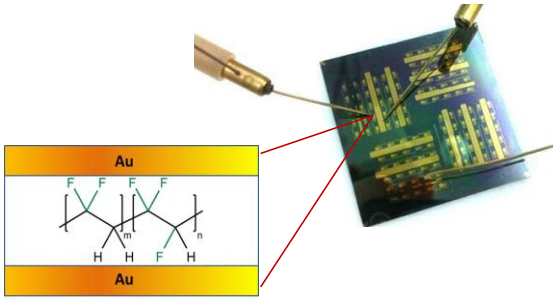

FIG. 3.1.1 A photograph of the finished capacitor array. The layout consists of discrete photolithographically defined Ti/Au bottom contacts with evaporated common Au top electrodes. The device area varies from 0.059 mm^2 to 1.38 mm^2. A schematic representation of the comprising capacitors' layout and the chemical structure of P(VDF-TrFE) are indicated. The thickness of the ferroelectric layer is about 500 nm.

3.2 Electrical measurements

Sawyor-Tower circuit

The electrical properties of ferroelectric capacitors are characterized by the Sawyer-Tower setup consisting of a Tektronix AFG3102 function generator, a LeCroy waverunner LT372 oscilloscope, a Krohn-Hite 7602M wide-band amplifier and a reference capacitor. The schematic of the Sawyer-Tower circuit is presented in Fig. 3.2.1.

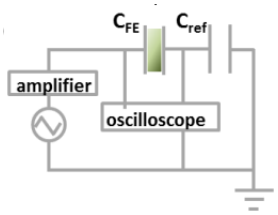

FIG. 3.2.1 A schematic of the Sawyer-Tower circuit.

A voltage is applied to the ferroelectric capacitor, C_{FE}, and the reference capacitor, C_{ref}, by the function generator through the amplifier, and is recorded through the first channel of the oscilloscope, denoted as U_1. The voltage on the reference capacitor is measured through a second channel of the oscilloscope, denoted as U_2. The polarization of the ferroelectric thin film is compensated by free charges at the electrodes. According to the Maxwell equation at the boundary of the ferroelectric material and the electrode, the density of free charges at the electrode is equal to the electric displacement, D, of the ferroelectric material. Therefore, at electrostatic equilibrium, the equations for the electric field and the electric displacement of the ferroelectric film as:

$$E_{FE} = (U_1 - U_2)/d \approx U_1/d \tag{3.2.1}$$

$$D_{FE} = C_{ref} U_2 \tag{3.2.2}$$

where d is the thickness of the ferroelectric capacitor. The reference capacitor is chosen such that U_2 is negligible compared with U_1 and, therefore, can be omitted in Eq. (3.2.1). The ferroelectric polarization, with the induced polarization excluded, of the ferroelectric thin film reads:

$$P = D - \varepsilon_0 \varepsilon_{FE} E \tag{3.2.3}$$

where ε_{FE} is the linear dielectric constant of the ferroelectric material, which is typically 3500 and 12 for PZT507 ceramics and P(VDF-TrFE) polycrystalline thin films respectively. Specifically, when E = 0, $P = D$ strictly holds, where the polarization is called remanent polarization. Generally, $P \approx D$ is a sufficiently good approximation. It is experimentally straightforward to measure D whereas P is convenient for discussion. In this thesis, except for conceptual description, we shall not emphasize the difference between P and D.

The characteristic *D-E* loop is measured by applying an alternating (AC) voltage. To eliminate the time during which the voltage amplitude is high, we choose a triangular waveform instead. The characteristic switching time of P(VDF-TrFE) is in the order milliseconds, and seconds for PZT ceramics. To quasi-statically measure the *D-E* loop, the applied AC voltage should have a frequency not higher than the reciprocal switching time. On the other hand, the reference capacitor discharges through the oscilloscope (impedance of 1 MΩ). For a reference capacitor of 680 nF, for example, the time constant for discharging is 0.68 s. This means, after 0.68 seconds, U_2 decreases to 1/e of its original value, although the polarization of the ferroelectric material does not change. Eq. (3.2.2) is severely violated when the measurement is longer than the time constant for discharging. Therefore the frequency of the applied AC should be higher than the reciprocal time constant for discharging.

From previous considerations we can see that there are two advantages of choosing a large reference capacitor: (i) it makes the approximation in Eq. (3.2.1) more accurate, (ii) it elongates the time constant for discharging. However, a too large reference capacitor leads to slow response of the reference capacitor to the polarization variation in the ferroelectric capacitor. This time constant is estimated as the RC constant of the reference capacitor and the resistance of the cable between C_{FE} and C_{ref}.

The RC constants are important in the transient measurements. We have carefully chosen the elements to eliminate the influence from RC.

Switching transient measurement

The switching transient has been measured on a Sawyer-Tower setup as schematically shown in Fig. 3.2.1. We apply a negative pulse to fully polarize the capacitor to $-P_r$. Subsequently, we short the capacitor to ensure that any extra charges at the electrodes are removed; only the compensating charges, equal to the remanent polarization, remain. We then apply a positive square pulse. The pulse duration is long enough to enable the ferroelectric thin film reach complete polarization reversal. We measure the voltage drop over the reference capacitor and hence obtain the polarization as a function of time. Afterwards, the same positive square pulse is applied to measure the non-switching contribution. Subtracting the two transients then yields the net polarization as a function of time. A typical measurement protocol is presented in Fig. 3.2.2, where the polarization has been normalized by $2P_r$. The difference from discrete Positive-Up-Negative-Down (PUND) measurements [74] is that only two pulses are needed to obtain the full polarization transient, *i.e.* the polarization as a function of time. The large number of quasi-continuous data points allows an accurate determination of the Avrami index. With this measurement procedure, fatigue is suppressed as the number of polarization reversals is drastically reduced. The experimental data are highly reproducible; after measuring the full data set, the original polarization transients were reproduced, yielding similar values for the fitting parameters.

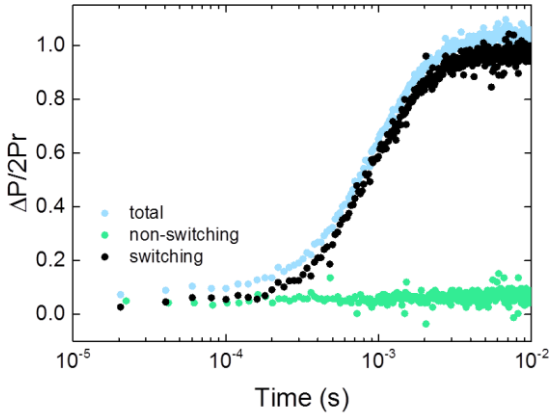

FIG. 3.2.2 Typical example of a measured polarization transient. After fully polarizing the capacitor to $-P_r$ and shortening the contacts for 10 s, a positive square pulse is applied. The blue dots present the total change of the charge on the reference capacitor after the first pulse. The measurement is repeated using a second positive square pulse. The green dots represent the non-switching dielectric contribution. The black dots are obtained by subtracting the two transients and represent the net polarization.

Quasi-static measurements of polarization and strain vs. electric field

The quasi-static measurements are performed with a Radiant Precision Multiferroic Test System (Radiant Technologies, Inc.). The fundamental principle is the same as the Sawyer-Tower circuit, with improvement in preventing the discharging of the sensing elements hence enabling measurements at a frequency as low as 0.1 Hz with acceptable accuracy. During the voltage sweep, the electric displacement and the strain, *i.e.* the relative change in thickness, are simultaneously obtained. The strain is obtained by measuring the mechanical displacement of a bulk electrode on the thick ferroelectric sample during polarization variation.

Tuning the internal electric field by a serial capacitor

In a conventional Sawyer-Tower circuit, a voltage, V_{app}, is applied to a ferroelectric capacitor and subsequently the electric displacement, D, of the ferroelectric material is measured over a reference capacitor. The internal field in the ferroelectric material, E_{ferro}, is derived as the applied voltage divided by the thickness, d, of the ferroelectric material.

To study suppression of polarization we use a linear capacitor, C_{ser}, in series with the ferroelectric capacitor, C_{ferro}. The applied voltage is then shared by the linear capacitor and the ferroelectric capacitor, and reads:

$$V_{app} = V_{ferro} + V_{ser} \tag{3.2.4}$$

where V_{ferro} and V_{ser} are the voltage drops over the ferroelectric- and serial capacitor, respectively. The values can be given as:

$$V_{ferro} = \frac{Q_{ferro} - PA}{C_{ferro}} \text{ and } \quad V_{ferro} = V_{app} - \frac{Q_{ser}}{C_{ser}} \tag{3.2.5}$$

where P and A are the ferroelectric polarization and the surface area of the ferroelectric capacitor, respectively. To satisfy the electro-neutrality between C_{ferro} and C_{ser}, $Q_{ferro} = Q_{ser} = V_{ferro} C_{ferro} + PA$, we get:

$$V_{ferro} = \frac{C_{ser}}{C_{ser} + C_{ferro}} V_{app} - \frac{PA}{C_{ser} + C_{ferro}} \tag{3.2.6}$$

We note that this equation is identical to Eq. (2) in Ref. [81]. Experimentally, the electric displacement, D, is directly extracted from the Sawyer-Tower measurements, and is regarded as fundamental variable [82]. To obtain the internal field within the ferroelectric material, we eliminate the ferroelectric polarization, P, by noting that:

$$D = \frac{\varepsilon_0 \varepsilon_{ferro} V_{ferro}}{d} + P \tag{3.2.7}$$

As the area of the ferroelectric capacitor, A, is given by $C_{ferro}d/\varepsilon_0\varepsilon_{ferro}$, the electric field inside the ferroelectric material is derived as:

$$E_{ferro} = \frac{V_{app}}{d} - \frac{D}{\varepsilon_0 \varepsilon_{ferro}} \times \frac{C_{ferro}}{C_{ser}} \tag{3.2.8}$$

Using the expression for the depolarization field, $E_{dep} = -P/(\varepsilon_0\varepsilon_{ferro})$, and taking Eq. (3.2.8), we get:

$$E_{ferro}(t) = E_{dep} \times \frac{1}{1+\left(C_{ferro}/C_{ser}\right)^{-1}} = -\frac{P(t)}{\varepsilon_0 \varepsilon_{ferro}} \times \frac{1}{1+\left(C_{ferro}/C_{ser}\right)^{-1}} \tag{3.2.9}$$

As compared to a single ferroelectric capacitor, the internal field relates to the depolarization field, E_{dep}, tuned by the ratio of the capacitances of the ferroelectric- and the linear serial capacitor, C_{ferro}/C_{ser}.

This net field by a serial capacitor is also schematically indicated in the sketch below:

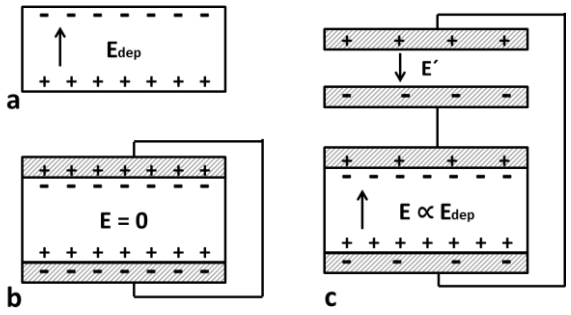

FIG. 3.2.3 Schematics of compensation of depolarization field. (a) Depolarization field in a free-standing ferroelectric material. (b) Ferroelectric-only capacitor. (c) Ferroelectric capacitor with an additional serial capacitor.

For a ferroelectric-only capacitor the charges in the electrodes fully compensate the polarization, such that at zero bias there is no net field in the ferroelectric material. In case of an additional serial capacitor, where due to charge neutrality the amount of free charges on both capacitors is equal, the depolarization field is not fully compensated. This leads to a net field inside the ferroelectric capacitor that is opposite to the electric field in the serial capacitor. At zero bias therefore the voltage drop over both capacitors is equal, but of opposite sign, such that the total voltage is zero. The smaller the capacitance of the serial capacitor the higher the net field in the ferroelectric material will become, as demonstrated by Eqs. (3.2.8) and (3.2.9).

Transient displacement measurements during depolarization

We first fully depolarized the ferroelectric capacitor by applying an alternating voltage with decreasing amplitude [83]. Subsequently the linear capacitor was discharged by shorting the electrodes, to ensure electro-neutrality between the ferroelectric- and linear capacitor. Then we applied a square pulse over the serially connected capacitors. The amplitude was high enough to fully polarize the ferroelectric capacitor. Contrary to quasi-static Sawyer-Tower measurements, the applied voltage was abruptly set to zero Volt and the resulting transient of the electric displacement, $D(t)$, was recorded.

Fatigue measurements

The degradation of polarization with poling cycles and time was performed on a Radiant Precision Multiferroic Test System (Radiant Technologies, Inc.) using a bipolar triangular or sinusoidal waveform. The frequency and amplitude were varied deliberately. After a preconfigured number of cycles the remanent polarization was determined by a positive-up-negative-down (PUND) measurement. We investigated scaling of fatigue with device area. Within device to device variations we could not identify statistically significant differences in programming cycle endurance.

Scanning electron micrographs were acquired with a Hitachi SU8000 SEM. The sample was exposed under analytical SEM working conditions, using a 10 kV acceleration voltage with an extractor working current of 20 μA, corresponding to a probe current of 1.1 nA. Micrographs were recorded intermittently during the exposure using a low voltage of 1 kV, at a probe current of ~ 50 pA. The top electrode of the capacitor was grounded using carbon tape.

3.3 Piezoresponse force microscopy (PFM)

We have developed a *global excitation and local probe* method for PFM investigation of domains with high resolution. Ferroelectric polarization as a function of electric field was measured using a Sawyer-Tower circuit as described previously. PFM measurements were conducted on a Bruker Dimension Icon Scanning Probe Microscopy (Bruker, Germany) using SCM-PITW probe (Bruker, Germany, conductive: 2.8 N/m 75 kHz, Pt/Ir Coating). We have chosen an AC frequency of 15 kHz and an amplitude of 5 V, significantly below the coercive voltage (30V for a 500 nm film); hence the PFM measurements did not affect the ferroelectric polarization. The topography and the PFM phase were obtained simultaneously from the same region.

To chemically remove the top electrode, we used a solution of I_2/KI/H_2O with weight ratio of 1:4:40. A drop of the Au etchant was dripped on the surface of the top electrode. After 20 seconds, the drop with the dissolved Au was sucked back with a glass pipet without touching the sample. After this process, the PFM tip directly scanned the exposed ferroelectric film.

PFM detects the local piezoelectric deformation of a sample caused by an applied electric field from the tip of a scanning force microscope. Regarding details on the operational mechanism we refer to one of the numerous reviews [84]. In most PFM publications only images of the out-of-plane phase are shown. The piezoelectric response of the sample is either in phase or out of phase with respect to the alternating voltage applied to the tip. The PFM phase therefore, ideally, only yields two values, namely 0° and 180°. We note that even if the polarization vector is not oriented exactly normal to the sample surface, the phase still yields one of these two binary values.

The displacement of the PFM cantilever induced by piezoresponse is proportional to the piezoelectric coefficient, d_{33}, and is consequently proportional to the polarization [46]. Since d_{33} of P(VDF-TrFE) is negative [4], an out-of-plane phase of 0° means that the polarity of the domains is opposite to the PFM tip (henceforth referred to as "up" domain), hence a positive tip bias results in an expansion of the domain and the piezoresponse is in-phase with the driving voltage; correspondingly, a phase of 180° indicates that the polarization of the domain points away from the PFM tip ("down" domain). In practice however, due to the finite size of the PFM tip, ultrafine structures, *e.g.* atomic-scale domains, cannot be fully resolved by PFM. This leads to smeared domain images and spatially averaged values for the phase [48], which can then assume continuous values between 0° and 180°.

After the PFM measurements, we re-evaporated Au on the samples as the new top electrodes. The new top electrodes can easily be aligned as the capacitor arrays have a cross-bar layout. After re-evaporation, we measured the remanent polarization with the Sawyer-Tower setup. The unchanged polarization verified the liability of the PFM measurements.

Chapter 4 Switching dynamics in disordered ferroelectric thin films*

Switching, *i.e.* polarization reversal, of disordered ferroelectric P(VDF-TrFE) thin films has been investigated at a wide range of applied electric field and temperature. The measured polarization transients can be quantitatively described by a compressed exponential function as originally formulated by Kolmogorov, Avrami and Ishibashi (KAI model). The phenomenological parameters switching time and Avrami index are related to the velocity and morphology of domain walls, respectively. We show that the switching time depends exponentially on electric field as described by the Merz law. The experimentally obtained Avrami index is independent of temperature but decreases with applied electric field from 1.55 at low field to 1.0 at 300 MV/m, indicative of an out-of-equilibrium dynamics of the growing domains. Using a random walk model we demonstrate that the observed switching dynamics are in agreement with a domain growth mechanism where domains are circular at low electric field with few nucleation sites, whereas at high field irregular entangled domains are formed. The density of nucleation sites is extracted as 1.5 % of the monomeric units in our work. Switching transients on capacitors where the nuclei density has been artificially increased exhibit 1D-like growth, as predicted by our model.

* Publication: D. Zhao, I. Katsouras, K. Asadi, P. W. M. Blom, and D. M. de Leeuw, *Phys. Rev. B* **92**, 214115 (2015).

4.1 Kolmogorov-Avrami-Ishibashi (KAI) model

Before the invention of the computer, the sophisticated interactions of the dipoles at domain-walls made the general calculation of the dynamics of polarization switching based on the Landau-Ginzburg-Devonshire (LGD) theory unfeasible. In practical device level, it is often the physics relating to the macroscopic polarization at micron- or larger scale that is concerned: simulations based on full-termed LGD theory are on one hand limited by computing capability for investigating large areas and on the other hand often not needed. To phenomenologically describe the dynamics of polarization switching, a statistical model was developed, known as the Kolmogorov-Avrami-Ishibashi (KAI) model [30] [31] [32].

The KAI model describes the (extrinsic) switching as a process of the nucleation and unrestricted expansion of the domains in which the dipoles reorient from anti-parallel to the applied electric field to parallel to the applied electric field. The KAI model assumes that polarization switching of a uniformly polarized sample under an applied electric field E takes place in four steps: (i) nucleation of domains; (ii) longitudinal growth of domains in the direction of the applied electric field; (iii) transverse growth of domains; and (iv) coalescence of domains until the polarization in the entire region is reversed. For thin films, steps (i) and (ii) are orders of magnitude faster than the last two steps [42] [85]. The transient of the polarization switching, therefore, is dominated by the transverse growth and coalescence of domains. The change in polarization with time $\Delta P(t)$ is proportional to the area of growing sporadic domains S_i as [29]

$$\Delta P(t)/2P_r = 1 - \exp\left(-\sum_i S_i/S_0\right) \tag{4.1.1}$$

where S_0 is the area of the sample and Pr is the remanent polarization, *viz.* the saturated polarization at zero electric field. The basic assumption of the KAI model is that, once nucleated, a domain can unrestrictedly expand in an electric field as

$$S_i \sim (vt)^n \tag{4.1.2}$$

where v is a constant domain-wall velocity and t is the time. The normalized change in polarization can then be expressed by the compressed exponential function

$$\Delta P(t)/2P_r = 1 - \exp\left[-\left(\frac{t}{t_0}\right)^n\right] \tag{4.1.3}$$

where t_0 is a characteristic switching time. The Avrami index n depends on the dimensionality of the domains and takes only integer values; the value is 3 for single crystals and 2 for epitaxial thin films. For polycrystalline films, however, it is common experimental practice either to force the Avrami index n to be 2 or to consider it as an arbitrary fitting parameter. The switching time follows the empirical Merz law [86]:

$$t_0 = t_\infty \exp\left[\frac{E_{act}(T)}{E}\right] \tag{4.1.4}$$

where E is the applied electric field, E_{act} is the so-called activation field which is proportional to the domain-wall energy, and t_∞ is the switching time at infinite applied electric field. The Merz law is observed in many systems ranging from single crystals [86], through bulk ceramics [87] and thin films [42] [35], to organic-ferroelectric composites [88]. The KAI model and Merz law have been successfully applied to single crystals and epitaxial films. In disordered inorganic polycrystalline films, however, the switching dynamics, especially over long time scales, cannot be quantitatively explained by the conventional theory of homogeneous nucleation and domain growth. As summarized in Ref. [33], for any choice of parameters the function of Eq. (4.1.3) leads to a steplike shape on a logarithmic time scale that is nearly symmetric with respect to its inflection point. Polarization reversal reported for inorganic polycrystalline films, however, exhibits asymmetric curves with extended quasilinear tails. As a consequence, switching in these systems cannot be described by a single switching time t_0. Polarization switching is then explained by assuming a broad distribution of switching time over the polycrystalline film [42] [35] [33] [36]. The variation in switching time can be due to local variations in electric field.

The most commonly used organic ferroelectric material is the random copolymer of vinylidene fluoride with trifluoroethylene [P(VDF-TrFE)]. Polarization switching in this material has been extensively investigated [74] [89] [61] [34] [90] [91]. Switching in ultrathin Langmuir-Blodgett films is intrinsic [61], facilitated by a coherent, collective rotation of dipoles [72]. However, switching in thicker films is extrinsic, driven by nucleation of reversed domains and subsequent domain-wall motion. Polarization reversal has been measured as a function of composition of the copolymer, applied electric field, and temperature. Experimental techniques applied are piezoresponse force microscopy (PFM) and measurement of electrical displacement or switching current as a function of time. In general the switching time follows the empirical Merz law [Eq. (4.1.4)] and the polarization reversal can be described with the compressed exponential function of Eq. (4.1.3). Extracted Avrami indices vary between 1 and 5. An extremely high Avrami index has been ascribed to a delay in nucleation [43]. However, non-KAI mechanisms have also been reported, claiming that the switching could not be described by a single switching time and a unique Avrami index [33].

P(VDF-TrFE) is a semicrystalline polymer; the crystallinity is about 50% [26]. The microstructure depends on the molecular weight and its distribution, as well as on the processing details, such as the solvents and annealing conditions used. Polarization switching will in turn depend on the details of the microstructure and the presence of defects and structural disorder introduced in the synthesis of P(VDF-TrFE). Recently, the switching dynamics of P(VDF-TrFE) (70/30) have been systematically investigated over an unprecedentedly wide range of temperature, frequency, and electric field [74]. The data could be interpreted using Merz law and the KAI equation derived for nucleation and unrestricted growth of domains. The extracted Avrami index increased from 1 to 3 with both increasing electric field and increasing temperature. The value of 3 was interpreted as an indication of isotropic growth. Due to strong inter-chain coupling the domains nucleate and grow simultaneously in all directions. This conclusion is surprising, since the longitudinal growth, in the direction of the electric field, is much faster than the lateral, transverse growth.

We note that the determination of the Avrami index is challenging as it is extremely sensitive to the slope of the polarization transient at the inflection point. The polarization evolution with time was determined in Ref. [74] using a Positive-Up-Negative-Down (PUND) pulse sequence. A first pulse sets the polarization state. The following two pulses with opposite polarity to the first one then

measure the switching and non-switching polarization, respectively. The difference is the net switching polarization. The number of discrete data points however is limited, and we found that experimentally obtaining reliable data is hampered by *e.g.* depolarization during the waiting time and discharging of the reference capacitor in the Sawyer-Tower setup. Reliable values for the Avrami index could not be extracted. Therefore, we measure the full polarization transient using a previously reported yet overlooked procedure [89]. The accurately measured switching transient allows us to accurately determine both the switching time and the Avrami index. We show that the extracted Avrami index is independent of temperature and monotonously decreases with increasing electric field from 1.55 to 1.0. A random walk model is used to simulate the growing domains during polarization reversal. The concept is borrowed from stochastic models describing far-from-equilibrium dynamics [92] [93], such as spinodal phase decomposition. The calculated morphology varies from circular domains that corresponds to the conventional KAI model, to highly irregular, entangled domains as have been reported for PFM measurements on P(VDF-TrFE) nanomesas [34] and ultra-thin films [61]. The random walk model qualitatively explains the change in Avrami index with electric field and is used to estimate the density of nucleation sites.

4.2 Characteristic parameters extracted from switching transients

Avrami index

Polarization transients have been measured as a function of applied electric field and temperature. As an example, transients measured at room temperature at electric fields between 60 MV/m and 120 MV/m are presented in Fig. 4.2.1 (a). Similarly, transients measured at an electric field of 80 MV/m at temperatures between 253 K and 333 K are presented in Fig. 4.2.1 (b). The solid lines are fits to the compressed exponential function of Eq. (4.1.3). An excellent agreement is obtained. From the fit the values for the Avrami index n and the switching time t_0 are obtained. The extracted values of the Avrami index are presented as a function of applied electric field at temperature between 193 K and 333 K in Fig. 4.2.1 (c). The non-integer value is independent of temperature and monotonically decreases with applied electric field from 1.55 at low fields to 1.0 at 300 MV/m. This behavior is counter to the previous literature report [74] that shows an index that increases from 1 to 3 with both increasing electric field and increasing temperature. For completeness, the measured remanent polarization P_r is presented in Fig. 4.2.1 (d). The polarization is independent of temperature but slightly increases with increasing applied electric field, as reported earlier [26].

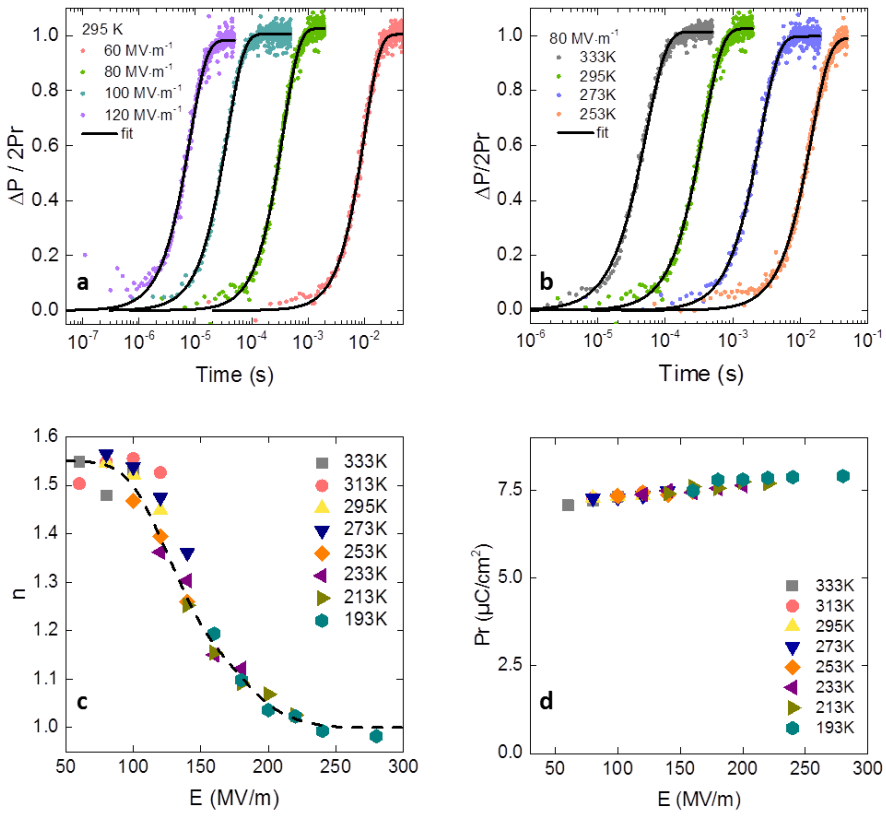

FIG. 4.2.1 (a) Typical polarization transients measured at room temperature at electric field between 60 MV/m and 120 MV/m. (b) Typical polarization transients measured at an electric field of 80 MV/m at temperatures between 253 K and 333 K. The solid lines are fits to the compressed exponential function of Eq. (4.1.3). (c) Extracted value of the Avrami index presented as a function of applied electric field between 50 MV/m and 300 MV/m at temperatures between 193 K and 333 K. The value is independent of temperature and monotonously decreases with applied electric field from 1.55 at low fields to 1.0 at 300 MV/m. The dashed line is a guide to the eye. (d) The measured remanent polarization, P_r, as a function of electric field at temperatures between 193 K and 333 K.

Switching time

The extracted switching time t_0 at temperatures between 190 K and 333 K is presented as a function of reciprocal electric field in Fig. 4.2.2 (a). The symbols show that the switching time follows the empirical Merz law as given by Eq. (4.1.4). The fitted lines are extrapolated to infinite electric field. The obtained value for the switching time at infinite applied electric field converges to 4 ns, in good agreement with reported values for P(VDF-TrFE) [74] [89]. From the polarization transients we estimate the order of magnitude of the domain-wall velocity as the lattice constant of 0.25 nm [94] over the switching time. The estimated domain-wall velocity at room temperature is presented in Fig. 4.2.2 (b) as a function of reciprocal electric field. For comparison, reported experimental values extracted by measuring the lateral growth of domains by PFM [95], represented by the orange dots, are included as well. A fair agreement is obtained at high electric field. The deviation at low electric field, corresponding to a very small domain-wall velocity, might indicate deviations from the Merz

law, as has been ascribed to the local disorder potential in literature [91] [96].

Activation field

The extracted values for the activation field vary from 800 MV/m to about 2500 MV/m, and are presented as a function of reciprocal temperature by the blue symbols in Fig. 4.2.2 (c). For comparison, previously reported values [74] for the activation field are included, represented by the green symbols. The solid line is a fit through the origin. A fair agreement is obtained.

The activation field is related to the domain-wall energy. In ferroelectric materials, regions with different polarization are separated by elastic domain walls. The application of an electric field favors one polarization state over the other. Dipolar reversal at the domain walls leads to domain-wall motion, which is typically described by a creep velocity [38]. The reciprocal domain-wall velocity is proportional to the switching time [32] [96]. In the creep of domain walls, the driving force is the applied electric field. The proportionality coefficient, E_{act}, is then directly proportional to the domain-wall energy according to the phenomenological model of Miller and Weinreich [37], given for the case when the depolarization energy of the opposite domain nucleus can be disregarded as [74]:

$$E_{act} = c\sigma_{dw}^2 / P_s k_B T \tag{4.2.1}$$

where c is the width of the domain wall that can be approximated by the lattice constant of the unit cell, s_{dw} is the domain wall energy, P_s is the spontaneous polarization, k_B is the Boltzmann constant and T is the absolute temperature. The 180°-domain-wall energy as extracted from the fit in Fig. 4.2.2 (c) amounts to about 60 mJ/m^2, in good agreement with the value reported in Ref. [74].

The activation field is typically much larger than the experimentally determined value of the coercive field. This means that the polarization actually reverses while the initial state is still metastable [97]. We present the value of the coercive field as measured using a triangular waveform with a frequency, f, of 100 Hz, as a function of the extracted activation field in Fig. 4.2.2 (d). The change of polarization with electric field, as observed in the hysteresis loop, depends on the rate at which the hysteresis loop is traversed and thus on both the frequency and waveform [97]. A few papers have addressed the relation between polarization, activation field and coercive field. A phenomenological expression has been suggested [98]:

$$E_c \approx \frac{E_{act}}{\ln(\gamma E_c) - \ln(16 f)} \tag{4.2.2}$$

where g may be regarded as the displacement velocity of domains per volt. For $BaTiO_3$ it was found that the term gE_c has a large value and can be approximated as a constant. The coercive field then depends linearly on activation field. The solid line in Fig. 4.2.2 (d) is a linear fit through the origin for P(VDF-TrFE), *cf.* Eq. (4.2.2). A qualitative agreement is obtained, which shows that the coercive field is about an order of magnitude lower than the activation field. We note that the coercive field is frequency dependent. In practice, typically a power-law dependence is reported [74] [99] [100].

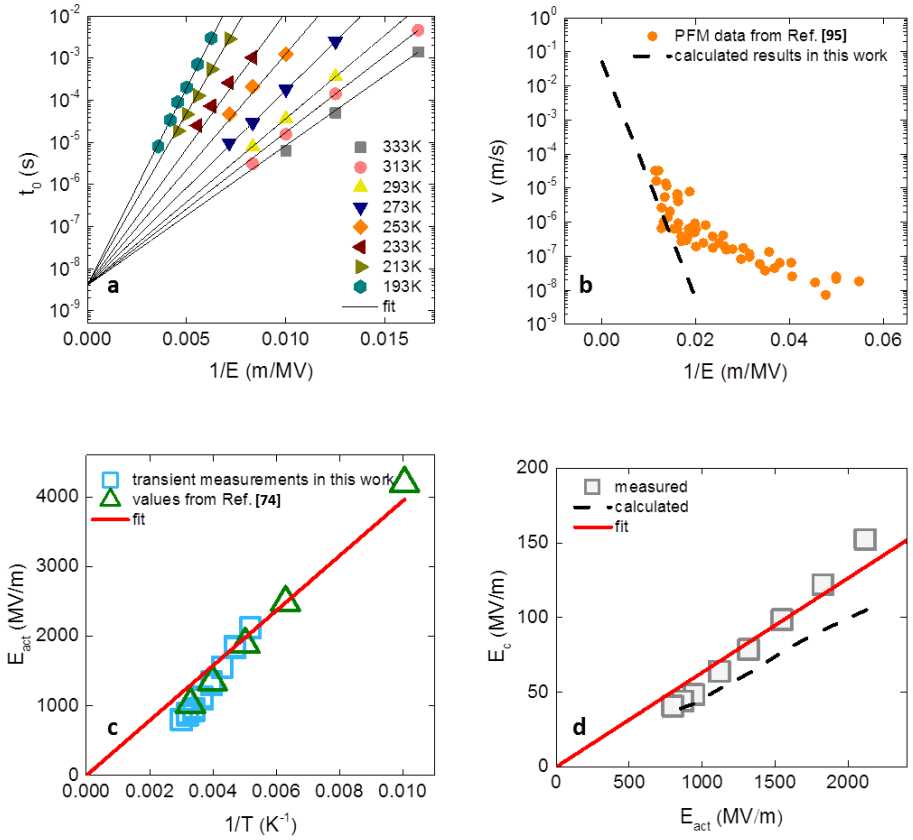

FIG. 4.2.2 (a) The characteristic switching time, t_0, as a function of reciprocal applied electric field. The lines are fits according to Eq. (4.1.4), extrapolated to zero reciprocal electric field. (b) Domain-wall velocity at room temperature as a function of reciprocal electric field. The black line is estimated assuming a velocity equal to the P(VDF-TrFE) lattice constant of 0.25 nm over the switching time. The dots are reported experimental values extracted from PFM measurements on growing domains [95]. (c) The activation field as a function of reciprocal temperature. The blue symbols represent the values extracted from the fit of the data in Fig. 4.2.2 (a) using Eq. (4.1.4). The green symbols represent the values reported in Ref. [74]. The solid line is a linear fit through the origin. (d) Coercive field measured at 100 Hz as a function of activation field. The red line is a linear fit through the origin. The black dashed line represents the coercive field obtained from the iteratively calculated hysteresis loops using Eq. (4.1.3).

The previously reported analytical relation between activation field and coercive field is purely phenomenological and relies on several assumptions and approximations. We can extract the activation field as a function of the coercive field directly from the measured transients, as follows. We iteratively calculate the hysteresis loop using the switching parameters, t_0 and n, extracted from polarization transients as input. To that end, we consider that a time-varying electric field, *e.g.* a triangular profile, is applied. Then at each time t, the electric field is known. The polarization at time $t + \Delta t$ follows from the polarization at time, t, as:

$$P(t+\Delta t) = P(t) + \left[P(\infty) - P(t)\right] \cdot \left[1 - e^{-(t/t_0)^n}\right] \tag{4.2.3}$$

where $P(\infty)$ is the saturated polarization. Hence the polarization can be numerically calculated as a function of time and converted into polarization as a function of electric field. From the resulting reconstructed hysteresis loops, the coercive field can be extracted and plotted as a function of the activation field. The results are represented by the dashed line in Fig. 4.2.2 (d). A reasonable agreement with the measured data is obtained.

4.3 Random-walk model for disordered ferroelectric thin films

Here we present a random walk model to qualitatively connect the switching transients and the Avrami index with the morphology of growing domains. P(VDF-TrFE) is a semi-crystalline polymer with a crystallinity of about 50% [26]. Polarization reversal will depend on the details of the microstructure. However, for simplicity, here we consider each monomeric unit as a single dipole. The film is then approximated as a single, uniform 2-dimensional square lattice of dipoles. In our capacitors the applied electric field is perpendicular to the film plane, hence we consider only out-of-plane switching. Initially, all dipoles are aligned except for a certain number of dipoles with a pinned, opposite orientation. These randomly distributed dipoles act as nucleation sites [29]. Chemical defects are regarded as the main origin [101]. Nucleation sites can also arise due to the presence of passive layers, such as oxidized or delaminated electrodes generated during device preparation and measurement [102] [103].

We apply abruptly an electric field to switch the dipoles. The system becomes metastable as it still maintains the initial macroscopic polarization. The energy of the electric field is much larger than the thermal energy, k_BT, hence the switching is an out-of-equilibrium process. The switching is triggered by the excess electrical energy. We model the polarization reversal as a series of N-step random walks. A single random walk is started. After stochastically dissipating the excess energy over N lattice sites, the random walk ends. A new random walk starts that again dissipates the excess energy over N lattice sites. The random walks ensue sequentially without temporal overlap.

The energy is dissipated regardless of the site's initial polarization state. However, when the dipole moment is opposite to that of the electric field, the dipole is flipped. The flipped dipole is stable only when it is in close vicinity to one or more flipped dipoles; otherwise the dipole immediately flips back. This implies that growth of domains with stable polarization reversal can only start at a nucleation site, despite the fact that the random walks are generated throughout the dipole lattice.

The higher the electric field, the more lattice sites, N, can be perturbed. Hence we call N the perturbation strength of a single random walk. We randomly generate a certain number of nucleation sites; their density normalized to the number of lattice sites is ρ_{nuclei}. Then we calculate the morphology as a function of N, and the cumulative number of random walks, τ.

Simulated domain morphology

Fig. 4.3.1 presents snapshots of the calculated morphology, extracted for a normalized polarization of about 35 %. The arrows indicate an increase in nucleation density and an increase in perturbation

strength. Fig. 4.4.1 shows that the geometry of the domains changes from circular to highly irregular. We first consider the limit of low nuclei density, the top row snapshots of Fig. 4.3.1. The single domains grow independently, without interference of other domains, provided that the perturbation strength is low. The growth then requires a large number of perturbations. In addition, at each point of the perimeter of the growing domains, the growth rate is the same due to statistical averaging of the perturbations. Consequently, the scenario of the conventional KAI model is reproduced and circular domains are obtained, as shown on the top left snapshot of Fig. 4.3.1.

With increasing perturbation strength, the domains become irregular; unflipped dipoles remain inside the domains as indicated by the sporadic white regions surrounded by the black regions. The growth rate at the perimeter of the domains gets anisotropic, as previously suggested by Monte-Carlo modeling [79].

When the nucleation density is high, then even at low perturbation strength the domains cannot grow unrestricted. As shown in the bottom part of Fig. 4.3.1, from the very beginning entangled domains are formed. Consequently, the conventional KAI model is not applicable. In the limit of a very high nuclei density, the domains are so close to each other that even small perturbations yield interconnected, entangled domains. The growth of entangled domains has been experimentally demonstrated by PFM measurements on both inorganic and organic ferroelectric materials, in $Pb(Zr,Ti)O_3$ (PZT) capacitors [42], $(PZT)_{0.95}(BiFeO_3)_{0.05}$ sol-gel thin films [104], $BiFeO_3$ thin films [40] and P(VDF-TrFE) crystalline nanomesas [34] or ultra-thin films [61].

Calculated switching transients

The change in polarization, ΔP, normalized by the remanent polarization, $2P_r$, is obtained as the number of flipped sites, the black regions in Fig. 4.3.1, over the total number of lattice sites. For all values of perturbation strength and nuclei density, the normalized polarization as a function of cumulative number of random walks can be perfectly described with a compressed exponential function:

$$\Delta P(\tau)/2P_r = 1 - \exp\left[-\left(\frac{\tau}{\tau_0}\right)^{n'}\right] \qquad (4.3.1)$$

by adjusting the fit parameters τ_0 and n'. The fit parameter τ_0 is the number of cumulative random walks needed to reach a normalized polarization of 63 %. Both τ and τ_0 are normalized to the number of lattice sites. The functional dependence of Eq. (4.3.1) is not surprising. The physical properties of systems in which the dynamics become progressively slower with time, are typically described by a compressed exponential function [105]. Compressed exponential dynamics are typically found for slow relaxation processes in out-of-equilibrium systems. An example is the change in physical properties of disordered quenched materials, such as glasses, gels and foams, during aging [105]: the physical properties depend on the time elapsed since the material was quenched, and the dynamics become progressively slower as the sample ages. Here, this condition holds for the calculated normalized polarization as a function of the number of random walks, since random walks within a domain do not contribute to its growth; only random walks at the perimeter of the domains can contribute. Hence the efficiency of random walks decreases with increasing normalized polarization.

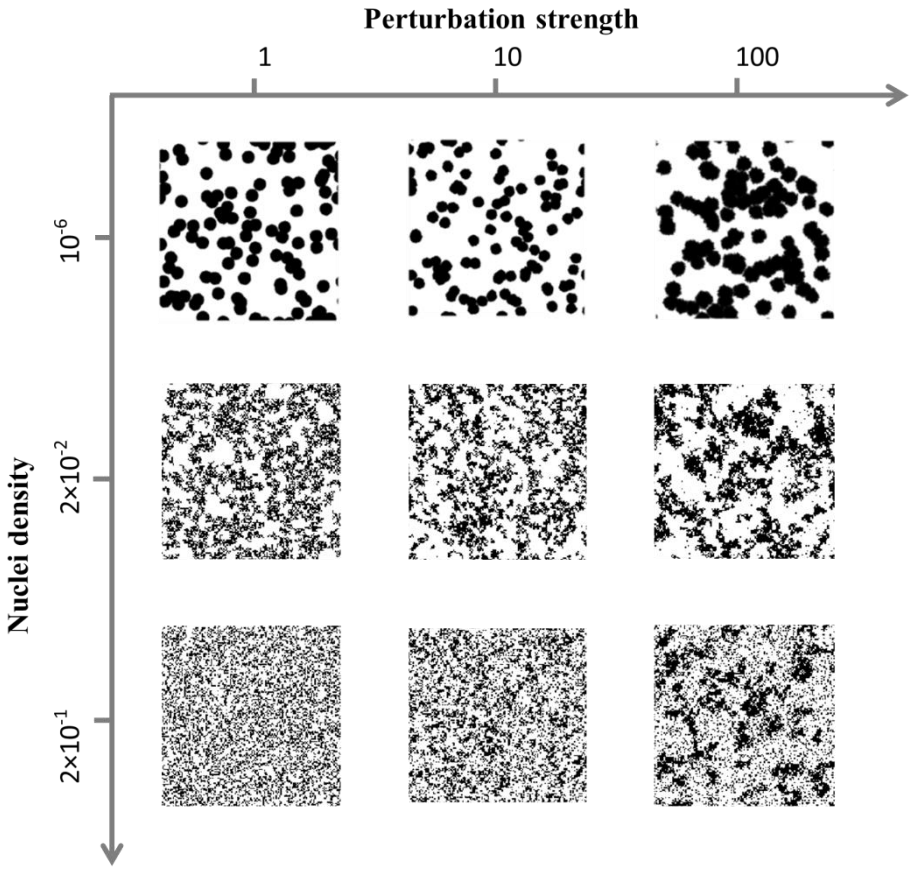

FIG. 4.3.1 Calculated domain morphology as a function of nuclei density, ρ_{nuclei}, and perturbation strength, *N*. The morphology is presented for a normalized polarization of about 35 %. Black areas represent flipped dipoles. The corresponding calculated Avrami indices are presented in Fig. 4.3.2 (a).

The extracted fitting parameters, *n'* and τ_0, are presented in Fig. 4.3.2 as a function of perturbation strength, *N*, for various nucleation densities, ρ_{nuclei}. The variation in the Avrami index, *n'*, correlates to the calculated domain morphology. At very low density of nucleation sites and moderate perturbation strength, domains are circular and grow unrestrictedly, as shown in Fig 4.3.1. The scenario for the conventional KAI model is reproduced and the calculated Avrami index, *n'*, is equal to 2, as expected. With increasing nuclei density and increasing perturbation strength, the domains no longer grow independently, but coalesce. Fig. 4.3.1 shows that in the limiting case, irregular, highly entangled domains are formed. This situation is characterized by an Avrami index of 1, indicative of growing 1D-wires.

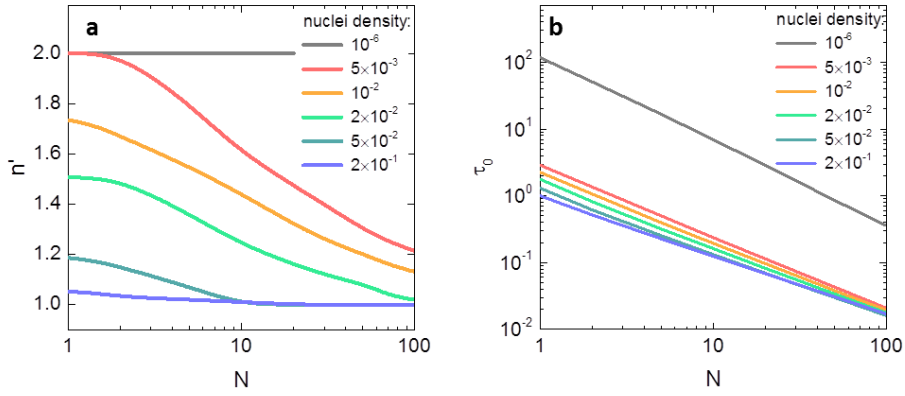

FIG. 4.3.2 (a,b) Values of the fitting parameters, n' and τ_0, as extracted from calculated normalized polarization as a function of cumulative number of random walks using Eq. (4.3.1). τ_0 is the number of cumulative random walks to reach 63% polarization reversal, normalized to the number of lattice sites. The values of n' and τ_0 are presented as a function of perturbation strength, N, and of the nuclei density, ρ_{nuclei}. The density of nucleation sites has been varied between 10^{-6} and 2×10^{-1}. The corresponding calculated domain morphologies are presented in Fig. 4.3.1.

The extracted value of τ_0 is presented in Fig. 4.3.2 (b) on a double logarithmic scale as a function of perturbation strength. We first consider the case in which the perturbation strength is unity, meaning that each random walk immediately ends after being generated. At very low nuclei density the random walk has a small probability of contributing to stable domain growth. Hence the number of random walks needed for polarization reversal is orders of magnitude larger than the number of lattice sites. However, the random walks get more effective when the nuclei density increases. At very high density, each random walk contributes to domain growth as is reflected by a value of τ_0 of about unity.

Now we increase the number of sites that a single random walk can reach. With a high value of N, almost all these steps are effective and contribute to growth. Hence τ_0 tends to depend linearly on $1/N$ as shown in Fig. 4.3.2 (b). At the same time, τ_0, the number of cumulative random walks to reach 63% polarization reversal, normalized to the number of lattice sites, corresponds to the switching time, t_0. Experimentally, the switching time depends exponentially on reciprocal electric field. We assume that τ_0 is directly proportional to t_0. Then, automatically, $\ln N$ increases with electric field, meaning that the number of sites each random walk can reach increases exponentially with electric field. The correlation between $\ln N$ and E implies that the Avrami index extracted from polarization transients, *cf.* Fig. 4.2.1 (c), may be compared with the Avrami index extracted from the random walk model, *cf.* Fig. 4.3.2 (a). The similarity implies that the monotonous decrease of the experimental Avrami index with increasing electric field is due to a change in morphology from circular domains to highly irregular entangled domains.

Verification of density of nucleation sites

Furthermore, regardless of the detailed relation between electric field and perturbation strength, the index extracted at low electric field is by definition identical to the index calculated at low

perturbation strength. The experimentally determined index converges to 1.55, *cf.* Fig. 4.2.1 (c). This value is obtained for a nucleation density of about 0.015, meaning that for 1.5 % of the monomeric units there is a nucleation site. Chemical defects are regarded as the main origin. A comparable density of head-to-head defects in PVDF between 6 % and 9 % has been derived from NMR measurements [24]. The nuclei density is expected to depend on the purity and molecular weight of the P(VDF-TrFE) polymer and the processing conditions of the capacitors. A systematic investigation was not attempted. We note however, that polarization transients on fatigued capacitors, where a high defect density is expected, indeed yielded an Avrami index close to unity. The dependence of Avrami index on morphology is corroborated by measuring capacitors where the nuclei density was artificially enhanced, as presented in Fig. 4.3.3. We start by depolarizing a capacitor. The polarization is close to zero meaning that initially about half of the dipoles are reversed. The microstructure, calculated by time-dependent Ginzburg-Landau approach, consists of small heterogeneous domains [62]. The reversed regions act as artificial nucleation sites. Polarization transients were measured. The extracted Avrami index is unity for all values of the applied electric field, as expected for a high nuclei density, *cf.* Fig. 4.3.2 (a).

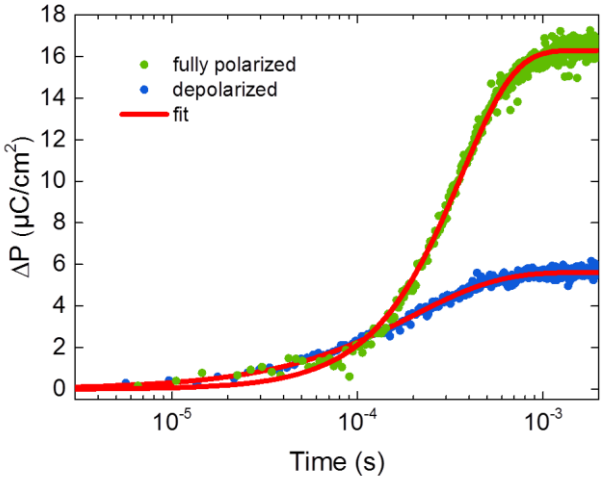

FIG. 4.3.3 Polarization transients measured at room temperature at an electric field of 80 MV/m of a depolarized and of a fully polarized ferroelectric P(VDF-TrFE) capacitor. The depolarized capacitor switches from the initial polarization of 0 to $+P_r$ (blue dots). The fully polarized capacitor switches from $-P_r$ to $+P_r$ (green dots). The solid red lines are fits to the data using Eq. (3.3.3) with n equal to 1 and 1.5, respectively.

4.4 Summary

In summary, we have investigated the switching dynamics of P(VDF-TrFE) thin films by measuring polarization reversal transients at a wide range of applied electric field and temperature. The transients can be described by a compressed exponential function using the characteristic switching time and Avrami index as fitting parameters. Contrary to literature reports the Avrami index is independent of temperature and decreases with applied electric field from 1.55 at low fields to 1.0 at 300 MV/m. The switching time depends exponentially on electric field as described by the Merz law.

The extracted activation field is an order of magnitude larger than the measured coercive field as confirmed by numerical calculations. A random walk model is used to simulate the growing domains during polarization reversal. The concept is borrowed from models describing far-from-equilibrium dynamics, such as spinodal phase decomposition. The monotonous decrease of the Avrami index with increasing electric field is due to a change in morphology from circular domains to highly irregular, entangled domains. The density of nucleation sites is derived as 1.5 % of the monomeric units. The modeling is supported by measuring polarization transients on capacitors where the nuclei density was artificially enhanced. The methodology may also be applied to investigate the dynamics of other binary systems with nucleation and non-equilibrium growth.

Chapter 5 Piezoresponse force microscopy study of ferroelectric domains

In this Chapter, the macroscopic polarization of a ferroelectric capacitor is correlated with the local domain morphology. To this end, a ferroelectric capacitor is poled to a set polarization state in a Sawyer-Tower setup. After chemically removing the top electrode, the exposed ferroelectric is locally probed with piezoresponse force microscopy. The domains without the top electrode are thermodynamically stable for weeks in ambient environment, as proven by comparing the remanent polarization measured before etching away and after re-depositing the top electrode. Out-of-plane PFM phase images show a random distribution of domains with up and down polarity. We unambiguously demonstrate a linear correlation between the mean PFM phase and the macroscopic polarization. As a demonstration of the insights the global excitation and local probing method can provide, we show how thermal and electrical depoling can result in identical macroscopic polarization, yet completely different domain morphologies.

5.1 Global excitation and local probing method

Scanning probe microscopy (SPM) techniques have revolutionized the field of ferroelectricity by providing an opportunity for non-destructive visualization of sub-micron ferroelectric domains [106]. One of the most widely used SPM techniques is piezoresponse force microscopy (PFM), which is based on monitoring piezoelectric surface deformation induced by the electrically biased probing tip [46]. The PFM technique was first developed in 1992 by Guethner and Dransfeld [39] to detect polarized regions in thin films of the ferroelectric random copolymer poly(vinylidenefluoride-trifluoroethylene) [P(VDF-TrFE)]. Since then the PFM technique has proven to be one of the most powerful approaches for sub-micron study of static domain morphology [40] [41], polarization switching [42] [43], domain-wall motion [38], non-linear dynamics of domains [44] and domain manipulation [38] [45] in a wide variety of ferroelectric materials.

In terms of exciting the sample, there are two main methods in PFM [46]: local or global excitation. In the local excitation method, there is no top electrode; the ferroelectric material is poled by the biased PFM tip, which scans the bare top surface of the sample. In the global excitation method, the ferroelectric material is poled in a capacitor using the top electrode, through which the domains are imaged by PFM.

The local excitation method allows *in situ* investigation of fine structures of domains [40] [41] and field-induced domain-wall motion [38] with high resolution. The drawback, however, is that the electric field generated by the PFM tip is inhomogeneous, which hampers quantitative analysis of the field-induced signal [46]. Moreover, the spot under the PFM tip acts as an artificial nucleation site. Due to the high local electric field, the tip actively drives the nucleation and domain growth process [45], which significantly differs from the scenario of stochastic nucleation and multi-domain growth during macroscopic polarization switching in a homogeneous electric field [29].

On the other hand, in the global excitation method, due to the presence of the top electrode, the sample is exposed to a homogeneous electric field. By using this method, the growth of domains could successfully be correlated to polarization switching transients [42] [43], verifying the statistical theory of multi-domain growth proposed by Kolmogorov, Avrami and Ishibashi [30] [31] [32]. Remarkably, the global excitation method allows one to quantitatively bridge the microscopic domains with the electrically measured macroscopic polarization. However, the major drawback of the global excitation method is that the resolution is limited due to the presence of the top electrode [47] [48].

We note that an alternative PFM method is to investigate in-plane capacitors, where both electrodes are in a common plane with the ferroelectric material on the substrate [49] [50]. The ferroelectric material is poled via the in-plane electrodes and probed by the PFM tip above the sample. This method generates a homogeneous electric field inside the ferroelectric material without sacrificing the intensity and resolution of the piezoresponse signal. However, unlike the top-view images by conventional PFM measurements, with planar capacitors one visualizes the lateral growth of the domains from side view.

To simultaneously achieve high resolution and a homogeneous poling electric field distribution, we report here a *global excitation and local probing* method. A ferroelectric P(VDF-TrFE) thin-film

capacitor is set to a given polarization state under an applied homogeneous electric field. Subsequently the top electrode is chemically etched away, without affecting the underlying ferroelectric layer. The exposed ferroelectric film can then be locally probed by a PFM tip with high resolution. We show that even without the top electrode the domains are thermodynamically stable for weeks in ambient environment; the possible origin is discussed. We unambiguously demonstrate a linear correlation between the mean out-of-plane PFM phase and the macroscopic polarization. As an application of the method, we visualize the domain morphologies of electrically and thermally depoled ferroelectric capacitors. We show that even when arriving at an identical final macroscopic polarization, the two depoling procedures result in widely different domain morphologies.

5.2 PFM phase analysis and macroscopic ferroelectric polarization

The schematics of a PFM tip scanning over “up” and “down” domains are presented in Fig. 5.2.1 (a).

Fig. 5.2.1 (b) shows a typical PFM topography of a partially polarized ferroelectric capacitor. The measurement was carried out on the surface of the 100 nm thick Au top electrode. The image shows the characteristic rice- or needle-like P(VDF-TrFE) grains [107]. The small particles on top of the needles are thermally evaporated Au granulates. The corresponding PFM phase image, which was measured simultaneously with the topography, is shown in Fig. 5.2.1 (c). The phase is spatially homogeneous. Discrete domains, as expected for a partially polarized ferroelectric thin-film capacitor, can hardly be detected. The lack of resolution is due to the presence of the thick top electrode, which damps the piezoelectric response of the underlying ferroelectric material, a well-known drawback of the global excitation method. To improve the resolution we therefore etched away the Au top electrode. The topography after the selective removal of the Au top electrode is presented in Fig. 5.2.1 (d). The topography before and after etching is similar, indicating that the P(VDF-TrFE) grains were unaffected. The PFM phase image after etching is shown in Fig. 5.2.1 (e). The resolution improved dramatically. Discrete domains locally probed by the PFM tip can clearly be distinguished. Hence, in our proposed method, we now can globally set the polarization of the capacitor using a Sawyer-Tower setup and locally measure the PFM phase of the ferroelectric layer after etching. We note that this procedure is only possible when the polarization remains stable even after removal of the top electrode. In the following sections we will demonstrate that this is indeed the case and provide a tentative interpretation.

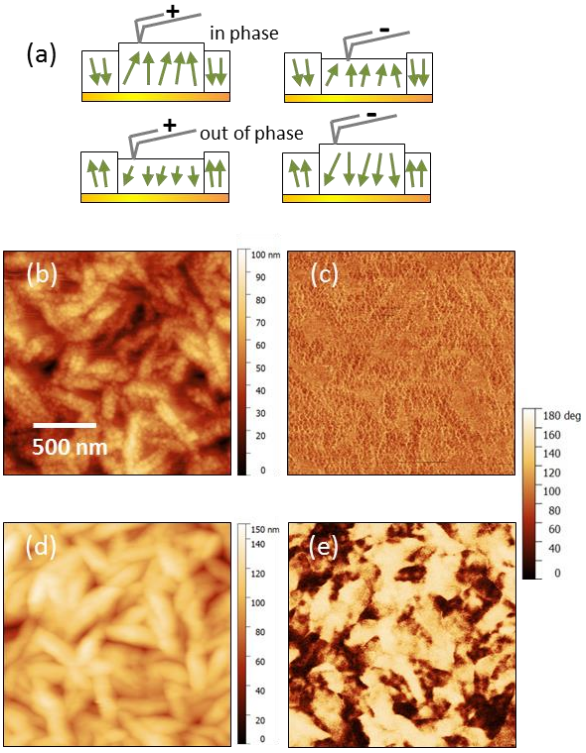

FIG. 5.2.1. Topography and out-of-plane PFM phase. (a) Schematics of the PFM tip scanning over "up" and "down" domains. (b) Topography of a P(VDF-TrFE) capacitor covered by a 100 nm Au top electrode. (c) The corresponding out-of-plane PFM phase. (d) Topography of the exposed P(VDF-TrFE) thin film after chemically removing the Au top electrode. (e) The corresponding out-of-plane PFM phase. The corresponding color bars indicate the height and the value for the out-of-plane PFM phase.

We have previously shown that the macroscopic polarization in a ferroelectric capacitor can be set to any value below the saturated polarization by designed voltage pulses [83]. Here we first polarized the P(VDF-TrFE) capacitor to the fully negative polarization state, $-P_r$. The polarization was consequently pointing down, away from the tip. Subsequently, we applied a positive voltage pulse with an amplitude of 30 V to set the P(VDF-TrFE) capacitor to a given intermediate polarization state, defined by the pulse duration, as shown in the inset of Fig. 5.2.2 (a). The corresponding transients of the electric displacement versus time for the two different pulse durations are presented in Fig. 5.2.2 (a). The final set polarization increases with increasing pulse duration.

In order to locally probe the ferroelectric polarization, we need to measure the PFM phase with high resolution. To this end, the top electrode was removed. The two PFM phase images corresponding to the two different final polarization states are presented in Fig. 5.2.2 (a). Additionally, we show the PFM phase image for the initial state corresponding to $-P_r$ as reference. The bright regions correspond to "down" domains, whose polarization is oriented away from the PFM tip. The fraction of the dark regions in the PFM phase images, which correspond to "up" domains, increases with increasing pulse duration.

To quantify the phase images, we analyzed the statistical distribution of the PFM phase values. The resulting histograms are presented in Figs. 5.2.2 (b-d). For the fully negatively polarized film, the phase exhibits a single peak at around 140°. The fact that the PFM phase deviates from 180° implies that the full saturation is not reached due to the presence of defects with misaligned polarity [29] [108]; moreover, a small portion of dipoles might have switched back when the applied poling field is removed [109] [110]. Upon applying the poling pulses, the polarization reverses as is reflected in the PFM phase images. The peak in the histogram at 140° that corresponds to fully negatively polarized P(VDF-TrFE), decreases; meanwhile a new peak at around 20°, corresponding to a fully positively polarized sample, appears. The presence of the two peaks in the histogram for the intermediate state reflects the presence of both "up" and "down" domains, which are spatially mixed.

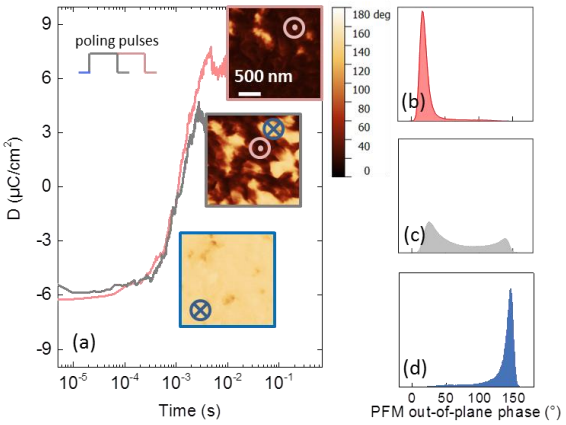

FIG. 5.2.2. Intermediate polarization states and corresponding PFM phase histograms. (a) Switching transients of two capacitors, which were fabricated on the same substrate. The capacitors were programmed to two different polarization states by voltage pulses with an amplitude of 30 V and a width of 3 ms and 5 ms, respectively, as schematically presented in the inset. The PFM phase images for the initial, fully negatively polarized, state and the two corresponding intermediate polarization states are shown. The notation ⊗ indicates a "down" domain, with a polarization oriented downwards in the plane of the substrate. The notation Θ indicates an "up" domain. (b-d) Statistical distribution of the PFM phase values for the initial and the two intermediate polarization states.

To correlate the phase with the macroscopic polarization, we quantitatively analyze the histograms of the PFM phase. For each P(VDF-TrFE) film, we calculate the mean value of the phase by integrating the histogram obtained for an arbitrarily chosen area of 5 μm × 5 μm. We deliberately varied the pulse duration to get a large number of intermediate states; a pristine capacitor was used for each state. The polarization at zero field was obtained from Sawyer-Tower measurements. Afterwards, the Au top electrode was removed and the mean PFM phase was obtained from the histogram. The light blue dots in Fig. 3 show the polarization as a function of the mean value of the PFM phase. The polarization monotonously decreases with increasing mean value of the PFM phase. The data can be described by a linear relation. Extrapolating to PFM phase values of 0° and 180°, we obtain a polarization of ± 9 μC/cm^2. This corresponds to the value for the saturated polarization, when all dipoles are aligned in

parallel [111]. The difference between the extrapolated saturated polarization and the experimentally obtained remanent polarization is due to back-switching [109] [110] and the presence of defects with misaligned polarity [29] [108].

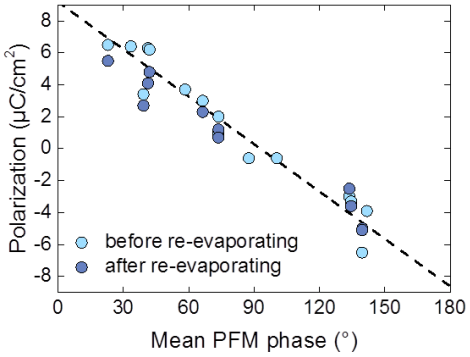

FIG. 5.2.3. The electrically measured macroscopic polarization as a function of the mean value of the out-of-plane phase measured by PFM. The ferroelectric capacitors were programmed in various intermediate states, whose polarization was measured with a Sawyer-Tower setup. Then the top electrodes were etched away and PFM measurements were conducted on the exposed P(VDF-TrFE) thin film. The data are presented by the light blue circles. The PFM measurements were repeated after storing the films in ambient atmosphere for a week and subsequently new Au top electrodes were evaporated at the same spots. The macroscopic polarization was re-measured. The data are presented by the dark blue circles. The dashed line is a linear fit to the measured data.

We note again that the PFM phase only depends on the component normal to the surface. The phase measurement cannot distinguish between domains that are perfectly perpendicular, and off-axis domains that exhibit an angle with respect to the surface normal. The phase response is in both cases the same. For a binary system, in which the domains can only be oriented “up” or “down”, the polarization depends by definition linearly on the mean PFM phase. P(VDF-TrFE) is not a perfect binary system, but a semi-crystalline polymer. The fact that the polarization still depends linearly on the PFM phase implies that the off-axis domains for “up” and “down” orientation apparently cancel each other out statistically.

Even without the top electrode, the domains of the P(VDF-TrFE) film are stable over time in ambient conditions. We performed PFM measurements again after the samples had been stored in ambient conditions for a week. We did not find any change in the mean value of the PFM phase. The morphology of the domains remained unchanged. We then re-evaporated Au on the samples as the new top electrodes. The new top electrodes can easily be aligned as the capacitor arrays have a cross-bar layout. After re-evaporation, we measured the remanent polarization with the Sawyer-Tower setup. As shown by the dark blue circles in Fig. 5.2.3, no change in the macroscopic polarization was observed, confirming that the exposed domains are stable in ambient conditions.

The remarkable retention of polarization, even in the absence of a top electrode, is further confirmed by measuring the remanent polarization of free-standing 30 μm thick P(VDF-TrFE) foils. In order to

polarize the foil, we used mechanically removable brass electrodes. The polarization states were retained for weeks. This stability is surprising, as the depolarization field, which is as high as 1 GV/m for a fully polarized P(VDF-TrFE) layer, is, in a free-standing film, not compensated for by counter charges from an electrode. Several secondary compensation mechanisms have been proposed, such as screening by ionic species as a result of dissociative water adsorption [44] [112], electrochemical equilibria by external oxygen partial pressure [113] and interfacial charges by oxygen vacancies [114].

We note, however, that net charges, *e.g*. ions, *alone* cannot be the reason for the stabilization in our case. Presence of ions would lead to a substantial built-in field upon re-evaporation of the top electrode, resulting in a pronounced horizontal shift when measuring the *D-E* hysteresis loop (imprint). When measuring the *D-E* hysteresis loop we should then see a huge horizontal shift. However, the experimentally observed shift was less than 10 MV/m, which corresponds to a surface density of net charges less than 0.01 μC/cm^2, by far lower than the necessary surface charge density to counter balance the depolarization field.

This contradiction can be resolved if we assume that the adsorbed species form an electrical double layer. Since a double layer is electrically neutral, its presence does not cause a built-in field. We note that the adsorption of neutral polar molecules such as H_2O and their role in screening mechanism have been suggested via density functional calculations [115]; the adsorption of CH_3OH and CO_2 on $BaTiO_3$ and PZT has been experimental verified by temperature-programmed desorption and scanning surface potential microscopy measurements [116]. In summary, although the detailed mechanism for domain stability remains elusive, Fig. 5.2.3 unambiguously demonstrates that the domains and the polarization are not affected by removal of the top electrode.

5.3 Domain morphology during polarization switching

The global excitation and local probing method can be used to study domain morphology as a function of macroscopic polarization. As an example, here, we compare the domain morphology of two different capacitors with zero polarization. One capacitor was electrically depoled by applying an alternating electric field with gradually decreasing amplitude [83]. The other capacitor was thermally depoled by annealing above the Curie temperature.

Figs. 5.3.1 (a) and 5.3.1 (b) show the PFM topography and phase images for the electrically depoled film after etching the Au top electrode. The morphology of the ferroelectric domains does not completely overlap with the film topography: a single domain can cross over different P(VDF-TrFE) grains and within a single grain there can exist multiple domains. Due to stochastic nucleation and anisotropic growth “up” and “down” domains are randomly distributed [117] [118]. This is in direct contrast to ordered ferroelectric materials, in which the domains are ordered stripes predetermined by the Kittel-Mitsui-Furuichi law [119] [120].

The phase image is quantified in the histogram shown in Fig. 5.3.1 (c). A bimodal distribution is observed with peak values around 20° and 140°. The dashed line shows the mean value by integration.

It is about 90°, corresponding to zero macroscopic polarization, in agreement to the data presented in Fig. 5.2.3. On average, the area of "up" and "down" domains is the same.

The PFM topography and phase images for the thermally depoled film are presented in Figs. 5.3.1 (d) and 5.3.1 (e), respectively. The topography is the same as for the electrically depoled film, which proves that the thermal depoling process does not affect the film's morphology. The PFM phase image, however, is completely different. The thermally depoled film shows a homogeneous PFM phase, in which single domains cannot be distinguished. This is reflected in the extracted histogram of Fig. 5.3.1 (f), which exhibits one single peak at 90°. Apparently, the domains are smaller than the resolution a PFM tip can achieve; each pixel corresponds to the average of several "up" and "down" domains and, therefore, the phase yields 90°. Although the two capacitors exhibit the same macroscopic polarization, their domain morphology is completely different.

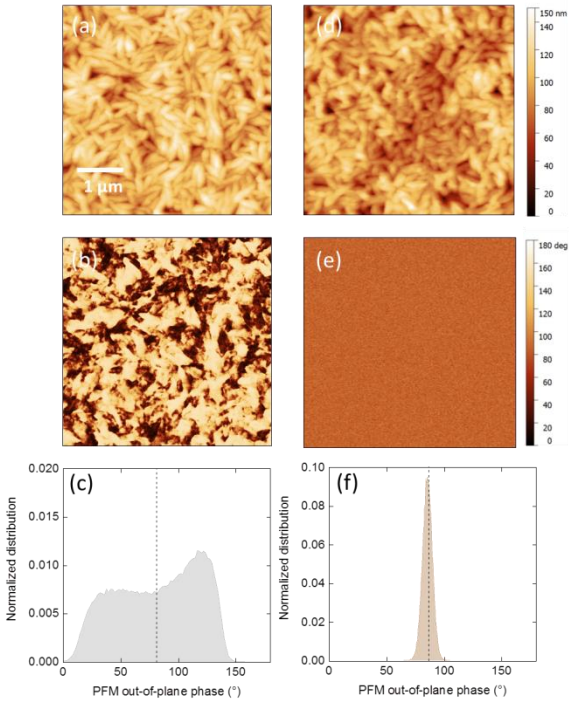

FIG. 5.3.1. Domains of electrically and thermally depoled P(VDF-TrFE) capacitors. Images were obtained after chemically removing the top electrodes. (a) Topography of the exposed P(VDF-TrFE) thin film in the electrically depoled capacitor. (b) The corresponding PFM phase image. (c) Histogram of the PFM phase values. The dashed line indicates the mean value obtained by integration. (d) Topography of the exposed P(VDF-TrFE) thin film in the thermally depoled capacitor. (e) The corresponding PFM phase image. (f) Histogram of the PFM phase values.

5.4 Summary

In conclusion, we have demonstrated a global excitation and local probing method for the investigation of ferroelectric domains with high resolution. A ferroelectric P(VDF-TrFE) capacitor is poled to a set polarization state in a Sawyer-Tower setup. Subsequently, the top electrode is chemically removed, without affecting the surface of the ferroelectric material. Afterwards the ferroelectric domains are locally probed by PFM. We show a linear relation between the PFM phase and the macroscopic polarization. The global excitation and local probing method can be used to study domain morphology as a function of macroscopic polarization. As an example, we have shown that the domain morphology between thermally and electrically depoled ferroelectric thin capacitors is completely different, although the macroscopic polarization is the same.

Chapter 6 Depolarization field and domain-wall depinning mechanism

Depolarization in ferroelectric materials, an important data-loss process in memories, has been studied in pioneering works since the 1970s, albeit under quasi-static conditions. To study the dynamics of depolarization one resorts to the empirical Merz law, which gives the polarization switching time as a function of electric field, normalized to the so-called activation field. The Merz law has been used for decades; its origin as domain-wall depinning has recently been corroborated by first-principles-based molecular dynamics simulations. Here we experimentally investigate domain-wall depinning by measuring the dynamics of depolarization in ferroelectric thin films. We find that the boundary between thermodynamically stable and depolarizing regimes can be described by a single constant, $P_{sat}/\varepsilon_0\varepsilon_{ferro}E_c$. Among different multidomain ferroelectric materials the values of coercive field, dielectric constant and polarization vary by orders of magnitude; the value for $P_{sat}/\varepsilon_0\varepsilon_{ferro}E_c$ however is comparable, implying a relation between activation-, depolarization- and intrinsic coercive field. We propose that the causality naturally holds, when domain-wall depinning originates from collective switching of polarized regions near pinning sites.

6.1 Depolarization field

The existence of a depolarization field in polarized ferroelectric materials was first experimentally demonstrated in the 1970s [121] [122]. In the pioneering work of Wurfel *et al*. [122], a triglycine sulfate ferroelectric film was sandwiched between a metal electrode and a *p*-type silicon counter electrode. The ferroelectric material could be poled when the Si-semiconductor was strongly illuminated. The photo-generated charge carriers then could stabilize the ferroelectric polarization. However, after switching off the light, only half of the polarization loop was observed, since only accumulation of majority carriers can provide sufficient compensation. Without compensating charges the ferroelectric material cannot maintain the remanent polarization due to the presence of a high depolarization field.

A polarized ferroelectric material exhibits a depolarization field given by [81]:

$$E_{dep} = -\frac{P}{\varepsilon_0 \varepsilon_{ferro}} \tag{6.1.1}$$

where P is the ferroelectric polarization, ε_0 and ε_{ferro} are the vacuum permittivity and static dielectric constant, respectively. As a typical example, for the ferroelectric random copolymer poly(vinylidenefluoride-trifluoroethylene) [P(VDF-TrFE)], the depolarization field can be estimated as 1 GV/m with a saturated polarization of 7 μC/cm^2 and a static dielectric constant of 10 taken. This field is an order of magnitude higher than the coercive field, E_c, of about 50 MV/m. The polarization is expected to be instable, but can be stabilized in a ferroelectric capacitor as the metallic electrodes provide free charges that fully compensate the depolarization field, yielding a zero internal electric field inside the ferroelectric material.

When the depolarization field is not fully compensated, the remanent polarization is suppressed. Incomplete compensation practically can for instance be due to the occurrence of a “dead layer” between the electrodes and the ferroelectric material [123] [124], or due to the finite screening length in metallic electrodes [121] [125] [126]. Another example is the ferroelectric field-effect transistor [127]; the semiconducting layer causes an uncompensated depolarization field that limits data retention.

The “dead layer” and finite screening length are typically modeled in an equivalent circuit comprising a linear capacitor in series with the ferroelectric capacitor [123] [124] [126]. This circuit yields a relation between depolarization field and suppressed remanent polarization, and has been verified by quasi-static hysteresis loop measurements [81]. Yet the dynamics of the polarization evolving from the fully saturated to the suppressed state have not been investigated.

Here, we study the depolarization dynamics. We use a ferroelectric capacitor in series with a linear capacitor to tune the compensation of the depolarization field. We used two classic ferroelectric materials, *viz.* P(VDF-TrFE) and Pb(Zr,Ti)O_3 (PZT). After applying a voltage pulse the electric displacement is measured as a function of time, from which the internal electric field is derived. The transients are quantitatively described by a generalized Kolmogorov-Avrami-Ishibashi (KAI) formalism, and feature a negative differential capacitance during the whole depolarization process. A depolarization diagram, constructed from the normalized displacement as a function of the ratio of the

capacitances, shows depolarizing and thermodynamically stable regimes. The boundary between these regimes defines a unique constant, comprising coercive field, dielectric constant and saturated polarization, $P_{sat}/\varepsilon_0\varepsilon_{ferro}E_c$, of about 16. This experimentally derived constant is identical for PZT and P(VDF-TrFE). Remarkably, the values of $P_{sat}/\varepsilon_0\varepsilon_{ferro}E_c$ for different ferroelectric materials, in which switching is mediated by nucleation and growth of domains, are comparable, although the values of coercive field, dielectric constant and polarization vary by orders of magnitude; the constant is therefore expected to be universal for multidomain ferroelectric materials. It is further deduced that the depolarization field is comparable to the activation field for domain-wall depinning in disordered ferroelectric systems, $E_{dep} \sim E_{act}$; the correlation with intrinsic switching, *i.e.* collective rotation of dipoles, is discussed. We argue that the relation extracted between the depolarization field and activation field implies that the domain-wall depinning originates from collective switching of polarized regions near pinning sites in ferroelectric thin films.

6.2 Suppression of the remanent polarization

The displacement versus applied voltage, D-V_{app}, hysteresis loops of ferroelectric-only capacitors comprising PZT or P(VDF-TrFE) are presented in Fig. 6.2.1 (a) and 6.2.1 (d), respectively. Values extracted for the coercive field amounted to 1 MV/m and 50 MV/m, and values extracted for the remanent polarization amounted to 38 μC/cm^2 and 7 μC/cm^2, all in good agreement with literature [128] [26].

The hysteresis loops of a ferroelectric capacitor, C_{ferro}, in series with different linear capacitors, C_{ser}, are presented in Fig. 6.2.1 (b) and 6.2.1 (e) for PZT and P(VDF-TrFE) respectively. At high bias all loops are saturated with the same value for the displacement as the ferroelectric-only capacitor. For higher ratios of C_{ferro}/C_{ser}, a higher applied voltage is needed to fully polarize the ferroelectric capacitor. All loops have an identical apparent coercive voltage, independent of the ratio C_{ferro}/C_{ser}, as at zero displacement there are no net free charges in the electrodes and hence the equivalent circuit is a ferroelectric-only capacitor.

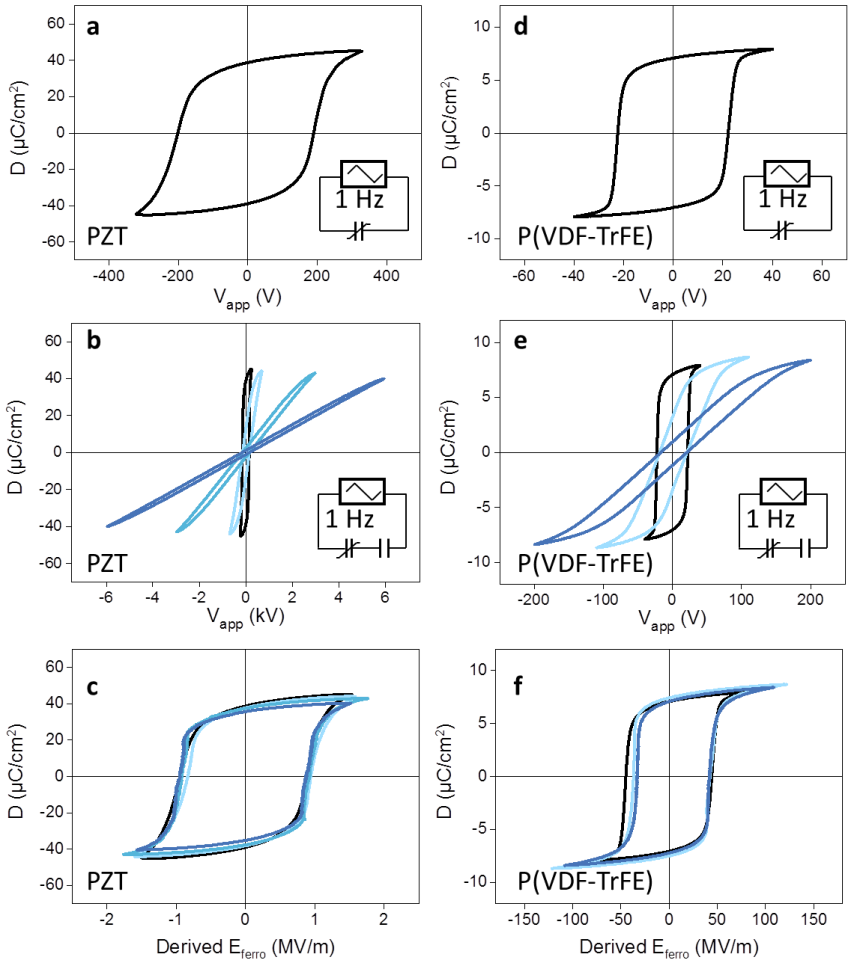

FIG. 6.2.1 Quasi-static hysteresis loops. (a,d) Electric displacement *vs.* applied voltage measured quasi-statically at 1 Hz on a PZT507 and P(VDF-TrFE) ferroelectric-only capacitor, respectively. The insets schematically show the measurement circuit. (b,e) Electric displacement *vs.* applied voltage measured at 1 Hz on a PZT507 and P(VDF-TrFE) ferroelectric capacitor in series with different linear capacitors. The ratio of capacitances varies from 0 (black line), to 3 (blue line) for PZT507 and to 0.3 (blue line) for P(VDF-TrFE). (c,f) Reconstructed D-E_{ferro} loops.

To obtain the intrinsic properties of the ferroelectric material, we reconstructed the hysteresis loops as a function of the electric field inside the ferroelectric material, E_{ferro}, which is derived in Section 3.3 as:

$$E_{ferro} = \frac{V_{app}}{d} - \frac{D}{\varepsilon_0 \varepsilon_{ferro}} \times \frac{C_{ferro}}{C_{ser}} \tag{6.2.1}$$

where V_{app} is the applied voltage and d is the thickness of the ferroelectric layer. Note that due to the incomplete compensation at $V_{app} = 0$ the net field E_{ferro} gives rise to a voltage drop over the ferroelectric capacitor that is equal, but with opposite sign, to the voltage drop over the serial

capacitor. The D-E_{ferro} loops derived from Eq. (6.2.1) are presented in Fig. 6.2.1 (c) for PZT and Fig. 6.2.1 (f) for P(VDF-TrFE). The reconstructed loops for various C_{ferro}/C_{ser} ratios all collapse and are identical to that of the ferroelectric-only capacitor. We note, however, that Eq. (6.2.1) applies only when the leakage current through the serial capacitance is negligible, which is the case in our work. An artificial interfacial layer [129] or fatigue-induced delamination [102] can lead to resistive interfacial layers with "threshold conduction"; there the measured D-V_{app} loops behave broadened instead of tilted, and the serial-capacitor model is no longer valid [130].

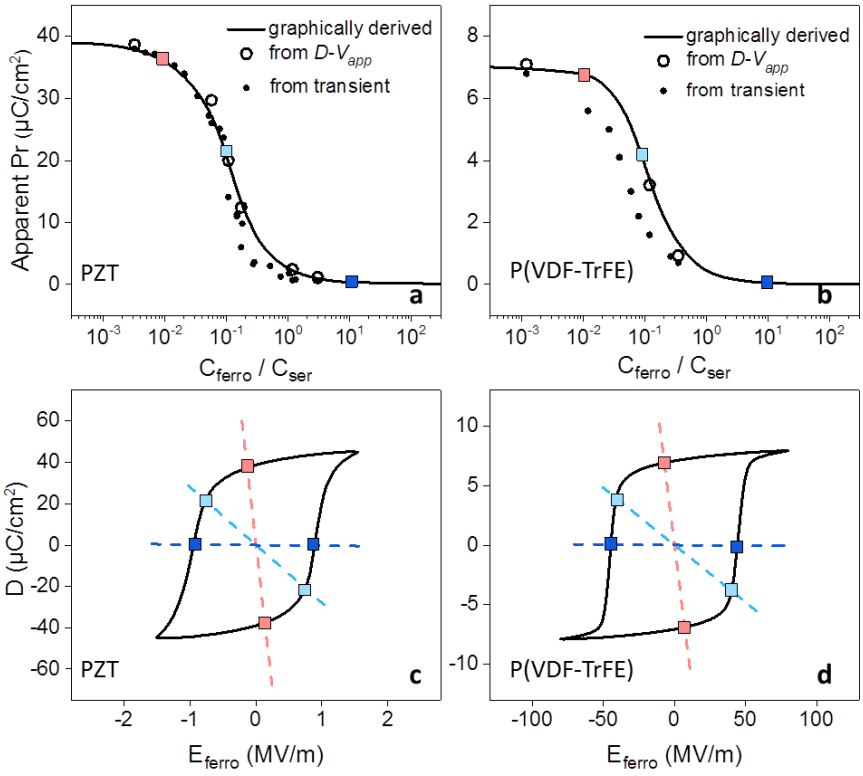

FIG. 6.2.2 Suppression of polarization. Apparent remanent polarization, *i.e.* the displacement at zero applied voltage, as a function of the ratio of capacitances, C_{ferro}/C_{ser}, for (a) PZT and (b) P(VDF-TrFE) in serial circuits. The hollow symbols are extracted from Figs. 1b,e. Black dots are obtained from transient measurements. Solid lines present graphically extracted values. (c,d) Graphical derivation of the apparent remanent polarization from the D-E_{ferro} loop of ferroelectric-only capacitors of PZT and P(VDF-TrFE), respectively. As an example, the derived values for C_{ferro}/C_{ser} of 0.01, 0.1 and 10 are marked with coloured squares.

The apparent remanent polarization, *i.e.* the displacement at zero applied bias, is extracted from the hysteresis loops of Figs. 6.2.1 (b), (e) and presented by the hollow symbols as a function of the ratio C_{ferro}/C_{ser} in Figs. 6.2.2 (a), (b).

The value for the apparent remanent polarization can also be graphically determined from the hysteresis D-E_{ferro} loop of the ferroelectric-only capacitor [131]. In a serial circuit the internal electric field in the ferroelectric material, at zero applied bias, is given by Eq. (6.2.1) as E_{ferro} =

$-D\times(C_{ferro}/C_{ser})/(\varepsilon_0\varepsilon_{ferro})$, and presented as straight lines in Figs. 6.2.2 (c), (d) for three different ratios of capacitances. Each cross point is by definition equal to the apparent remanent polarization. The values derived are presented as the coloured squares. The solid lines in Figs. 6.2.2 (a), (b) are graphically extracted as a function of the ratio C_{ferro}/C_{ser}. A good agreement with the apparent remanent polarization extracted from the quasi-static D-V_{app} hysteresis loops, *c.f.* Fig. 6.2.1, is obtained for both PZT and P(VDF-TrFE), which legitimates our derivation below of the internal field from the displacement using Eq. (6.2.1). .

6.3 Dynamics of depolarization

The suppression of polarization was hitherto investigated by measuring quasi-static hysteresis loops, where the electric field changes gradually. It might be, however, that the final polarization state is different when a high applied electric field is abruptly switched off. The polarization in this case is initially still saturated leading to a huge depolarization field that is no longer fully compensated. The ferroelectric material is expected to depolarize. However, the final polarization state is not *a priori* known; one might even expect macroscopic polarization reversal as an overshoot effect.

Here we investigate the depolarization dynamics. We applied a voltage pulse, high enough to fully polarize the ferroelectric capacitor. Then the applied voltage abruptly dropped to 0 V, and we recorded the transient of the electric displacement, $D(t)$. A schematic representation of the applied pulse and the measured response is given in the inset of Fig. 6.3.1 (a). At the end of the applied pulse there is a fast discharge of the induced polarization. Afterwards, the ferroelectric polarization dominates the transient. As a typical example, a set of transients of a PZT capacitor in series with three different serial capacitors are presented in Fig. 6.3.1 (a). The electric displacement drastically decreases within the first 100 ms. Subsequently, the displacement only slightly decreases with time and stabilizes after a few seconds. When the displacement is stabilized we disconnect the serial capacitor and measure the first two D-V_{ferro} hysteresis loops of the ferroelectric-only capacitor, presented in Fig. 6.3.1 (b). The starting point of the first loop agrees with the ending point of the transient measurement yielding the retained polarization. The second loop was measured as a reference and found to coincide with the first loop, excluding experimental artefacts. The retained polarization is presented in Fig. 6.2.2 (a), (b) as a function of the ratio C_{ferro}/C_{ser}. The values measured for PZT are similar to those obtained from the quasi-static measurements; for P(VDF-TrFE) the values slightly deviate. However, no overshoot is observed for either ferroelectric material. We therefore conclude that the final polarization state in the dynamic depolarization measurements is identical to the suppressed polarization state reached quasi-statically. The transients for P(VDF-TrFE) are presented in Fig. 6.3.1 (c). The solid lines are depolarization transients calculated with the Kolmogorov-Avrami-Ishibashi (KAI) formalism [30] [31] [32] [29] [74], adapted to a time-dependent electric field [118] and Merz law [86] [132]. The good agreement implies that depolarization is due to domain switching without macroscopic polarization reversal.

From the measured transients of displacement, D-t, of Fig. 6.3.1 (c) the field inside the ferroelectric material, E_{ferro}, is calculated using Eq. (6.2.1). The time-dependent internal electric field is presented

in Fig. 6.3.1 (d) for the two different capacitance ratios. Solid lines are iteratively calculated using the KAI formalism. Fig. 6.3.1 (d) shows that the final internal field is about equal to the coercive field, as will be explained further below.

During depolarization, both the internal electric field and the displacement are decreasing with time. However, as their signs are opposite, as shown in Figs. 6.3.1 (c), (d), the depolarization transients feature a negative differential capacitance. An *NDC* as a transient phenomenon has been reported in ferroelectric capacitors during polarization reversal [133] [134] [135]. Here, the *NDC* is the derivative of the amount of free charges at the ferroelectric capacitor, Q_{ferro}, with internal voltage, V_{ferro}, and the absolute value is by definition equal to the serial capacitance:

$$NDC = \frac{\mathrm{d}Q_{ferro}}{\mathrm{d}V_{ferro}} = \frac{A}{d} \times \frac{\mathrm{d}D}{\mathrm{d}E_{ferro}} = -C_{ser} \tag{6.3.1}$$

where we used Eq. (6.2.1) for the relation between D and E_{ferro} at zero applied external bias. The *NDC* is constant during the whole depolarization process, unlike in the case of bipolar switching [133].

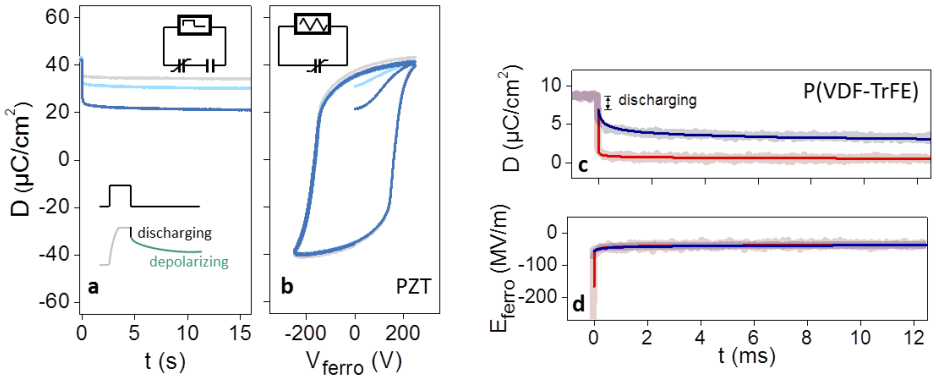

FIG. 6.3.1 Depolarization dynamics. (a) Transients of the electric displacement of a PZT507 ferroelectric capacitor (C_{ferro} = 14 nF) with various serial capacitors. The circuit and transient measurement are schematically described in the inset. The transients for C_{ser} as 6 μF, 330 nF and 110 nF are presented with grey, light blue and blue lines respectively. (b) Reading the retained polarization by measuring the ferroelectric-only capacitor after depolarization. (c,d) Displacement and internal field as a function of time. The dynamics of the displacement, after a fast discharge of the induced polarization shown by the double arrow, are given by the solid lines, as obtained by numerical calculation. The curves correspond to the serial capacitances of 4.4 nF (blue line) and 890 pF (red line). C_{ferro} of P(VDF-TrFE) here is 260 pF.

To measure the depolarization transient, we apply a voltage pulse, high enough to fully polarize the ferroelectric capacitor. The initial value of displacement is taken after the fast discharge of the induced polarization, as shown in the inset of Fig. 6.3.1 (a). The initial and final internal fields are calculated from the corresponding displacement using Eq. (6.2.1) and presented in Fig. 6.3.2 as a function of C_{ferro}/C_{ser}. When the initial internal field is much lower than the coercive field, the initial and final internal fields are identical; there is no depolarization. However, when the initial internal field is much

higher than the coercive field, the ferroelectric material depolarizes until the final internal field is stabilized at the coercive field, regardless of the ratio C_{ferro}/C_{ser}.

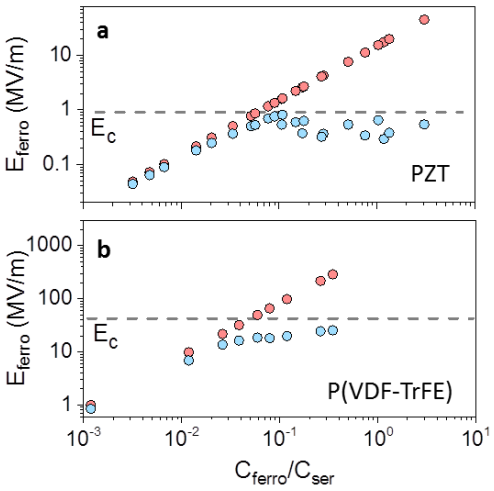

FIG. 6.3.2 Internal electric field. (a,b) Internal electric field as a function of the ratio of capacitances for PZT and P(VDF-TrFE), respectively. The red circles represent the initial electric field, directly after the applied voltage drops to zero and the induced polarization is discharged. The blue circles represent the retained values after depolarization. The dashed lines represent the coercive field.

Such a difference from a ferroelectric-only capacitor can be understood as follows. The depolarization field is always fully compensated by countercharges in the electrodes; at zero applied bias the internal field is always zero. However, when a serial capacitor is connected, incomplete compensation results in a finite internal field, as shown by Eq. (6.2.1). When this internal field is lower than the coercive field, the system is thermodynamically stable; there is no switching and no depolarization. If the initial internal field is higher than the coercive field, then domains will switch, leading to depolarization. The internal field decreases concomitantly with polarization. When the internal field becomes lower than the coercive field, a stable state is obtained. In the depolarized ferroelectric material an internal electric field as high as the coercive field remains. Consequently, the ratio of capacitances can also be used to tune the non-linear optoelectronic properties of ferroelectric materials.

6.4 Depolarization diagram

Figs. 6.3.1 (c), (d) imply a relation between the coercive field, the displacement and the ratio of capacitances, which can be elucidated by plotting the displacement as a function of $C_{ferro}/C_{ser.}$ In order to compare different ferroelectric materials, we normalize the displacement by the saturated polarization, P_{sat}, which is the ferroelectric polarization when all the dipoles are aligned. The

depolarization measurements are summarized in the depolarization diagram presented in Fig. 6.4.1. For a given ratio of capacitances we apply a voltage pulse to set a polarized state and then remove the bias. Each point in the diagram represents a set displacement as a function of the ratio of capacitances.

The diagram shows depolarizing and thermodynamically stable regimes. The stability boundary separating the two regimes is obtained when the internal field is equal to the coercive field. The boundary, presented by the grey line, is derived from Eq. (6.2.1) and reads:

$$D/P_{sat} = \frac{\varepsilon_0 \varepsilon_{ferro} E_c / P_{sat}}{C_{ferro} / C_{ser}} \tag{6.4.1}$$

The light-grey area of Fig. 6.4.1 represents states in which the set displacement is smaller than both the boundary value and the saturated polarization. These are intermediate polarization states, which are reported to be thermodynamically stable [83]. The internal field is zero when the ferroelectric capacitance is much smaller than the serial capacitance. For a given displacement the internal field increases with C_{ferro}/C_{ser} and reaches the coercive field at the boundary.

The dark grey area represents fully saturated states reached at very high applied bias. The displacement is equal to the saturated ferroelectric polarization plus the linear displacement, P_{sat} + $\varepsilon_0\varepsilon_{ferro}E_{ferro}$. Upon removing the applied bias the induced polarization is discharged and the displacement reduces to the saturated polarization, P_{sat}. There is no depolarization and the remanent polarization is equal to the saturated polarization.

When the set displacement is higher than the boundary value, *i.e.* in the white region of Fig. 6.4.1, the ferroelectric material depolarizes. As an example, we replotted the measurements of Fig. 6.3.1 (c). The green circle denotes the set state and the arrow indicates the measured depolarization. After depolarization the remanent polarization in the final state is equal to the boundary value of the displacement at that ratio of capacitances. This depolarization process is corroborated by replotting the transients of Fig. 6.3.1 (c) in the depolarization diagram. The final internal field is equal to the coercive field. The depolarization transient features an *NDC*. The absolute value of the *NDC* is equal to the serial capacitance during the whole depolarization process.

We replotted the retained displacement for both P(VDF-TrFE) and PZT, *c.f.* Fig. 6.2.2, in the depolarization diagram. The data points for both materials overlap and are identically described by the stability boundary, Eq. (6.4.1). This means that for both materials the normalized displacement D/P_{sat} is a unique linear function of $(C_{ferro}/C_{ser})^{-1}$, with the same proportionality constant, $P_{sat}/\varepsilon_0\varepsilon_{ferro}E_c$, of about 16. We calculated this constant for other ferroelectric materials. The derived values are presented in Table 6.4.1. Among different ferroelectric materials the values of coercive field and dielectric constant vary by orders of magnitude. Remarkably, for all ferroelectric materials a comparable value for $P_{sat}/\varepsilon_0\varepsilon_{ferro}E_c$ is obtained, suggesting that this constant is universal.

TABLE 6.4.1 Values of $P_{sat}/\varepsilon_0\varepsilon_{ferro}E_c$ extracted for ferroelectric materials.

Ferroelectric material	Code	P_{sat} * ($\mu C/cm^2$)	E_c (MV/m)	ε_{ferro}	$P_{sat}/\varepsilon_0\varepsilon_{ferro}E_c$	Reference
P(VDF-TrFE) **		7	50	10	**16**	
β PVDF		7	60	10	**13**	
δ PVDF		10	115	9	**11**	[136]
PZT	PZT507	40	1.0	3500	**14**	
"	PZT4	35	1.3	1260	**27**	
$BaTiO_3$	SPS-nano 0.6µm	24	0.35	5250	**16**	[137]
"	Sample A 1.3µm	20	0.36	5000	**14**	[138]
$SrBi_2Ta_2O_9$		15	3.0	400	**16**	[139]
Nylon-11		6	60	5	**25**	[140]
trialkylbenzene-1,3,5-tricarboxamide	BTA-C10 100°C 1Hz	4	30	10	**17**	[141]
"	BTA-C18 100°C 1Hz	2.5	20	10	**16**	[141]
$Bi_{0.5}Na_{0.5}TiO_3$-$Bi_{0.5}K_{0.5}TiO_3$	BNKT70	37	3.2	1000	**14**	[142]
"	BNKT94	37	7	400	**17**	[142]
$Sr_{0.15}(Na_{0.5}Bi_{0.5})_{0.85}TiO_3$	25°C	27	2	1000	**17**	[143]

*The saturated polarization, P_{sat}, is taken from the maximum polarization of the ferroelectric-only capacitor.
**Presented values are obtained at ambient temperature. In Section 6.6 we show that the value of $P_{sat}/\varepsilon_0\varepsilon_{ferro}E_c$ remains constant between 213 K and 333 K.

The common value found for $P_{sat}/\varepsilon_0\varepsilon_{ferro}E_c$ relates the depolarization field to the activation field for polarization switching. The switching time in ferroelectric materials follows the empirical Merz law [86] [132]:

$$t_0 = t_\infty \exp\left(\frac{E_{act}}{E}\right) \tag{6.4.2}$$

where E is the applied electric field and E_{act} is the activation field [79], describing the onset of domain wall motion [38] [96]. The activation field is typically one order of magnitude higher than the coercive field [144], and hence the coercive field times the proportionality constant of 16 is approximately equal to the activation field [118].

The proportionality constant can be derived from the phenomenological model of Miller and Weinreich, originally derived for 180° domain-wall motion in $BaTiO_3$ [37]. The activation field, E_{act}, is approximated as [74]:

$$E_{act} = \frac{c\sigma_{dw}^2}{P_{sat} k_B T} \tag{6.4.3}$$

where c is the width of the domain wall, σ_{dw} is the domain-wall energy; k_B is the Boltzmann constant, and T is the absolute temperature. Each domain grows from a critical nucleus with an internal energy, ΔU^*, approximated as:

$$\Delta U^* = \frac{c\sigma_{dw}^2}{P_{sat} E_c} = k_B T \frac{E_{act}}{E_c} \tag{6.4.4}$$

The proportionality constant of about 16 we derived corresponds, within this model, to $\Delta U^*/ k_B T$. A range of values for ΔU^* has been reported [74], *e.g.* 29 $k_B T$ for thin films P(VDF-TrFE), 15 $k_B T$ for PVDF Langmuir Blodgett films, 40 $k_B T$ for $BaTiO_3$ and 10 $k_B T$ for PZT, leading to a range of the proportionality constant of 10 to 40.

On the other hand, the term $P_{sat}/\varepsilon_0\varepsilon_{ferro}$ is the depolarization field in fully polarized ferroelectric materials. The unique proportionality constant then implies that the activation field for domain-wall motion is about equal to the depolarization field:

$$E_{act} \sim E_{dep} \tag{6.4.5}$$

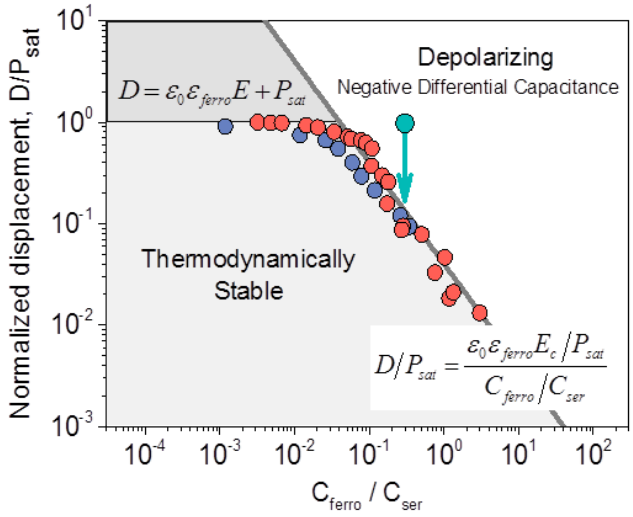

FIG. 6.4.1 Depolarization diagram of ferroelectric materials. The normalized displacement is presented as a function of the ratio of capacitances. The diagram shows the stability for any set state at zero applied bias. The boundary between thermodynamically-stable states and depolarizing states is the grey line calculated with the

inset formula. The blue and red symbols represent the normalized, retained displacement using P(VDF-TrFE) and PZT capacitors connected with serial capacitors, respectively. The green arrow is reproduced from Fig. 6.3.1 (c). The green circle denotes the set state and the arrow indicates the measured depolarization.

6.5 Origin of activation field

Merz law, *c.f.* Eq. (6.4.2), is a special case of domain-wall motion in generic creep systems, describing propagation of elastic objects driven by an external force in the presence of a pinning potential [38], such as domains in ferroelectric [38] and magnetic materials [145], or vortices in type-II superconductors [146]. At zero temperature, domain walls are pinned when the external driving force, f, is below a certain threshold depinning force, f_d. At finite temperature, when $f < f_d$, domain-wall motion is thermally activated and the velocity, v, follows the creep formula [38]:

$$v = \exp\left[-\frac{U}{k_B T}\left(\frac{f_d}{f} \right)^{\mu} \right] \tag{6.5.1}$$

where U is a depinning energy barrier and μ is an exponent related to the type of disorder. For polycrystalline ferroelectric materials μ is reported to be about unity [38] [79] [96] [74] [118] and the activation field can be regarded as a depinning field. The experimentally found relation between depolarization field and activation field implies that depinning is due to overcoming the depolarization field.

Pinning sites in ferroelectric materials are point defects with a fixed polarity [38] [96]. Dipoles in the vicinity tend to align in parallel to the polarity of the pinning site. We propose that depinning of the domain wall requires collective switching of these polarized regions. Their internal electric field is the depolarization field, which has to be overcome in order to move the domain walls. Hence the depolarization field is the onset of domain-wall creep and hence similar to the activation field, $E_{dep} \sim E_{act}$. Interestingly, by expanding and keeping the leading term of the Landau-Devonshire free energy, one finds that the depolarization field is approximately equal to the thermodynamic coercive field [29], or often termed as intrinsic coercive field, $E_{dep} \sim E_{int,c}$. Consequently, the depolarization- and activation field should be of the same order of magnitude as the intrinsic coercive field, $E_{dep} \sim E_{act} \sim E_{int,c}$. This relation is supported by the experimentally determined values for the intrinsic coercive field for ultrathin films of $PbTiO_3$ [147] and Langmuir-Blodgett films of P(VDF-TrFE) [60].

6.6 Temperature dependence

To investigate the temperature dependence of $P_{sat}/\varepsilon_0\varepsilon_{ferro}E_c$, we have measured the saturated polarization, dielectric function and the coercive field of P(VDF-TrFE) ferroelectric-only capacitors at temperatures ranging from 213 K to 333 K.

The real part of the dielectric constant is presented as a function of frequency for various temperatures in Fig. 6.6.1 (a). The dielectric loss is measured to be 2 % or less. The dielectric constant is almost frequency-independent below 10 kHz and slightly decreases at higher frequency. We take for the value of the static dielectric constant, ε_{ferro}, the dielectric constant at 1 kHz. Fig. 6.6.1 (a) shows that the value of the static dielectric constant increases with temperature from 6 at 213 K to 11 at 333 K.

The temperature dependence of the coercive field, E_c, is presented in Fig. 6.6.1 (b). The values of E_c were extracted from quasi-static *D-E* hysteresis loops, measured in a Sawyer-Tower configuration at 100 Hz. As typical examples, hysteresis loops measured at three temperatures, *viz.* 213 K, 253 K and 333 K, are shown in the inset. The value of the coercive field monotonously decreases with increasing temperature from 115 MV/m at 213 K to 40 MV/m at 333 K. From the hysteresis loops we extracted the value of the saturated polarization, P_{sat}, which slightly decreases from 8.8 μC/cm^2 at 213 K to 6.6 μC/cm^2 at 333 K. We note that the hysteresis loops indicate that the remanent polarization is almost equal to the saturated polarization; the difference in displacement between high bias and zero bias is dominated by the induced polarization, $\sim\varepsilon_0\varepsilon_{ferro}E$.

We calculated the value of $P_{sat}/\varepsilon_0\varepsilon_{ferro}E_c$ using the extracted values of saturated polarization, static dielectric constant, and coercive field. As shown in Fig. 6.6.1 (c) the value is about 16 and independent of temperature between 213 K and 333 K. The constant value implies that at all temperatures the depolarization field, E_{dep}, is equal to the activation field, E_{act}. The calculated depolarization field is presented as a function of temperature in Fig. 6.6.1 (d), together with the activation field independently extracted from polarization switching measurement [118]. For all temperatures a perfect agreement is obtained, demonstrating that the relation $E_{dep} \sim E_{act}$ holds for P(VDF-TrFE) within a wide range of temperatures.

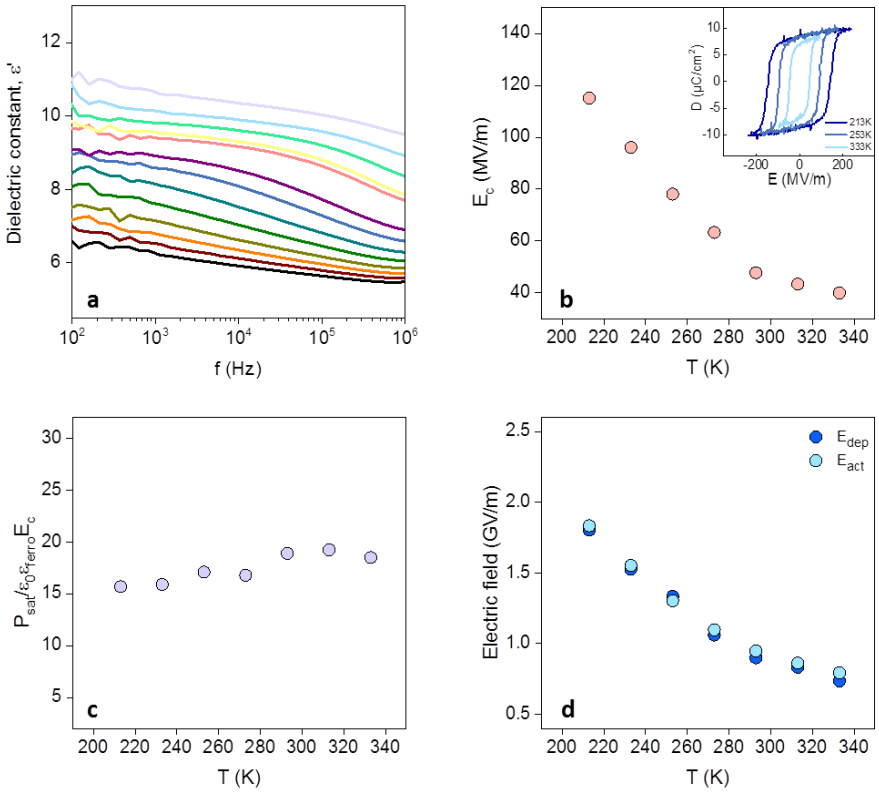

FIG. 6.6.1 Temperature dependence of P(VDF-TrFE) ferroelectric-only capacitors. (a) The real part of the dielectric constant as a function of frequency at various temperatures between 213 K (black line) to 333 K (light purple line). (b) The coercive field extracted from quasi-statically measured *D-E* hysteresis loops as a function of temperature. Hysteresis loops were measured at 100 Hz. Typical examples at three temperatures are shown in the inset. (c) Calculated value of $P_{sat}/\varepsilon_0\varepsilon_{ferro}E_c$ as a function of temperature. (d) The calculated depolarization field and the independently extracted activation field as a function of the temperature. E_{dep} is calculated using the measured values of ε_{ferro} and P_{sat}. E_{act} is extracted from polarization switching measurements [118].

6.7 Summary

In conclusion, we have investigated the dynamics of depolarization in ferroelectric thin films. To tune the compensation of the depolarization field we used a ferroelectric capacitor in series with linear capacitors. The stability of any set polarization state is summarized in a depolarization diagram that shows depolarizing and thermodynamically stable regimes. The boundary separating the two regimes is obtained when the internal electric field is equal to the coercive field, and yields a unique relation among the coercive field, dielectric constant and saturated polarization, $P_{sat}/\varepsilon_0\varepsilon_{ferro}E_c$. This experimentally derived constant is identical for PZT and P(VDF-TrFE) and equal to about 16. Among different ferroelectric materials the values of coercive field, dielectric constant and polarization vary by orders of magnitude. Remarkably however, the values for $P_{sat}/\varepsilon_0\varepsilon_{ferro}E_c$ are comparable. The

constant value implies that for a wide range of ferroelectric materials the depolarization field is comparable to the activation field for domain-wall creep. We propose that depinning of domain walls requires collective switching of polarized regions near the pinning sites. This mechanism naturally leads to the relation $E_{dep} \sim E_{act}$. We argue that the depolarization- and activation field are of the same order of magnitude as the intrinsic coercive field.

Chapter 7 Polarization fatigue of P(VDF-TrFE) ferroelectric capacitors*

The polarization of the ferroelectric polymer P(VDF-TrFE) decreases upon prolonged cycling. Understanding of this fatigue behavior is of great technological importance for the implementation of P(VDF-TrFE) in random-access memories. However, the origin of fatigue is still ambiguous. Here we investigate fatigue in thin-film capacitors by systematically varying the frequency and amplitude of the driving waveform. We show that the fatigue is due to delamination of the top electrode. The origin is accumulation of gases, expelled from the capacitor, under the impermeable top electrode. The gases are formed by electron-induced phase decomposition of P(VDF-TrFE), similar as reported for inorganic ferroelectric materials. When the gas barrier is removed and the waveform is adapted, a fatigue-free ferroelectric capacitor based on P(VDF-TrFE) is realized. The capacitor can be cycled for more than 10^8 times, approaching the programming cycle endurance of its inorganic ferroelectric counterparts.

* Publication: D. Zhao, I. Katsouras, M. Li, K. Asadi, J. Tsurumi, G. Glasser, J. Takeya, P. W. M. Blom, and D. M. de Leeuw, *Sci. Rep.* **4**, 5075 (2014).

7.1 Fatigue of ferroelectric capacitors

Due to the spontaneous polarization whose direction may be reversed by applying an external electrical field, the polarization can be used as a Boolean "0" and "1" in ferroelectric random access memories (FeRAM). Here, the binary information is stored in a capacitor and retrieved by applying a switching voltage to obtain a high or a low charge displacement current response, depending on whether the internal polarization was aligned or not with the direction of the applied field. The read-out is therefore destructive. If the polarization direction was changed during the read-out operation then a reset voltage needs to be applied afterwards. During these numerous read and write operations the spontaneous polarization decreases. Although this so-called polarization fatigue has been thoroughly investigated, its origin, especially for organic ferroelectrics, is still under debate.

Experimental data for the reduction of the spontaneous polarization of inorganic ferroelectric thin films under electrical stress have been reviewed by Tagantsev *et al.* in 2001 [51]. The dependence of fatigue on amplitude, frequency and profile of the driving electric field was discussed and models such as domain wall pinning and nucleation inhibition were reviewed. Experimental characteristics and explanations of polarization fatigue in inorganic thin films, bulk ceramics and single crystals have also been reviewed by Lou in 2009 [52]. Capacitors consisting of $SrBi_3TaO_9$ (SBT) exhibit virtually fatigue-free behavior. The endurance is better than 10^{12} cycles [148]. In contrast, traditional $Pb(Zr,Ti)O_3$ (PZT) capacitors with Pt electrodes are prone to fatigue. Although the degradation behavior can be improved by using conductive oxide electrodes such as RuO_2, IrO_2 and $SrRuO_3$ [51], the polarization still decreases after 10^4 to 10^9 cycles. The number of cycles at which the polarization starts to decrease is comparable for thin films, bulk ceramics and single crystals [52], which indicates that a similar degradation mechanism is responsible for the polarization fatigue. Reported models typically comprise two steps [51]: (*i*) electrical stress leads to formation or redistribution of defects and (*ii*) these imperfections influence the spontaneous polarization. For instance, electro-migration of oxygen vacancies can form extended defects capable of pinning domain walls. The oxygen vacancies can also lead to the formation of a dead interface layer at the electrodes. Furthermore, it has been reported that the fatigue of PZT capacitors could be due to local phase decomposition [53] [21]. Under electrical bipolar stress the ferroelectric PZT perovskite phase is transformed into the paraelectric pyrochlore phase, as confirmed by Micro Raman measurements. Upon annealing the fatigued capacitor in oxygen ambient, the original ferroelectric perovskite PZT phase was completely restored. Therefore, it was concluded that fatigue is a generic problem of inorganic ferroelectric materials. The origin was argued to be the formation of oxygen vacancies caused by a local, uncompensated high depolarization field.

Contrary to inorganic ferroelectrics, reports on fatigue of organic ferroelectrics are limited. The most studied organic ferroelectric materials are poly(vinylidene-difluoride) (PVDF) and its random copolymer with trifluoroethylene, P(VDF-TrFE). They are investigated due to their potential application in transducers, sensors, actuators and memories. As compared to inorganic ferroelectrics, the remanent polarization is about one order of magnitude lower and the coercive field one order of magnitude higher. However, the advantage of organic ferroelectric materials is compatibility with low temperature flexible substrates and the possibility for up-scaling by large-area solution processing. The remanent polarization and coercive field of ferroelectric capacitors did not change upon bending with a radius of curvature down to 1 cm, which illustrates that organic ferroelectrics are ideal

candidates for flexible electronics or system-in-foil applications [22] [149]. As an example, high performance non-volatile polymer memories on banknotes have recently been realized [23].

Fatigue in organic ferroelectric capacitors is a major problem as the spontaneous polarization is typically halved already after less than 10^6 cycles [52]. Fatigue depends on experimental parameters such as temperature, the type of electrodes and the frequency and amplitude of the applied waveform [54] [59] [56]. It has been reported for P(VDF-TrFE) that fatigue increases with increasing driving voltage and decreasing frequency. Bipolar driving with either sinusoidal, triangular, or rectangular waveforms introduces polarization fatigue, while unipolar switching does not. Application of polymer electrodes, such as poly(3,4-ethylenedioxythiophene) stabilized with polystyrene sulfonic acid (PEDOT:PSS), leads to improved programming cycle endurance [22]. We also note that since ferroelectric polymers are semi-crystalline, fatigue may depend on the degree of crystallinity [57].

Fatigue in organic ferroelectric materials has been ascribed to charge trapping. Injected charges get trapped at crystalline boundaries and defects, thereby locking the domain walls and reducing the polarization [55]. Increasing the crystallinity concomitantly reduces the number of defects and grain boundaries, resulting in increased reliability. The use of poorly conducting polymer electrodes, or the introduction of an interfacial blocking layer, diminishes charge injection and, hence, fatigue [58]. Apart from the intrinsic domain wall pinning mechanism, fatigue can have an extrinsic origin, such as delamination of the top electrode. A few reports [149] [56] mention this delamination and suggest a temperature rise due to the heat dissipation upon continuous cycling as the origin [149].

Here we systematically investigate fatigue of P(VDF-TrFE) thin-film capacitors. We deliberately varied the frequency and amplitude of the applied waveform. Both unipolar and bipolar switching is considered. We used Au, PEDOT:PSS or PEDOT:PSS covered with Au as top electrode. We show that fatigue is due to delamination of the top electrode. The polarization then decreases proportionally to the decreased electrode area. Thermal and piezoelectric stress is ruled out as the origin. We show that the delamination is due to formation of gases that are expelled from the capacitor. The origin is argued to be electron-induced phase decomposition of the P(VDF-TrFE), similar as reported for the inorganic ferroelectric material PZT. The mechanism is supported by inducing similar damage using high current densities in a scanning electron microscope. We show that when the gas barrier is removed and the waveform is adapted, a fatigue-free ferroelectric capacitor based on P(VDF-TrFE) is realized. The capacitor can be cycled for more than 10^8 times, approaching the programming cycle endurance of its inorganic ferroelectric counterparts [148].

7.2 Fatigue of P(VDF-TrFE) capacitors with Au electrodes

As an example we present typical fatigue measurements on a ferroelectric P(VDF-TrFE) capacitor in Fig. 7.2.1. Au is used as the top electrode. The displacement loops are presented in Fig. 7.2.1 (a) as a function of the cumulative number of cycles. The pristine capacitor exhibits a coercive field of 60 MV/m and a remanent polarization of 7 $\mu C/cm^2$, in good agreement with literature values [26]. Upon continuous cycling the coercive field remains constant but the polarization decreases severely. Fig.

7.2.1 (b) shows the corresponding remanent polarization as a function of the cumulative number of cycles. The polarization is already halved after about 10^5 cycles. Comparable numbers have been reported in literature [149] [150]. The inset shows optical micrographs of the pristine and degraded capacitor. The black framed micrograph shows that the top electrode of the pristine capacitor is smooth, while the red framed micrograph shows that in the fatigued capacitor the top electrode exhibits bumps and may have been delaminated.

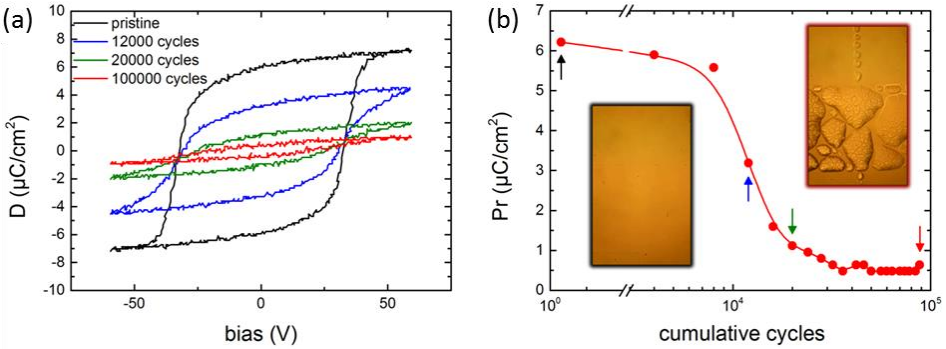

FIG. 7.2.1 (a) Evolution of the displacement loops of a P(VDF-TrFE) ferroelectric capacitor with Au top electrode under continuous cycling. The measurements were performed using a bipolar triangular waveform with a frequency of 1 kHz and the amplitude of 60V. (b) The extracted remanent polarization as a function of the cumulative number of cycles. The arrows indicate the data points corresponding to the displacement loops of Fig. 7.2.1 (a). The inset shows optical micrographs of the pristine and degraded capacitor. The black and red framed micrographs show the top electrode of the pristine and fatigued capacitor, respectively. In the fatigued capacitor the top electrode shows bumps and may have been delaminated.

To pinpoint the origin of the measured fatigue we deliberately varied the amplitude and the frequency of the bipolar triangular waveform. The normalized polarization as a function of the cumulative number of cycles is presented in Fig. 7.2.2. The frequency was fixed at 100 Hz and the amplitude was varied from 20 to 80 V. At the amplitude of 20 V the applied electric field is smaller than the coercive field. Hence the ferroelectric polarization does not switch. Not surprisingly, the intermittently measured remanent polarization is constant. Under these measurement conditions the capacitor does not switch and is fatigue-free. As soon as the applied field becomes larger than the coercive field, the ferroelectric material switches, and the polarization decreases with increasing cumulative number of cycles. Fig. 7.2.2 shows that the degradation is bias dependent. The onset of degradation is at about 10^4 cycles, but the fatigue rate strongly increases with increasing bias.

The data show that fatigue only occurs when the polarization is switched. This is in perfect agreement with reported so-called unipolar cycling [59]. The electric field then varies from zero to above the coercive field. The ferroelectric polarization does not switch and the capacitor shows no fatigue. A similar conclusion can be drawn from the frequency dependence, as will be discussed below.

Fig. 7.2.2 shows that the polarization initially increases. The polarization enhancement has been observed previously, where it was reported that it might be due to field-induced recrystallization [150]. We note that a similar enhancement can be found, upon close inspection, in other reported data sets,

both for organic [151] [152] and inorganic ferroelectrics [52]. In all our measurements there is an apparent correlation between the polarization enhancement and the onset of degradation. However, the origin is still elusive.

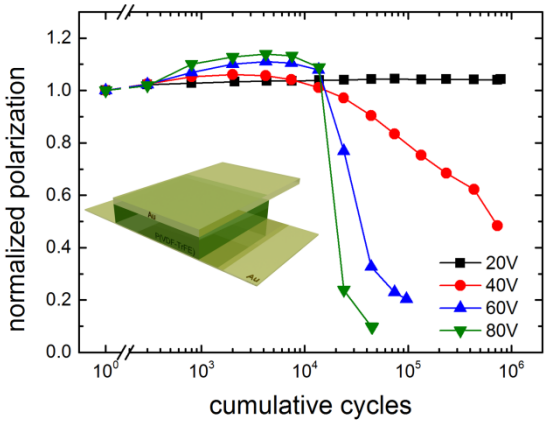

FIG. 7.2.2 The normalized polarization as a function of the cumulative number of cycles. The frequency was fixed at 100 Hz and the amplitude was varied from 20 V to 80 V. At an amplitude of 20 V the applied electric field is smaller than the coercive field. The data show that the degradation is bias dependent. The onset of the degradation is at about 10^4 cycles, but the degradation rate strongly increases with increasing bias. The inset depicts the capacitor layout, where a P(VDF-TrFE) thin film is sandwiched between two Au electrodes.

The bias dependence suggests that fatigue is related to the switching of the polarization. To substantiate this observation we investigated fatigue as a function of frequency. The frequency was varied from 10 Hz to 100 kHz. The amplitude of 40 V corresponds to an electric field larger than the coercive field. The normalized polarization as a function of the cumulative number of cycles is presented in Fig. 7.2.3 (a). At high frequency, here 100 kHz, the capacitor is fatigue-free. The polarization does not change with the number of cycles. The reason is that at this frequency the ferroelectric does not switch. This is in agreement with the bias dependence, which shows that polarization switching is a prerequisite for fatigue. From the frequency dependence we can further infer that a high electric field alone does not induce fatigue. Fig. 7.2.3 (a) shows that fatigue is observed for those frequencies at which the polarization switches. The initial polarization increase is comparable to that of Fig. 7.2.2. The onset of degradation is at about 10^4 cycles. The degradation is almost frequency independent, which suggests that fatigue is dominated by the number of switching events.

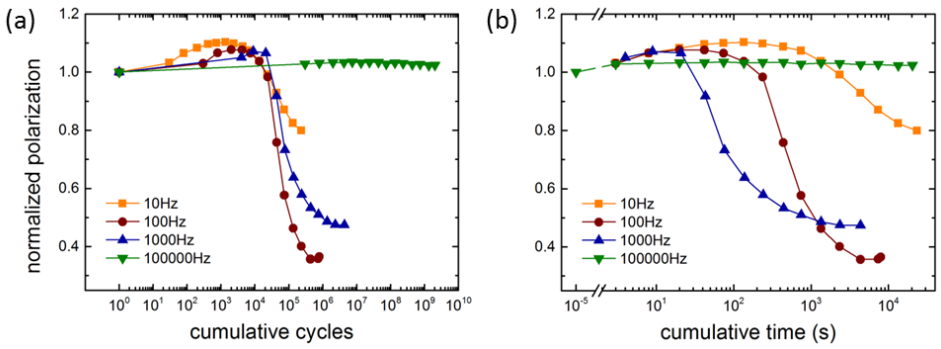

FIG. 7.2.3 Frequency dependence of fatigue. (a) The normalized polarization as a function of the cumulative number of cycles**.** The amplitude was fixed at 40V and the frequency was varied from 10 Hz to 100 kHz. At high frequency polarization switching is impeded and therefore the capacitor is fatigue-free. The onset of the degradation is at about 10^4 cycles. (b) Replotted data of normalized polarization as a function of the cumulative time**.**

The optical micrograph in Fig. 7.2.1 (b) shows that delamination of the top Au electrode may occur during the fatigue measurements. When the delamination is due to thermal stress it should depend on the dissipated energy, which is equal to the dissipated power times the cumulative time. Therefore, we replotted the data of Fig. 7.2.3 (a) not as a function of the cumulative number of cycles but as a function of cumulative time. As N is the number of cycles and f is the frequency, N/f is the cumulative time. Contrary to previous reports [59] [153] that show universal scaling, the data of Fig. 7.2.3 (b) do not collapse on a single curve. A clear trend appears. The higher the frequency, the faster the degradation is. We note that the time scales involved are in the order of 10^2-10^3 seconds.

In summary, the occurrence of fatigue in a ferroelectric P(VDF-TrFE) capacitor requires polarization switching driven by a bipolar waveform. The fatigue depends on the frequency and amplitude of the applied waveform. These dependencies suggest a power-related problem, which might lead to the observed electrode delamination. However, in the following section we show that thermal stress can be disregarded.

7.3 Mechanism

In this section, we reveal the origin of polarization fatigue of P(VDF-TrFE) thin-film capacitors. The observed frequency dependence and the amplitude dependence of fatigue suggest that the fatigue may relate to power-related processes. Besides, we argue that degradation is due to delamination of the Au top electrode of the fatigued capacitor, as indicated in Fig. 7.2.1 (b), where the polarization is diminished proportionally to the reduced electrode area. This suggests that the degradation of the P(VDF-TrFE) capacitors may be an extrinsic device problem rather than the chemical degradation of the ferroelectric material.

Thermal analysis

To estimate the temperature rise we approximate the capacitor as a zero-thickness spherical source with constant flux over its area, placed on top of a homogenous semi-infinite substrate. In this case, the thermal resistance is given by:

$$R_{th} = 8/(3\pi^2 \kappa a) \tag{7.3.1}$$

where a is the radius of the sphere and κ is the thermal conductivity of the substrate [154]. The temperature rise, ΔT, is then equal to the input power, P_{in}, multiplied by the thermal resistance:

$$\Delta T = P_{in} R_{th} \tag{7.3.2}$$

The input power is generated by switching the ferroelectric polarization. The leakage current can be disregarded. We verified that the dissipated energy per cycle is equal to the area in the displacement hysteresis loop. To that end, we recorded the displacement current and we integrated the instantaneous power $I(t)V(t)$ over the period of one cycle. The obtained values are equal to the area of the displacement loop for all frequencies at which the ferroelectric switches. We approximate this area by $2P_r \cdot 2V_c$. The dissipated energy per cycle is then given by:

$$E_{in,cycle} = 2P_r \cdot 2E_c \cdot t \cdot \pi a^2 \tag{7.3.3}$$

where P_r is the remanent polarization, E_c is the coercive field, t the thickness of the ferroelectric layer and $\pi\alpha^2$ is the surface area of the capacitor. The total dissipated power is the frequency, f, times the energy per cycle. The temperature rise follows from:

$$\Delta T = (32/3\pi\kappa) \cdot f P_r E_c t a \tag{7.3.4}$$

We calculated the temperature rise using a remanent polarization of 7 μC/cm^2, a coercive field of 60 MV/m, a frequency of 1 kHz and a layer thickness of 500 nm. The dissipated power per unit area is then ~8 kW/m^2. We take a typical surface area of 1 mm^2 and for the thermal conductivity we use either 1 W/m·K, a typical value for glass and thermally grown SiO_2, or 100 W/m·K, a typical value for the highly doped crystalline silicon wafer used as the substrate. The calculated temperature rise is 4 ^{o}C and 0.04 ^{o}C respectively, orders of magnitude too low to account for thermal delamination.

To verify these estimations we measured the temperature rise of a segmented polymeric light emitting diode on glass. For an input power of 1 kW/m^2 we estimated a temperature rise of 1.7 ^{o}C for a segment with a radius of 2 mm. Here we have assumed that all input power is converted into heat. The estimated value did nicely agree with the experimental value, as measured for the segmented display, of about 2 ^{o}C.

The time scale for thermal delamination is off by orders of magnitude as well. The time constant, τ, is the product of the thermal capacitance of all material that has to be heated and the thermal resistance.

$$\Delta T(t) = \Delta T_{\max}\left[1 - \exp(-t/\tau)\right] \tag{7.3.5}$$

where $\tau = q_{th} V R_{th}$. We take a volumetric heat capacity, q_{th}, of 2 Ws/cm^{3}K. The longest time scale is obtained when we assume that the whole substrate, with a volume V, has to be heated. The time constant is then at most seconds, still orders of magnitude smaller than the experimental time at which fatigue sets in. We note that the time scale, Eq. (7.3.5), does not depend on the dissipated power but only on the substrate properties. Experimentally, however, fatigue rate increases with frequency, hence with increasing dissipated power. Delamination therefore cannot be due to thermal stress. Finally, we used a simplified thermal model. By adapting the thermal resistance, albeit that the values then are unrealistic, a large temperature rise or a long time scale can be calculated. However, these values cannot be obtained simultaneously. A large temperature rise and a long time scale are mutually exclusive. Hence, in summary, fatigue and delamination of the top electrode cannot be due to thermal stress.

Mechanical frustration induced by inverse piezoelectricity

The modelling of the previous section proved that degradation cannot be due to thermal stress induced by the dissipated power. However, P(VDF-TrFE) is not only ferroelectric but also piezoelectric. The delamination of the top electrode might then be due to the piezoelectric response of the P(VDF-TrFE) layer. Application of an electrical field leads to a contraction in the direction of the field and to a simultaneous expansion in the lateral direction. The resulting lateral strain leads to a mechanical stress at the interface between the top electrode and the P(VDF-TrFE) thin film. The top Au electrode is not compliant, which means that the generated stress cannot be accommodated. Therefore, the top electrode delaminates. The strain, *i.e.* the relative change in the lateral dimension, l, is in first order approximation directly proportional to the applied electric field, $\Delta l/l = d_{31} \cdot E$. Fig. 7.2.2, however, shows that there is no fatigue when the amplitude corresponds to a field below the coercive field. The P(VDF-TrFE) film still exhibits a piezoelectric response though. Therefore, piezoelectricity can be ruled out as the origin of fatigue.

Electrically induced phase decomposition

With thermal delamination and mechanical frustration ruled out, the remaining possible origin of the delamination is gas expelled from the capacitor upon cycling. The gases are formed by phase decomposition of P(VDF-TrFE), induced by the high internal electric fields generated upon switching the polarization.

Gas formation is not unexpected. The radiation chemistry of the homopolymer, PVDF, is well-established and covered in two thorough reviews [155] [156]. During electron beam irradiation or γ-radiolysis, PVDF undergoes elimination of HF. The following mechanism has emerged. Electrons are injected and trapped at defects, grain boundaries or domain walls. At a given applied external electric field the capacitor is in static equilibrium. All molecular dipoles are compensated for, either internally or by counter-charges at the electrodes. The internal electric field is negligible and the trapped charges remain fixed. However, when the polarization switches temporarily large depolarization fields occur. Hot electrons are injected and trapped electrons are accelerated by this internal electric field. The charge carriers have enough energy to abstract F^- ions, which in turn initiate unzipping reactions of the PVDF chains. As a result HF is formed together with unsaturated carbon bonds and cross-linked moieties. The polyene bonds have been identified by optical and infrared absorption measurements, while Raman measurements have confirmed that H^+ and F^- ions are formed in unzipping chain reactions [157]. These reactions only occur when the polarization switches. The gas emission has been monitored using permeable grid electrodes [158]. Gases were predominantly produced at the negatively charged electrode and only during polarization switching. The threshold for gas emission corresponded to the coercive field. Under constant electric field the gas emission decreased by at least an order of magnitude.

To confirm the gas-induced delamination, we looked at the temporal evolution of the electrode morphology. Fig. 7.3.1 shows *in-situ* optical micrographs taken during a fatigue measurement. The Au electrode of the pristine capacitor is smooth. During cycling small bumps are formed. With time the number of bumps increases, they grow in size and finally coalesce into macroscopic bubbles. The gold electrode acts as a gas barrier. The gas expelled from P(VDF-TrFE) is accumulated at the interface forming bumps that grow in time. Finally, the top electrode is delaminated, which is visible by the naked eye.

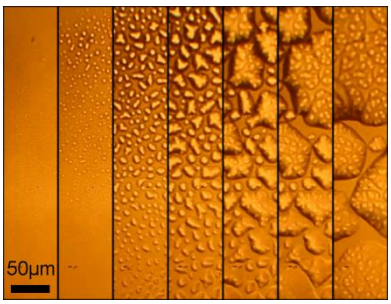

FIG. 7.3.1 Temporal evolution of the electrode morphology. In-situ optical micrographs on the same spot, taken during a fatigue measurement of a P(VDF-TrFE) capacitor with Au electrodes. The fatigue measurement was performed using a bipolar triangular waveform with a frequency of 1 kHz and an amplitude of 60 V. The left micrograph shows that the Au electrode of the pristine capacitor is smooth. The right micrograph shows that the top electrode is delaminated, which is visible by the naked eye.

We note that the gas volume required for delamination can be produced by a negligible amount of decomposed polymer. Hence, it is not surprising that the phase decomposition cannot be detected

electrically, such as in leakage current or in direct reduction of polarization. Furthermore, we note that for organic ferroelectrics the effect is very pronounced because the electrode is not covalently bound to the polymer layer. The adhesion between the polymer layer and the electrode is limited to van der Waals forces.

Prerequisites for fatigue are therefore both the presence of injected and/or trapped charges and switching of the polarization. This explains why fatigue can be less pronounced when using poorly injecting electrodes and why fatigue only occurs under bipolar switching. Furthermore it might explain the dependence on the waveform. Triangular or sinusoidal pulses yield similar programming cycle endurance, while the use of rectangular pulses, with abrupt variations in electric field, inevitably leads to an enhanced fatigue behavior. We expect that this mechanism also explains the initial enhancement of the remanent polarization upon cycling. However, we could not pinpoint the direct link. Electrons injected in the pristine polymer might yield extra compensation charges that can stabilize the polarization of parts in the film that had not yet been polarized.

Local phase decomposition has been reported as a generic fatigue mechanism for inorganic ferroelectrics. Optical micrographs of fatigued PZT capacitors showed dark spots due to holes in the Pt top electrode. The delaminated holes are due to evaporation of oxygen and/or Pb/PbO from the interface [53]. Micro Raman measurements, performed in the micron size holes, showed that the ferroelectric perovskite phase was transformed into the paraelectric pyrochlore phase. Upon annealing the degraded capacitor in an O_2 ambient, the perovskite phase and the accompanying ferroelectric polarization was restored. The phase decomposition was initiated by large depolarization fields that occur when the polarization is switched. It has been argued that the same mechanism holds for other inorganic ferroelectrics such as $BaTiO_3$. Here we have shown that it explains fatigue in the organic ferroelectric P(VDF-TrFE).

The phase decomposition mechanism is confirmed by electron beam-induced damage in a scanning electron microscope. A high probe current was used to expose a pristine capacitor. Real-time images were recorded during the exposure. The composite SEM micrograph in Fig. 7.3.2 shows the time evolution (left to right) of a growing bump on the top Au electrode (light gray area).

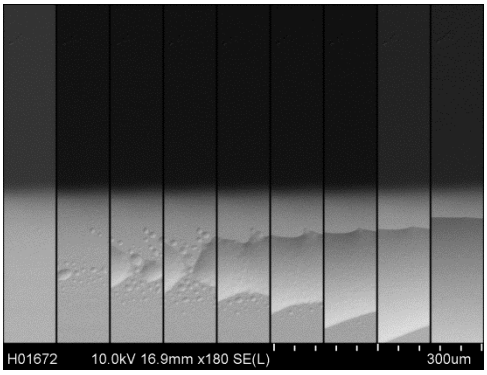

FIG. 7.3.2 Electron-beam induced damage. A pristine capacitor (left) is exposed to a 10 keV electron beam under analytical SEM conditions with a high probe current of ~1 nA. Real-time images were recorded during the exposure. The composite SEM micrograph shows the time evolution (left to right) of a growing bump on the top Au electrode (light gray area).

7.4 Fatigue-free P(VDF-TrFE)-based capacitors

We have shown that the delamination of the top electrode is caused by accumulation of volatile components expelled from the capacitor and blocked by the top electrode. The gases are generated when the polarization switches. The delamination can be avoided by adapting the waveform of the cycling and/or by adapting the layout of the capacitor. The waveform controls the gas generation and diffusion rate. In the adapted layout of the capacitor configuration the gas barrier is removed.

In Fig. 7.4.1 we varied the duty cycle of the waveform. We cycled the capacitor with a triangular waveform of 100 Hz. The red curve shows the normalized polarization as a function of the cumulative number of cycles for continuous cycling. The polarization rapidly decreases and is halved after approximately 5×10^4 cycles. The resulting morphology of the top electrode is schematically depicted in the inset. Next, we adapted the duty cycle. The continuous cycling was interrupted every second with a waiting time of up to 10 seconds, as schematically depicted in the inset of Fig. 7.4.1. The cycling endurance increases with waiting time, as shown by the blue (5 s waiting time) and green (10 s waiting time) curves. The measured dependence on duty cycle can be explained as follows. While switching gas is generated by phase decomposition of P(VDF-TrFE). During the waiting time the gas can diffuse out of the capacitor. Gas accumulation at the interface between the P(VDF-TrFE) layer and the top electrode is thereby prevented. The reduced delamination results in improved programming cycle endurance.

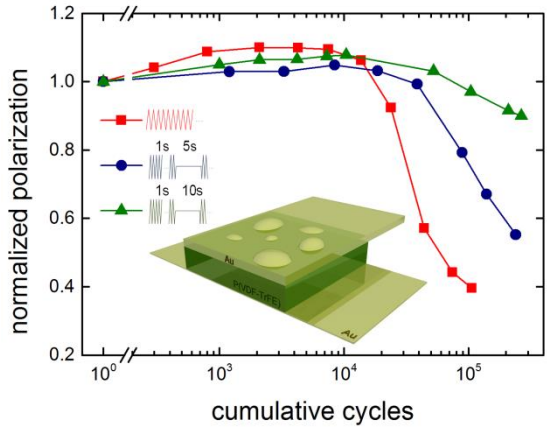

FIG. 7.4.1 Improved programming cycle endurance. Fatigue measurement of a P(VDF-TrFE) capacitor with Au electrodes. The measurement was performed using a variable duty cycle. The red curve shows the normalized polarization as a function of the cumulative number of cycles for continuous cycling with a bipolar triangular waveform with a frequency of 100 Hz and an amplitude of 40V. The inset depicts the resulting morphology of the top electrode. The blue and green curves correspond to measurements where the continuous cycling was interrupted every second with a waiting time of 5 and 10 seconds, respectively. The programming cycle endurance increases with decreasing duty cycle.

To further enhance the endurance and to substantiate the relevance of gas-induced delamination, we varied the capacitor layout. We changed the gold electrode, which is impermeable to gases, to the polymeric conductor PEDOT:PSS, whose gas diffusion coefficient is orders of magnitude higher.

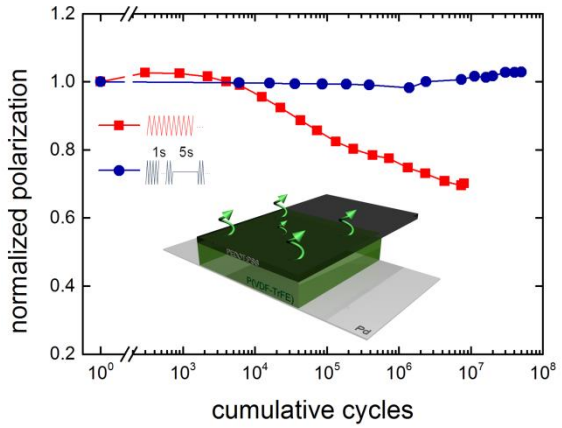

FIG. 7.4.2 Fatigue-free P(VDF-TrFE) ferroelectric capacitors. Fatigue measurement of a P(VDF-TrFE) capacitor with a PEDOT:PSS top electrode. The red curve shows the normalized polarization as a function of the cumulative number of cycles for continuous cycling with a bipolar triangular waveform with a frequency of 100 Hz and an amplitude of 40 V. The blue curve corresponds to measurements using a waiting time of 5 seconds and a frequency of 1 kHz. The inset depicts the facilitated gas diffusion through the top polymeric electrode. A fatigue-free capacitor is realized with a programming cycle endurance of 10^8 cycles.

Fig. 7.4.2 shows the normalized polarization as a function of the cumulative number of cycles for a PVDF-TrFE capacitor with a PEDOT:PSS top electrode. The red curve shows fatigue under continuous operation. Although improved with respect to a Au top electrode, the capacitor still shows fatigue. Optical inspection did show that the morphology of the top electrode changes. With time, micro-voids on the surface of the PEDOT:PSS electrode become clearly visible. By introducing a waiting time of 5 seconds, represented by the blue data points, a fatigue-free capacitor is realized. The inset depicts the facilitated gas diffusion through the polymeric top electrode. In this case, the morphology of the electrode does not change. However, when we apply an additional Au capping layer, the PEDOT:PSS/Au stack becomes impermeable to volatile components and the fatigue behavior resembles that of capacitors with Au-only electrodes, *c.f.* Fig. 7.2.1. Without Au, using only a PEDOT:PSS electrode and by reducing the duty cycle, there is no degradation up to 10^8 cycles. The programming cycle endurance of the P(VDF-TrFE) capacitor approaches that of its inorganic ferroelectric counterparts.

7.5 Summary

We have systematically investigated fatigue of P(VDF-TrFE) thin-film capacitors. In a capacitor with Au electrodes the coercive field remains constant but the polarization severely decreases under continuous cycling. A thermal analysis showed that thermal stress can be disregarded. To pinpoint the origin of the measured fatigue we deliberately varied the amplitude and the frequency of the applied bipolar waveform. The dependence on amplitude shows that fatigue is related to the switching of the

polarization. The onset of degradation is at about 10^4 cycles, but the degradation rate strongly increases with increasing amplitude. The frequency dependence shows that at low frequency the polarization unambiguously decreases with the number of cycles. At high frequency the capacitor is fatigue-free because the polarization does not switch.

We argue that the origin of fatigue in P(VDF-TrFE) capacitors is delamination of the Au top electrode, as can be seen from in-situ optical micrographs. The delamination is due to gases formed by phase decomposition of the P(VDF-TrFE), induced by the high internal electric fields that occur when the polarization switches. The mechanism is confirmed by inducing similar damage using high current densities in a scanning electron microscope. We show that when the gas barrier is removed and the waveform is adapted to control the gas generation and diffusion rates, a fatigue-free capacitor is realized. The P(VDF-TrFE)-based ferroelectric capacitor can be cycled more than 10^8 times.

Chapter 8 Perspective: in-plane polarization and vortices in ferroelectrics

Hitherto, all our focuses are on the out-of-plane polarization, *i.e.* the polarization perpendicular to the ferroelectric thin film as well as the direction of the applied electric field. The aforementioned macroscopic polarization specifically refers to the out-of-plane polarization, consisting of domains with *up* or *down* polarity, whereas the in-plane polarization is disregarded. In thin-film ferroelectric devices, it is the out-of-plane polarization that enables their application in information storage, as the out-of-plane polarization can be aligned and switched among multiple states by applied static electric field and maintains the value when the electric field is removed. The in-plane-polarization however, has no net macroscopic effect when that within the whole thin film is added up, therefore is for a long time of no practical interests.

With the development of the techniques in visualizing and engineering the domains in smaller and smaller scale, local properties of domain walls become increasingly interesting in recent decades [159]. Contemporarily, it has been shown that in low-dimensional ferroelectric materials, there exists exotic topological phase transition, which greatly broadens the scope and capability of future in-plane-polarization related applications. In this Chapter, we briefly review reported recent progress in the research of the in-plane polarization in ferroelectric materials.

8.1 Charged domain walls

The charged domain walls (CDWs) refer to a type of ferroelectric domain walls where the net bound charges exist. In general, adjacent domains are naturally forced towards equilibrium with electrostatic neutrality in between, *e.g.* the 180° out-of-plane domain walls. Charged domain walls can arise in two circumstances. In the first case, when the equilibrium neutral domain-wall configuration is slightly perturbed, for example during polarization switching, the domain walls become weakly charged due to the in-plane polarization divergence [160]. These weakly charged domain walls are usually instable and tend to relax to low-energy, uncharged orientations after removal of the external field unless pinned by local defects [161]. Another situation of the charged domain walls, termed as the strongly charged domain walls, refers to a type of domain walls formed with a "head-to-head" or "tail-to-tail" in-plane polarization configuration [162]. With the participation of the clamping effect of two ferroelastic states, the strongly charged domain walls with such "head-to-head" or "tail-to-tail" polarization configuration can be stabilized without defect pinning [160].

The bound charges at charged domain walls can gather free charges to eliminate the depolarization field [160] [161]. The gathered free charges at the charged domain walls form degenerated quasi-two-dimensional electron gas with metallic free-carrier concentration, resulting in a local insulator-metal transition [163] [164] [165] [166] [160]. Such a transition is directly reflected by the local conductivity. *J-V* measurements on weakly charged domain walls show transient, enhanced conductivity 10-10^3 times that of the bulk [166]. The intrinsic conductivity on strongly charged domain wall with "head-to-head" configuration in $BaTiO_3$ was found 10^8-10^{10} higher than bulk with the thickness of the domain wall as 10-100 nm taken into consideration [160]. Furthermore, the conductivity as a function of the temperature was obtained in Ref. [160], showing the metallic behaviour as $\sim[1+a\cdot(T-T_0)]^{-1}$. These finding are not of fundamental interest, but also suggest potential applications such as ultra-high-density information storage based on charged-domain-wall induced resistive switching [161].

The bound charges at the charged domain walls can also affect the properties of the surrounding material with an in-plane depolarization field incompletely compensated. This depolarization field leads to the rotation of the polarization as schematically shown in Ref. [167], and enhanced dielectric and piezoelectric response of each domain [167]. A ferroelectric material with dense patterns of charged domain walls are therefore expected to have strongly enhanced piezoelectric properties, promising for high-performance devices for energy harvesting, transducers, and *etc*.

8.2 In-plane vortices and skyrmionic configurations

The swirling field textures, *e.g.* vortices, anti-vortices, are now widely recognized as objects of both fundamental interest and technological relevance. The formation of such in-plane flux-closure structures is regarded as a result of chiral interactions. Ferroelectrics, lacking such chiral interactions, have long been left aside in this quest.

The interactions governing the ferroelectric material is the long-range Coulomb interaction and short-range covalent interaction [5]. In nanostructured ferroelectrics, the long-range Coulomb interaction is truncated due to lack of periodicity, and the short-range interaction is significantly modified near the surface boundary [168]. Based on first-principles-derived effective Hamiltonian approach coupled with Monte Carlo simulations, Fu *et al*. found robust vortex patterns of the in-plane polarization in barium titanate quantum dots and wires [168]. Later, they conducted *ab initio* studies on free-standing nanoparticles of $Pb(Zr_{0.5}Ti_{0.5})O_3$ solid solution [169], and pointed out that the formation of such vortex pattern belongs to a topological phase transition, where a new order parameter as the toroid moment is defined as:

$$\mathbf{G} = (2N)^{-1} \sum_i \mathbf{R}_i \times \mathbf{p}_i \tag{8.2.1}$$

where N is the number of cells in the simulation, $\mathbf{p}_i$ is the local dipole of cell i located at $\mathbf{R}_i$. The out-of-plane component of toroid moment, G_z, increases sharply below 600 K while being zero at higher temperature. They also found that the specific heat exhibits a hump around 550 K, which further confirmed the existence of a phase transition. Below the transition temperature, the vortex configuration was found energetically more stable than the periodic 180° domains with an out-of-plane polarization; in other words, the system prefers spontaneous vortex to spontaneous polarization.

The vortex structure was found bistable, as the toroid moment, **G**, can be equivalently parallel or anti-parallel to the plane norm. The two states can be accessed via and alternating magnetic field which interacts with the toroid moment by generating a curling electric field:

$$\nabla \times \mathbf{E} = -\frac{\partial \mathbf{B}}{\partial t} \tag{8.2.2}$$

And the coercive field was defined as $\partial\mathbf{B}/\partial t$ needed to switch the toroid moment, unlike a static electric field switching the out-of-plane polarization in ferroelectrics thin films or bulks.

The data storage via switchable macroscopic toroid moment could be superior to using spontaneous polarization for the following reasons [169]. Firstly, generating a magnetic field does not require electrode contact which is challenging for make in nanoscale devices. Secondly, the vortex phase does not exhibit macroscopic polarization or produce a strong electric field that has long-range character. Therefore the vortex structure in a single nanoparticle can be switched without modifying the states of its neighbouring particles, and hence the toroid carriers of information can be packed considerably more densely than the conventional carriers of polarization, giving rise to remarkable improvement in the density of ferroelectric recording. The minimum diameter that they found to be able to generate bistable toroid states is 3.2 nm, enabling a storage density of 60 Tbit/inch^2. The stability of the vortices was found depending on the strain. First-principle based simulations on perovskite nanoparticles [170] have suggested: (i) unstrained flat nanoparticles transform into a vortex state with an in-plane curling polarization, (ii) under strong enough compressive strain the vortex state is no longer stable and gives way to a 180° domain phase.

The existence and stability of in-plane flux-closure configurations in geometrically confined nano-ferroelectrics have also been tested using phase-field simulations [171] [172] where Helmholtz free energy consists of the Landau-Ginzburg term, the electrostatic energy, the elastic energy, the surface energy *etc*. In the nano-ferroelectric materials, the trend to minimize the residual stress and the stray field leads to the formation of closed circuits of 90° domains.

The predicted existence of in-plane vortices in geometrically confined ferroelectrics further intrigued the search for electrical skyrminons in ferroelectric materials. Skyrmions are topologically protected objects which are stable against perturbations. The topological charge is defined as:

$$Q = \frac{1}{4\pi}\int \mathbf{u}\cdot\left(\partial_x \mathbf{u}\times\partial_y \mathbf{u}\right)\mathrm{d}x\mathrm{d}y \tag{8.2.3}$$

where **u** denotes the normalized local dipole moment. The topological charge takes integral numbers whose change relates to topological phase transitions. The skyrmionic configuration in ferromagnets [173] [174] and anti-ferromagnets [175] has been intensively studied and remains an active field. To find the counterpart in ferroelectrics is of fundamental interest. The formation of skyrmions in magnets has been ascribed to the chiral Dzyaloshinskii-Moriya interaction [176] [177] which is absent in ferroelectrics. However, the geometrical confinement in nanoscale ferroelectric materials may enable formation of skyrmions as hinted from the existence of vortices in such materials [178].

Nahas *et al*. simulated the cylindrical $BaTiO_3$ nanowire with a radius of 2.7 nm embedded in a $SrTiO_3$ matrix to study electrical skyrmions [178]. They first performed a temperature annealing under an external electric field of 100 MV/m along the plane norm. On reaching 15 K, the field was set to zero and further relax the dipole configuration. The resulting relaxed configuration features a co-existence of a spontaneous polarization along the plane norm and a flux-closure vortex structure; the topological charge calculated was 0, meaning that the structure was topologically trivial. However, when the state was subject to an electric field against the plane norm, with value of about 16.5 MV/m, the topological charge sharply changes to 1, indicating the formation of topologically non-trivial skyrmion. The formed skyrmions were stable, and can be as small as a few nanometers. Their findings widened the scope and capabilities of future skyrmion-based applications.

Experimental evidences [179] [41] [180] for in-plane vortices in ferroelectrics are currently very rare. Via piezoresponse force microscopy, images of in-plane vortices formed by bundles of in-plane nano domains have been reported [41]. The dimension of such vortices, however, is of hundreds of nanometers. The vortices were found to occur spontaneously and can also be produced by external electric field. Contrary to theoretical predictions, the vortices were found in large-area ferroelectric thin films, not just in nanodots, and were found not limited by geometric grain boundaries [41]. Physical origins of such contradictions with simulation results [168] [169] [170] [178] remain elusive; observation of in-plane vortex in atomic scale, as has been achieved for 180° flux-closure domains near interfaces [181] and ferroelectric/paraelectric superlattices [182], is yet to be explored.

Summary

In summary, we have systematically investigated the device physics of polarization in ferroelectric thin films, including polarization switching, evolution of ferroelectric domains, retention of various polarization states, mechanism of domain-wall depinning, and the mechanism of polarization fatigue. This thesis consists of experimental investigations and theoretical modeling.

Chapter 1 is a short introduction to the fundamentals of ferroelectricity and PVDF-based ferroelectric polymers. The microscopic origin of ferroelectricity has been discussed from both an *ab initio* and a phenomenological point of view. The ferroelectricity in polymers has been reviewed from monomeric to macroscopic device level. The theory and computer simulation of polarization switching has been elaborated in **Chapter 2**. The hysteresis loops of the polarization- and strain *vs.* the electric field have been simulated and shown good agreement with experimental data. **Chapter 3** described the experimental details on device fabrication and measurements. In **Chapter 4**, the transients of the polarization switching have been systematically investigated as a function of electric field and temperature. A random walk model has been presented that correlates the observed switching dynamics with the morphology of ferroelectric domains. We have elaborated the piezoresponse force microscopy investigation in **Chapter 5**. We have shown for the first time an explicit correlation between the mean out-of-plane piezoresponse phase and the macroscopic polarization. The underlying origin for the retention of domains absent of screening free charges at conductive electrodes has been discussed. The domain morphology discussed in **Chapter 4** has been directly visualized. The measurement of the dynamics of depolarization has surprisingly allowed us unraveling the universal mechanism of domain-wall depinning and the long-standing puzzle of the origin of Merz law. The story has been discussed in depth in **Chapter 6**. In **Chapter 7**, we have investigated the fatigue in P(VDF-TrFE) thin-film capacitors. We have demonstrated that the fatigue is due to delamination of the top electrode caused by the accumulation of gases formed by electron-induced phase decomposition of P(VDF-TrFE). We have shown an ultra-endurable ferroelectric capacitor based on P(VDF-TrFE) when the gas can be released, approaching the programming cycle endurance of its inorganic ferroelectric counterparts. **Chapter 8** is a briefly review on recent research progresses on in-plane polarization as a future outlook of this thesis, in which two topics, *i.e.* the in-plane vortices and the charged domain walls, have been specifically chosen.

Acknowledgement

It is difficult to express my innumerous thanks with words to all those who have made my pursuit for PhD a lifelong unforgettable memory. Nevertheless, I would like to deliver my acknowledgement, which is far beyond words, to them in this part.

I would like to give special thanks to Prof. Dr. Dago de Leeuw at the Max-Planck Institute for Polymer Research (MPIP) for his supervision as well as his strong impetus on my development in academia. I feel so lucky to have the chance to learn from and discuss with such a world-famous scientist so frequently, several times per day, to be precise. His help to my improvement is multiple, including scientific knowledge, experimental techniques, the way of writing and presenting, the matters of dealing with people and *etc*. Dago has deeply influenced my attitude towards research. He is an extremely dedicated scientist, spending all day time in the lab or discussing or writing with students, which I not only appreciate but also take as exemplar. Dago has convinced me of the importance of a full dataset instead of merely "useful" data. "You've had an expectation before the measurement; then you treat the rest data which do not support your expectation as useless. It's not the correct way!" he once told me. I shall keep this in mind forever. I also treasure the off-duty time with him: the lunches together, the days of traveling after conferences in Italy, in Singapore, in China and in Germany, the time we drinking beer after paper finalized...

I thank Prof. Dr. Paul Blom (MPIP) for his helpful support both administratively and scientifically. It is my great honor to once be a member of this group which I have had known from uncountable brilliant publications and had being longing for during writing my Bachelor thesis five years ago. Discussing with Paul is always inspiring and pleasant without any pressure, which I enjoy a lot.

I thank Prof. Dr. Hans-Joachim Elmers (Johannes-Gutenberg University Mainz) and Prof. Dr. Mathias Kläui (JGU) for helpful discussions and advices.

I am grateful to my colleagues as well as co-authors, Dr. Ilias Katsouras, Dr. Mengyuan Li, Dr. Kamal Asadi and Mr. Thomas Lenz, for excellent collaboration. While Ilias introduced me into ferroelectrics and paved the way for high-quality research in our lab, Thomas explored shoulder by shoulder with me, and we have made remarkable progresses together.

I am grateful to Mrs. Petra Pausch (MPIP) for her generous help in administrative affairs, and by the way, thanks for the information of the amazing concerts. I do owe many thanks to Mr. Hans-Peter Raich, Mr. Frank Keller, Mr. Gunnar Glass and Mr. Uwe Rietzler (MPIP) for their technical support. It is their professional effort that guarantees our productive research.

I thank Prof. Dr. Edmund Boschitz (Karlsruhe Institute of Technology, Germany) for his warm help ranging from career-wise advices to life philosophy. We met in his seminar in the Department of Physics at Peking University in 2009. Since then we maintain a friendship which I treasure a lot. And I do appreciate his words to me: focus on your Holy Grail; things like money and reputations are secondary and come automatically.

I thank Dr. Hans-Peter Loebl (Philips Research Laboratory, Aachen, Germany) and Prof. Dr. Uli Lemmer (KIT) for supervising my Master thesis and Prof. Dr. Lixin Xiao and Prof. Dr. Zhijian Chen (Peking University, China) for supervising my Bachelor thesis. Their patient guidance made my way to PhD application possible.

I thank Mr. Junto Tsurumi and Mr. Yu Yamashita (The University of Tokyo, Japan), Mr. Cheng Guo, Mr. Haonan Huang and Mr. Lian Duan (Peking University, China) for research assistance.

I appreciate fruitful discussions with my friends in the field of ferroelectrics all over the world, especially Dr. Zhen Huang (Swiss Federal Institute of Technology in Lausanne, Switzerland) and Dr. Linze Li (The University of Michigan, USA).

I also thank my friends in other field of scientific research, whom are Dr. Yuki Nagata, Dr. Fen-Yen Lin and Mr. Zhijun Chen (MPIP), Dr. Binghong Han and Miss Lili Yu (Massachusetts Institute of Technology, USA), Mr. Yanhao Tang (Michigan State University, USA), Mr. She Chen (Tsinghua University, China), Dr. Ziyao Wang (Philips Research Laboratory, Aachen, Germany), Mr. Qing Shi (McGill University, Canada), Mr. Bin Xu (Princeton University, USA), Mr. Yongxi Ou (Cornell University, USA), Dr. Xinyi Li (Swiss Federal Institute of Technology in Zurich, Switzerland), Mr. Wenping Cui (Rheinische Friedrich-Wilhelms University Bonn, Germany), Mr. Ta-Shun Chou (Friedrich-Alexander University Erlangen-Nürnberg, Germany), and Mr. Zhengqi Wang (KIT), for their inspiring comments from other aspects of view.

At the occasion of finishing this thesis, I would like to mention my parents. They have created an atmosphere full of love in which I grew up. Their love is my greatest fortune. They have provided me with best family education and have encouraged me developing my hobbies, choosing my career and leading my life independently. It is always my greatest pride to have such a family. Last but not least, I would like to express my infinite love to my parents to whom I am in debt in all respects. 谁言寸草心，报得三春晖!

List of publications*

1. D. Zhao, T. Lenz, I. Katsouras, P. W. M. Blom, and D. M. de Leeuw, Global excitation and local probing of ferroelectric domains, *Org. Electron.* **47,** 189 (2017).

2. J. M. Perez, D. Zhao, T. Lenz, I. Katsouras, D. M. de Leeuw, and N. Stingelin, Solid-state-processing of δ-PVDF, *Mater. Horiz.* **4,** 408 (2017).

3. M. Ghittorelli, T. Lenz, H. Dehsari, D. Zhao, K. Asadi, P. W. M. Blom, Z. Kovacs-Vajna, and D. M. de Leeuw, Quantum tunnelling and charge confinement in organic ferroelectric memory diodes, *Nature Commun.* **8.** 15741 (2017).

4. D. Zhao, I. Katsouras, K. Asadi, W. A. Groen, P. W. M. Blom, and D. M. de Leeuw, Retention of intermediate polarization states in ferroelectric materials enabling memories for multi-bit data storage, *Appl. Phys. Lett.* **108,** 232907 (2016).

5. I. Katsouras, K. Asadi, M. Li, T. B. Van Driel, K. S. Kjær, D. Zhao, T. Lenz, Y. Gu, P. W. M. Blom, D. Damjanovic, M. M. Nielsen, and D. M. De Leeuw, The negative piezoelectric effect of the ferroelectric polymer poly (vinylidene fluoride), *Nature Mater.* **15,** 78 (2016).

6. D. Zhao, I. Katsouras, K. Asadi, P. W. M. Blom, and D. M. de Leeuw, Switching dynamics in ferroelectric P(VDF-TrFE) thin films, *Phys. Rev. B* **92,** 214115 (2015).

7. I. Katsouras, D. Zhao, M. Spijkman, M. Li, P. W. M. Blom, D. M. de Leeuw, and K. Asadi, Controlling the on/off current ratio of ferroelectric field-effect transistors, *Sci. Rep.* **5,** 12094 (2015).

8. T. Lenz, D. Zhao, G. Richardson, I. Katsouras, K. Asadi, G. Glasser, S. Zimmermann, N. Stingelin, C. Roelofs, M. Kemerink, P. W. M. Blom, and D. M. de Leeuw, Microstructured organic ferroelectric thin film capacitors by solution micromolding, *Phys. Status Solidi A* **212,** 10 (2015).

9. D. Zhao, I. Katsouras, M. Li, K. Asadi, J. Tsurumi, G. Glasser, J. Takeya, P. W. M. Blom, and D. M. de Leeuw, Polarization fatigue of organic ferroelectric capacitors, *Sci. Rep.* **4,** 5075 (2014).

* Publications related to PhD topic.

References

[1] K. Rabe, Ch. H. Ahn, J. -M. Triscone, Physics of Ferroelectrics: A Modern Perspective, Heidelberg: Springer, 2007.

[2] J. Valasek, *Phys. Rev.* 15, 537 (1920).

[3] J. Valasek, *Phys. Rev.* 17, 4 (1921).

[4] I. Katsouras, K. Asadi, L. M., T. van Driel, K. S. Kjær, D. Zhao, T. Lenz, Y. Gu, P. W. M. Blom, D. Damjanovic, Nielsen, M. and D. M. de Leeuw, *Nature Mater.* 15, 78–84 (2016).

[5] R. E. Cohen, *Nature* 358, 136-138 (1992).

[6] R. Resta, *Ferroelectrics* 136, 51 (1992).

[7] R. D. King-Smith and D. Vanderbilt, *Phys. Rev. B* 47, 1651 (1993).

[8] R. Resta, *Rev. Mod. Phys.* 66, 899 (1994).

[9] C. Kittel, Introduction to Solid State Physics 7th Ed., New York: Wiley, 1996.

[10] G. Shirane and R. Pepinsky, *Phys. Rev.* 91, 812 (1953).

[11] W. Zhong and D. Vanderbilt, *Phys. Rev. Lett.* 73, 13 (1994).

[12] B. Zalar, V. V. Laguta and R. Blinc, *Phys. Rev. Lett.* 90, 3 (2003).

[13] K. Tashiro and M. Kobayashi, *Phase Trans.* 18, 213-246 (1989).

[14] B. B. Tian, X. F. Bai, Y. Liu, P. Gemeiner, X. L. Zhao, B. L. Liu and Y. H. Zou, *Appl. Phys. Lett.* 106, 092902 (2015).

[15] R. Clausius, Die Mechanische Behandlung der Electrica, Berlin: Vieweg, 1879.

[16] L. D. Landau and E. M. Lifshitz, Statistical Physics, Oxford: Pergamon, 1959.

[17] A. F. Devonshire, *Philos. Mag.* 40, 1040 (1949).

[18] H. Kawai, *Jpn. J. Appl. Phys.* 8, 975 (1969).

[19] J. G. Bergman, Jr., J. H. McFee, G. R. Crane, *Appl. Phys. Lett.* 18, 203 (1971).

[20] A. J. Lovinger, *Science* 220, 4602 (1983).

[21] X. Lou, M. Zhang, S. A. T. Redfern and J. F. Scott, *Phys. Rev. B* 75, 224104 (2007).

[22] M. A. Khan, U. S. Bhansali, X. X. Zhang, M. M. Saleh, I. Odeh and H. N. Alshareef, *Appl. Phys. Lett.* 101, 143303 (2012).

[23] M. A. Khan, U. S. Bhansali and H. N. Alshareef, *Adv. Mater.* 24, 2165-2170 (2012).

[24] G. Botelho, S. Lanceros-Mendez, A. Gonçalves, V. Sencadas and J. Rocha, *J. Non-Cryst. Solids* 354, 72 (2008).

[25] D. C., W. N. Mei, W.-G. Yin, J. Liu, J. R. Hardy, S. Ducharme and P. A. Dowben, *Phys. Rev. B* 69, 235106 (2004).

[26] T. Furukawa, *Phase Trans.* 18, 143 (1989).

[27] J. F. Scott, Ferroelectric Memories, Heidelberg: Springer, 2000.

[28] V. L. Ginzburg, *Fiz. Tverd. Tela* 2, 2031 (1960).

[29] A. Tagantseve, L. Cross and J. Fousek, Domains in Ferroic Crystals and Thin Films, New York: Springer, 2010.

[30] A. Kolmogorov, *Izv. Akad. Nauk USSR; Ser. Math.* 3, 355 (1937).

[31] M. Avrami, *J. Chem. Phys.* 7, 1103 (1939).

[32] Y. Ishibashi and Y. Takagi, *J. Phys. Soc. Jpn.* 31, 506 (1971).

[33] Y. Genenko, S. Zhukov, S. Yampolskii, J. Schutrumpf, R. Dittmer, W. Jo, H. Kung, M. Hoffmann and H. von Seggern, *Adv. Funct. Mater.* 22, 2058 (2012).

[34] P. Sharma, T. J. Reece, S. Ducharme and A. Gruverman, *Nano Lett.* 11, 1970 (2011).

[35] J. Y. Jo, H. S. Han, J. G. Yoon, T. K. Song, S. H. Kim and T. W. Noh, *Phys. Rev. Lett.* 99, 267602 (2007).

[36] A. K. Tagantsev, I. Stolichnov, N. Setter, J. S. Cross and M. Tsukada, *Phys. Rev. B* 66, 214109 (2002).

[37] R. Miller and G. Weinreich, *Phys. Rev.* 117, 6 (1960).

[38] T. Tybell, P. Paruch, T. Giamarchi and J. Triscone, *Phys. Rev. Lett.* 89, 9 (2002).

[39] P. Guethner and K. Dransfeld, *Appl. Phys. Lett.* 61, 1137 (1992).

[40] G. Catalan, H. Béa, S. Fusil, M. Bibes, P. Paruch, A. Barthélémy and J. F. Scott, *Phys. Rev. Lett.* 100, 027602 (2008).

[41] Y. Ivry, D. P. Chu, J. F. Scott and C. Durkan, *Phys. Rev. Lett.* 104, 207602 (2010).

[42] A. Gruverman, D. Wu and J. F. Scott, *Phys. Rev. Lett.* 100, 097601 (2008).

[43] Y. Takahashi, N. Tomoda and T. Furukawa, *Polym. J.* 47, 249 (2015).

[44] A. V. Ievlev, S. Jesse, A. N. Morozovska, E. Strelcov, E. A. Eliseev, Y. V. Pershin, A. Kumar, V. Shur and S. V. Kalinin, *Nature Phys.* 10, 59-66 (2014).

[45] L. J. McGilly, P. Yudin, L. Feigl, A. K. Tagantsev and N. Setter, *Nature Nanotechnology* 10, 145-150 (2015).

[46] A. Kholkin, S. V. Kalinin, A. Roelofs and A. Gruverman, "Chapter I.6," in *Scanning Probe Microscopy*, New Yor, USA, Springer, 2007.

[47] S. V. Kalinin, B. J. Rodriguez, S. Kim, S. Hong, A. Gruverman and E. A. Eliseev, *Appl. Phys. Lett.* 92, 152906 (2008).

[48] S. V. Kalinin, A. N. Morozovska, L. Q. Chen and B. J. Rodriguez, *Rep. Prog. Phys.* 73, 056502 (2010).

[49] R. Gysel, A. K. Tagantsev, I. Stolichnov, N. Setter and M. Pavius, *Appl. Phys. Lett.* 89, 082906 (2006).

[50] R. G. P. McQuaid, L. J. McGilly, P. Sharma, A. Gruverman and J. M. Gregg, *Nature Commun.* 2, 404 (2011).

[51] A. K. Tagantsev, I. Stolichnov, E. L. Colla and N. Setter, *J. Appl. Phys.* 90, 1387-1402 (2001).

[52] X. Lou, *J. Appl. Phys.* 105, 024101 (2009).

[53] X. Lou, M. Zhang, S. A. T. Redfern and J. F. Scott, *Phys. Rev. Lett.* 97, 177601 (2006).

[54] G. Zhu, X. Luo, J. Zhang, Y. Gu and Y. Jiang, *IEEE T. Dielect. El. In* 17, 1172-1177 (2010).

[55] G. Zhu, Y. Gu, H. Yu, S. Fu and Y. Jiang, *J. Appl. Phys.* 110, 024109 (2011).

[56] X. Zhang, H. Xu and Y. Zhang, *J. Phys. D: Appl. Phys.* 44, 155501 (2011).

[57] H. Xu, J. Zhong, X. Liu, J. Chen and D. Shen, *Appl. Phys. Lett.* 90, 092903 (2007).

[58] H. Xu, X. Liu, X. Fang, H. Xie, G. Li, X. Meng, J. Sun and J. Chu, *J. Appl. Phys.* 105, 034107 (2009).

[59] G. Zhu, Z. Zeng, L. Zhang and X. Yan, *Appl. Phys. Lett.* 89, 102905 (2006).

[60] S. Ducharme, V. M. Fridkin, A. V. Bune, S. P. Palto, L. M. Blinov, N. N. Petukhova and S. G. Yudin, *Phys. Rev. Lett.* 84, 175 (2000).

[61] G. Vizdrik, S. Ducharme, V. M. Fridkin and S. G. Yudin, *Phys. Rev. B* 68, 094113 (2003).

[62] R. Ahluwalia, M. Sullivan, D. Srolovitz, J. Zheng and A. Huan, *Phys. Rev. B* 78, 054110 (2008).

[63] H. Hu and L. Q. Chen, *J. Am. Ceram. Soc.* 81, 3 (1998).

[64] S. Jesse, B. J. Rodriguez, S. Choudhury, A. P. Baddorf, I. Vrejoiu, D. Hesse, M. Alexe, E. A. Eliseev, A. N. Morozovska, J. Zhang, L. Chen and S. V. & Kalinin, *Nature Mater.* 7, 209-215 (2008).

[65] B. L. Li, X. P. Liu, F. Fang, J. L. Zhu and L. J. M., *Phys. Rev. B* 73, 014107 (2006).

[66] F. Xue, X. S. Gao and J. M. Liu, *J. Appl. Phys.* 106, 114103 (2009).

[67] Y. Ma, K. Albe and B. Xu, *Phys. Rev. B* 91, 184108 (2015).

[68] L. F. Wang and J. M. Liu, *Appl. Phys. Lett.* 89, 092909 (2006).

[69] H. L. Hu and L. Q. Chen, *Mater. Sci. Eng. A* 238, 182 (1997).

[70] T. Furukawa and N. Seo, *Jpn. J. Appl. Phys.* 29, 675 (1990).

[71] S. M. Nakhmanson, M. B. Nardelli and J. Bernholc, *Phys. Rev. Lett.* 92, 115504 (2004).

[72] J. F. Scott, *Adv. Mater.* 22, 5315 (2010).

[73] N. Setter, D. Damjanovic, L. Eng, G. Fox, S. Gevorgian, S. Hong, A. Kingon, H. Kohlstedt, N. Y. Park, G. B. Stephenson, I. Stolitchnov, A. K. Taganstev, D. V. Taylor, T. Yamada, and S. Streiffer, *J. Appl. Phys.* 100, 051606 (2006).

[74] W. J. Hu, D.-M. Juo, L. You, J. Wang, Y.-C. Chen, Y.-H. Chu and T. Wu, *Sci. Rep.* 4, 4772 (2014).

[75] T. J. Yang, Venkatraman Gopalan, P. J. Swart and U. Mohideen, *Phys. Rev. Lett.* 82, 4106 (1999).

[76] M. Chu, I. Szafraniak, R. Scholz, C. Harnagea, D. Hesse, M. Alexe and U. Gösele, *Nature Mater.* 3, 87-90 (2004).

[77] R. C. Buchanan, T. R. Armstrong and R. D. Roseman, *Ferroelectrics* 135, 1 (1992).

[78] Y. Wu, X. Li, A. M. Jonas and Z. Hu, *Phys. Rev. Lett.* 115, 267601 (2015).

[79] Y. Shin, I. Grinberg, I. Chen and A. Rappe, *Nature* 449, 881-884 (2007).

[80] M. Kühn and H. Kliem, *Phys. Stat. Sol. (b)* 1, 213-223 (2008).

[81] C. T. Black, C. Farrell and T. J. Licata, *Appl. Phys. Lett.* 71, 2041-2043 (1997).

[82] M. Stengel, N. A. Spaldin and D. Vanderbilt, *Nature Phys.* 5, 304-308 (2009).

[83] D. Zhao, I. Katsouras, K. Asadi, W. A. Groen, P. W. Blom and D. M. de Leeuw, *Appl. Phys. Lett.* 108, 232907 (2016).

[84] E. Soergel, *J. Phys. D: Appl. Phys.* 44, 464003 (2011).

[85] A. Kuroda, S. Kurimura and Y. Uesu, *Appl. Phys. Lett.* 69, 1565 (1996).

[86] M. Merz, *Phys. Rev.* 95, 690 (1954).

[87] S. Zhukov, Y. A. Genenko, O. Hirsch, J. Glaum, T. Granzow and H. von Seggern, *Phys. Rev. B* 82, 014109 (2010).

[88] A. Nautiyal, K. Sekhar, N. Pathak, N. Dabra, J. Hundal and R. Nath, *Appl. Phys. A* 99, 941 (2010).

[89] T. Furukawa and G. Johnson, *Appl. Phys. Lett.* 38, 1027 (1981).

[90] I. Stolichnov, P. Maksymovych, E. Mikheev, S. V. Kalinin, A. K. Tagantsev and N. Setter, *Phys. Rev. Lett.* 108, 027603 (2012).

[91] P. Sharma, T. Nakajima, S. Okamur and A. Gruverman, *Nanotechonlogy* 24, 015706 (2013).

[92] T. Witten and L. Sander, *Phys. Rev. Lett.* 47, 19 (1981).

[93] P. Meakin, Fractals, Scaling and Growth Far from Equilibrium, New York: Cambridge University Press, 1998.

[94] R. Naber, B. de Boer, P. W. M. Blom and D. M. de Leeuw, *Appl. Phys. Lett.* 87, 203509 (2005).

[95] Z. Xiao, S. Poddar, S. Ducharme and X. Hong, *Appl. Phys. Lett.* 103, 112903 (2013).

[96] J. Jo, S. Yang, T. Kim, H. Lee, J. Yoon, S. Park, Y. Jo, M. Jung and T. Noh, *Phys. Rev. Lett.* 102, 045701 (2009).

[97] R. Landauer, D. Young and M. Drougard, *J. Appl. Phys.* 27, 752 (1956).

[98] C. Pulvari and W. Kuebler, *J. Appl. Phys. Lett.* 29, 1315-1321 (1958).

[99] Y. So, D. Kim, T. Noh, J. Yoon and T. Song, *Appl. Phys. Lett.* 86, 092905 (2005).

[100] S. Yang, J. Jo, T. Kim, J. Yoon, T. Song, H. Lee, Z. Marton, S. Park, Y. Jo and T. Noh, *Phys. Rev. B* 82, 174125 (2010).

[101] C. Nelson, P. Gao, J. Jokisaari, C. Heikes, C. Adamo, A. Melville, S. Baek, C. Folkman, B. Winchester, Y. Gu, Y. Liu, K. Zhang, E. Wang, J. Li, L. Chen, C. Eom, D. Schlom and X. Pan, *Science* 334, 968-971 (2011).

[102] D. Zhao, I. Katsouras, M. Li, K. Asadi, J. Tsurumi, G. Glasser, J. Takeya, P. W. M. Blom and D. M. de Leeuw, *Sci. Rep.* 4, 5075 (2014).

[103] R. Gysel, I. Stolichnov, A. Tagantsev, N. Setter and P. Mokrý, *Appl. Phys. Lett.* 103, 084120 (2008).

[104] B. Rodriguez, S. Jesse, A. Baddorf and S. Kalinin, *Phys. Rev. Lett.* 98, 247603 (2007).

[105] L. Cipelletti and L. Ramos, *Curr. Opin. Colloid Interface Sci.* 7, 228-234 (2002).

[106] A. Gruverman and A. Kholkin, *Rep. Prog. Phys.* 69, 2443 (2005).

[107] T. Lenz, D. Zhao, G. Richardson, I. Katsouras, K. Asadi, G. Glasser, S. Zimmermann, N. Stingelin, C. Roelofs, M. Kemerink, P. Blom and D. de Leeuw, *Phys. Status Solidi A* 212, 10 (2015).

[108] Y. Ehara, S. Yasui, T. Oikawa, T. Shiraishi, N. Oshima, T. Yamada, Y. Imai, O. Sakata and H. Funakubo, *Appl. Phys. Lett.* 108, 21 (2016).

[109] D. Fu, K. Suzuki, K. Kato and H. Suzuki, *Appl. Phys. Lett.* 82, 13 (2003).

[110] T. Furukawa, T. Nakajima and Y. Takahashi, *IEEE T. Dielect. EL. In.* 13, 5 (2006).

[111] S. M. Nakhmanson, M. B. Nardelli and J. Bernholc, *Phys. Rev. Lett.* 92, 11 (2004).

[112] S. Tong, W. Jung, Y. -Y. Choi, S. Hong and A. Roelofs, *ACS Nano* 10, 2568-2574 (2016).

[113] M. J. Highland, T. T. Fister, D. D. Fong, P. H. Fuoss, C. Thompson, J. A. Eastman, S. K. Streiffer and G. B. Stephenson, *Phys. Rev. Lett.* 107, 187602 (2011).

[114] M. F. Chisholm, W. Luo, M. P. Oxley, S. T. Pantelides and H. Lee, *Phys. Rev. Lett.* 105, 197602 (2010).

[115] G. Geneste and B. Dkhil, *Phys. Rev. B* 79, 235420 (2009).

[116] D. Li, M. H. Zhao, J. Garra, A. M. Kolpak, A. M. Rappe, D. A. Bonnell and J. M. Vohs, *Nature Mater.* 7, 473-477 (2008).

[117] P. Sharma, T. Reece, D. Wu, V. M. Fridkin, S. Ducharme and A. Gruverman, *J. Phys.: Condens. Matter.* 21, 485902 (2009).

[118] D. Zhao, I. Katsouras, K. Asadi, P. W. M. Blom and D. M. de Leeuw, *Phys. Rev. B* 92, 214115 (2015).

[119] C. Kittel, *Phys. Rev.* 70, 965 (1946).

[120] T. Mitsui and J. Furuichi, *Phys. Rev.* 90, 193 (1953).

[121] R. R. Mehta, B. D. Silverman and J. T. Jacobs, *J. Appl. Phys.* 44, 3379-3385 (1973).

[122] P. Wurfel, I. P. Batra and J. T. Jacobs, *Phys. Rev. Lett.* 30, 1218-1221 (1972).

[123] M. Stengel and N. A. Spaldin, *Nature* 443, 679-682 (2006).

[124] M. Stengel, D. Vanderbilt and N. A. Spaldin, *Nature Mater.* 8, 392-397 (2009).

[125] D. J. Kim, J. Y. Jo, Y. S. Kim, Y. J. Chang, J. S. Lee, Jong-Gul Yoon, T. K. Song and T. W. Noh, *Phys. Rev. Lett.* 95, 237602 (2005).

[126] G. Gerra, A. K. Tagantsev, N. Setter and K. Parlinski, *Phys. Rev. Lett.* 107603, 96 (2006).

[127] T. P. Ma and J. -P. Han, *IEEE Electron. Device Lett.* 23, 386-388 (2002).

[128] J. Holterman and P. Groen, An Introduction to Piezoelectric Materials and Components, Stichting Applied Piezo, 2012.

[129] M. Mai, B. Martin and H. Kliem, *J. Appl. Phys.* 110, 064101 (2011).

[130] A. K. Tagantsev and G. Gerra, *J. Appl. Phys.* 100, 051607 (2006).

[131] U. Robels, J. H. Calderwood and G. Arlt, *J. Appl. Phys.* 77, 4002-4008 (1995).

[132] E. Fatuzzo and W. J. Merz, *Phys. Rev. B* 116, 61-68 (1959).

[133] A. Khan and e. al., *Nature Mater.* 14, 182-186 (2015).

[134] J. Jo and e. al., *Nano Lett.* 15, 4553-4556 (2015).

[135] P. Zubko and e. al., *Nature* doi: 10.1038 (2016).

[136] L. M. and e. al., *Nature Mater.* 12, 433-438 (2013).

[137] Y. Tan and e. al., *Sci. Rep.* 5, 9953 (2015).

[138] I. Fujii, M. Ugorek and Trolier-McKinstry, *J. App. Phys.* 107, 104116 (2010).

[139] K. Amanuma, T. Hase and Y. Miyasaka, *Appl. Phys. Lett.* 66, 221-223 (1995).

[140] J. W. Lee, Y. Takase, B. A. Newman and J. I. Scheinbeim, *J. Polym. Sci. Pol. Phys.* 29, 279-286 (1991).

[141] A. V. Gorbunov and e. al., *Phys. Chem. Chem. Phys.* 18, 23663-23672 (2016).

[142] K. Yoshii, Y. Hiruma, H. Nagata and T. Takenaka, *Jpn. J. Appl. Phys.* 45, 4493-4496 (2006).

[143] K. Sakata and Y. Masuda, *Ferroelectrics* 7, 347-349 (1974).

[144] H. H. Wieder, *J. Appl. Phys.* 28, 367-369 (1957).

[145] S. Lemerle, J. Ferré, C. Chappert, V. Mathet, T. Giamarchi and P. Le Doussal, *Phys. Rev. Lett.* 80, 849 (1998).

[146] G. Blatter, M. V. Feigel'man, V. B. Geshkenbein, A. I. Larkin and V. M. Vinokur, *Rev. Mod. Phys.* 66, 1125-1388 (1994).

[147] M. J. Highland, T. T. Fister, M. Richard, D. D. Fong, P. H. Fuoss, C. Thompson, J. A. Eastman, S. K. Streiffer and G. B. Stephenson, *Phys. Rev. Lett.* 105, 167601 (2010).

[148] C. de Araujo, J. Cuchiaro, D. McMillan, M. C. Scott and J. F. Scott, *Nature* 374, 627-629 (1994).

[149] M. A. Khan, U. S. Bhansali, M. N. Almadhoun, I. N. Odeh, D. Cha and H. N. Alshareef, *Adv. Funct. Mater.* 24, 10 (2014).

[150] S. Yuan, X. Meng, J. Sun, Y. Cui, J. Wang, L. Tian and J. Chu, *Phys. Lett. A* 375, 1612-1614 (2011).

[151] F. Fang, W. Yang, C. Jia and X. Luo, *Appl. Phys. Lett.* 92, 222906 (2008).

[152] Y. Mabuchi, T. Nakajima, T. Furukawa and S. Okamura, *Appl. Phys. Express* 4, 071501 (2011).

[153] M. Dawber and J. F. Scott, *Appl. Phys. Lett.* 76, 1060-1062 (2000).

[154] H. Carlslaw and J. Jaeger, Conduction of heat in solids, 2nd ed, Oxford: Oxford University Press, 1959.

[155] J. S. Forsy and D. J. T. Hill, *Prog. Polym. Sci.* 25, 101-136 (2000).

[156] B. J. Lyons, *Radiat. Phys. Chem.* 45, 159-174 (1995).

[157] W. Eisenmenger and H. Schmidt, in *Proc. 10th, Symp. Int. IEEE Symp. Electrets (ISE10)*, Athens, 1999.

[158] E. Bihler, K. Holdik and W. Eisenberger, *IEEE Trans. Electr. Insul.* 22, 207–210 (1987).

[159] G. Catalan, J. Seidel, R. Ramesh and J. F. Scott, *Rev. Mod. Phys.* 84, 119 (2012).

[160] T. Sluka, A. K. Tagantsev, P. Bednyakov and N. Setter, *Nature Commun.* 4, 1808 (2013).

[161] L. Li, J. Britson, J. R. Jokisaari, Y. Zhang, C. Adamo, A. Melville, D. G. Schlom, L. Q. Chen and X. Q. Pan, *Adv. Mater.* 28, 6574-6580 (2016).

[162] C. L. Jia, S. B. Mi, K. Urban, I. Vrejoiu, M. Alexe and D. Hesse, *Nature Mater.* 7, 57-61 (2007).

[163] Y. Watanabe, M. Okano and A. Masuda, *Phys. Rev. Lett.* 86, 332 (2001).

[164] B. M. Vul, G. M. Guro and I. Ivanchik, *Ferroelectrics* 6, 29-31 (1973).

[165] M. Y. Gureev, A. K. Tagantsev and N. Setter, *Phys. Rev. B* 83, 184104 (2011).

[166] P. Maksymovych, A. N. Morozovska, P. Yu, E. A. Eliseev, Y. H. Chu, R. Ramesh, A. P. Baddorf and S. V. Kalinin, *Nano Lett.* 12, 209 (2012).

[167] T. Sluka, A. K. Tagantsev, D. Damjanovic, M. Gureev and N. Setter, *Nature Commun.* 3, 748 (2012).

[168] H. Fu and L. Bellaiche, *Phys. Rev. Lett.* 91, 25 (2003).

[169] I. I. Naumov, L. Bellaiche and H. Fu, *Nature* 432, 737-740 (2004).

[170] I. Naumov and A. M. Bratkovskzy, *Phys. Rev. Lett.* 101, 107601 (2008).

[171] J. Slutsker, A. Artemev and A. Roytburd, *Phys. Rev. Lett.* 100, 087602 (2008).

[172] W. J. Chen, Y. Zheng, B. Wang, D. C. Mab and F. R. Ling, *Phys. Chem. Chem. Phys.* 15, 7277-7285 (2013).

[173] W. Jiang, P. Upadhyaya, W. Zhang, G. Yu, M. B. Jungfleisch, F. Y. Fradin, J. E. Pearson, Y.

Tserkovnyak, K. L. Wang, O. Heinonen, S. G. E. te Velthuis and A. Hoffmann, *Science* 349, 6245 (2015).

[174] S. Woo, K. Litzius, B. Krüger, M. -Y. Im, L. Caretta, K. Richter, M. Mann, A. Krone, R. M. Reeve, M. Weigand, P. Agrawal, I. Lemesh, M. A. Mawass, P. Fischer, M. Kläui and G. S. D. Beach, *Nature Mater.* 15, 501-506 (2016).

[175] J. Barker and O. A. Tretiakov, *Phys. Rev. Lett.* 116, 147203 (2016).

[176] I. Dzyaloshinsky, *J. Phys. Chem. Solids* 4, 241-255 (1958).

[177] T. Moriya, *Phys. Rev.* 120, 91-98 (1960).

[178] Y. Nahas, S. Prokhorenko, L. Louis, Z. Gui, I. Kornev and L. Bellaiche, *Nature Commun.* 6, 8542 (2015).

[179] A. Gruverman, D. Wu, H. -F. Fan, I. Vrejoiu, M. Alexe, R. J. Harrison and J. F. Scott, *J. Phys.: Condens. Matter* 20, 342201 (2008).

[180] R. G. P. McQuaid, A. Gruverman, J. F. Scott and J. M. Gregg, *Nano Lett.* 14, 4230-4237 (2014).

[181] C. -L. Jia, K. W. Urban, M. Alexe, D. Hesse and I. Vrejoiu, *Science* 331, 1420-1423 (2011).

[182] A. K. Yadav, C. T. Nelson, S. L. Hsu, Z. Hong, J. D. Clarkson, C. M. Schlepütz, A. R. Damodaran, P. Shafer, E. Arenholz, L. R. Dedon, D. Chen, A. Vishwanath, A. M. Minor, L. Q. Chen, J. F. Scott, L. W. Martin and R. Ramesh, *Nature* 530, 198 (2016).